Far- and Near-Field Photochemistry of Single Molecules on a Metal Surface

Dissertation
zur Erlangung des Grades eines
Doktors der Naturwissenschaften (Dr. rer. nat.)

am Fachbereich Physik
der Freien Universität Berlin

vorgelegt von

Hannes Böckmann

Berlin 2018

This work was started in September 2014 and finished in August 2018 in the group of Dr. Takashi Kumagai at the Department of Physical Chemistry of the Fritz-Haber-Institut der Max-Planck-Gesellschaft.

Berlin, August 2018

Erstgutachter: Prof. Dr. Martin Wolf
Zweitgutachterin: Prof. Dr. Katharina Franke

Disputation: 05.06.2019

Abstract

Photoexcitation of molecules on metal surfaces can drive chemical reactions within the excited state along otherwise not accessible reaction pathways. Fast relaxation to substrate induced dissipation channels, however, significantly reduces the reaction yield. The concentration of visible light in the near-field of metal nanostructures has been demonstrated before to enhance the excitation rate of adsorbed molecules and compensate increased losses. Quantitative insight into the underlying mechanism at the single-molecule level within a well-defined nanostructure geometry is nevertheless missing and usually inaccessible in ensemble averaging techniques. Low-temperature scanning tunneling microscopy (STM) is ideally suited to study single molecules, while the junction, formed between a noble metal tip and and substrate, provides an individual, precisely tunable nano-gap, in which the electric field of the incident light is dramatically enhanced.
In this thesis, a combination of STM with wavelength tunable laser excitation is used to investigate single-molecule photochemistry within a tip-sample junction. The molecular photochemical reactivity is monitored as function of photon energy which provides insight into the underlying excitation mechanism while comparing optical far- and near-field excitation.
Porphycene molecules on copper surfaces act as multiresponsive, bi-stable tautomeric switches. Within this work, the optical stimulus is explored through far-field excitation. We find that photogenerated substrate charge carriers drive the tautomerization via non-adiabatic coupling of vibrational energy to the reaction coordinate.
By narrowing the tip-sample gap into the range of optical near-field enhancement, the photochemical reactivity is enhanced by 10^2-10^3. In the tunneling regime, photogenerated charge carriers mediate inelastic tunneling between tip and sample and can attach to molecule electronic states before thermalization.
As optically induced porphycene tautomerization is found highly responsive to the near-field magnitude at the apex, it is further employed as a sensitive sensor to study the plasmonic response of scanning tunneling tips. Microstructured tips are found to exhibit a spectrally modulated near-field at the apex due to the formation of surface plasmon cavity resonances which provides a facile tool for customizing the near-field response.
The here presented findings contribute to the understanding of plasmon enhanced chemistry at the level of a single metallic nano-gap and molecule which is unattainable in ensemble averaging techniques and demonstrates a possibility to fabricate tailored near-field optical probes.

Kurzfassung

Photoanregung von Molekülen auf Metalloberflächen kann chemische Reaktionen im angeregten Zustand entlang andernfalls nicht erreichbarer Reaktionspfade auslösen. Trotzdem wird die Reaktionsausbeute signifikant reduziert durch schnelle Relaxation zu substratinduzierten Streukanälen. Es ist bereits gezeigt worden, dass die Konzentration sichtbaren Lichts im Nahfeld metallischer Nanostrukturen die Anregungsrate adsorbierter Moleküle verstärkt und die erhöhten Verluste kompensiert. Nichtsdestotrotz fehlt ein quantitativer Einblick in den zugrundeliegenden Mechanismus auf der Einzelmolekülebene innerhalb einer wohldefinierten Nanostruktur, welcher normalerweise unerreichbar mit Ensemble-mittelnden Techniken ist. Niedertemperatur-Rastertunnelmikroskopie (RTM) ist ideal geeignet um einzelne Moleküle zu studieren. Der übergang zwischen Edelmetallspitze und Substrat stellt eine einzelne, einstellbare Nano-Lücke dar, in welcher das elektrische Feld einfallenden Lichts dramatisch verstärkt wird.
In dieser Dissertation wird eine Kombination aus RTM und wellenlängendurchstimmbarer Laseranregung eingesetzt um Einzelmolekül-Photochemie in einem Spitze-Probe-übergang zu untersuchen. Die photochemische Reaktivität eines Moleküls wird als Funktion der Photonenenergie aufgezeichnet, was einen Einblick in den zugrundeliegenden Anregungsmechanismus gewährt im Vergleich zwischen optischer Fern- und Nahfeldanregung.
Porphyzenmoleküle auf Kupferoberflächen stellen vielfältig ansprechbare, bi-stabile tautomerische Schalter dar. Innerhalb dieser Arbeit wird der optische Reiz durch Fernfeld-Anregung erforscht. Wir finden heraus, dass photogenerierte Ladungsträger aus dem Substrat die Tautomerisierung auslösen durch nicht-adiabatische Kopplung von Vibrationsenergie zur Reaktionskoordinate.
Durch die Verengung des Spitze-Probe-übergangs in den Bereich optischer Nahfeld-Verstärkung wird die photochemische Reaktivität um 10^2-10^3 verstärkt. Im Tunnelregime können photogenerierte Ladungsträger vor der Thermalisierung durch inelastisches Tunneln zwischen Spitze und Probe an elektronische Zustände des Moleküls anheften.
Da optische induzierte Tautomerisierung von Porphyzen hoch sensitiv auf die Stärke des Nahfelds am Apex reagiert, wird sie als sensibler Sensor zur Erforschung der plasmonischen Antwort von Rastertunnelspitzen genutzt. Es wurde herausgefunden, dass mikrostrukturierte Spitzen ein spektral moduliertes Nahfeld am Apex aufweisen durch die Bildung von Hohlraumresonanzen für Oberflächenplasmon, was ein einfaches Werkzeug zur individuellen Anpassung der Nahfeld-Antwort darstellt.
Die hier präsentierten Erkenntnisse tragen zum Verständnis plasmonisch verstärkter Chemie auf dem Level einzelner metallischer Nano-Lücken und Moleküle bei, welches unzugänglich für Ensemble-mittelnde Techniken ist und demonstriert die Möglichkeit, angepasste optische Nahfeld-Sonden herzustellen.

Abbreviations

STM Scanning Tunneling Microscopy
STS Scanning Tunneling Spectroscopy
STML Scanning Tunneling Microscopy Luminescence
SPM Scanning Probe Microscopy
SEM Scanning Electron Microscopy
DNA Deoxyribonucleic Acid
LUMO Lowest Unoccupied Molecular Orbital
HOMO Highest Occupied Molecular Orbital
ARPES Angle Resolved Photoemission Spectroscopy
DFT Density Functional Theory
CW continuous wave
IR infrared
UV ultraviolet
FIB Focused Ion Beam
TTB Tetra-*tert*-butyl
SERS Surface Enhanced Raman Spectroscopy
TERS Tip-Enhanced Raman Spectroscopy
SNOM Scanning Near-Field Optical Microscopy
PSTM Photon Scanning Tunneling Microscopy
AFM Atomic Force Microscopy
UHV ultra-high vacuum
4NBT 4-Nitrobenzenethiol
DMAB p,p'-dimercaptoazobisbenzene
ATP Aminothiophenol
ABT [4-(phenylazo)phenoxy]hexane-1-thiol
LSPR localized surface plasmon resonance
SPP surface plasmon polariton

Contents

1 Introduction

Chemical reactions that occur under light may yield desired products, which are inaccessible with thermal excitation, as the light stimulus can drive the reaction in an excited molecular state. Photochemical reactions of molecules on solid surfaces largely differ from those in the gas phase or solution as the interaction with the substrate modifies the energy potential landscape of molecular processes. New excitation pathways also become possible due to energy and charge exchange between molecule and substrate [1]. However, it also causes rapid relaxation of the excited molecular states, leading to quenching of photochemical reactions. In order to gain fundamental understanding of elementary processes in the complex surface photochemistry, it is essential to investigate model systems in a well-defined environment. Single-crystal metal surfaces under UHV conditions offer a unique playground to examine adsorbate structures and dynamics at the atomistic level and many photochemical processes have been investigated [2].
In order to expand to more realistic catalysts, metal nanoparticle decorated surfaces have been explored [3]. Metal nanoparticles have unique chemical and optical properties which are considerably different from flat metal surfaces and which are determined not only by size and composition of the individual particle but also by the geometry of an entire ensemble [4, 5]. The strong resonant optical absorption through surface plasmon excitation can be tuned by varying the above parameters which provides a viable tool to enhance the photochemical performance of adsorbed molecules [6]. Research on such plasmonic catalysts has attracted increasing attention because of potential applications to clean energy/material production with the aid of sunlight [7]. It was found that specifically hot-carrier mediated reactions are of particular interest as charge carrier excitation from plasmonic decay governs most of the investigated systems [8–13]. However, the complex geometry of nanoparticle agglomerates makes a direct identification of the spectral plasmonic response and resulting charge carrier generation at active sites very challenging so that it remains unknown when using ensemble averaging techniques. Nevertheless, the identification of optimal geometry and composition of a plasmonic nanostructure is highly desirable [10]. As the nanometer sized gaps between individual particles, where the near-field is most intense, are hypothesized to be photochemically most active, a detailed understanding of the interplay between the local plasmonic response and photochemical reactivity at the single-molecule level in an individual nano-gap is indispensable to design tailored plasmonic catalysts.
STM can probe photochemical reactions of individual molecules located within the tip-sample junction. In this thesis, a combination of STM with wavelength tunable laser excitation is employed to study the tautomerization reaction of individual porphycene molecules on single crystal copper surfaces, induced either by far- or near-field excitation. The wavelength dependent reaction yield was found to directly correlate with the near-field intensity and could therefore be used to unravel the interplay between the plasmonic properties of a nanostructure and the hot-carrier mediated reaction pathway. Structural modifications of the tip were performed to manipulate the resulting near-field properties in the junction. Furthermore, insight into the origin and energy distribution of photoexcited charge carrier in the tip-sample junction could be achieved.
Our findings demonstrate the relation between the local plasmonic response and photochemical reactivity of a single molecule in a precisely tunable nano-gap. Modification of the tip with nanometer precision can yield spectrally sharp and tunable reso-

nances, which may be employed to tailor plasmonic catalysts to specific demands. Furthermore, we demonstrate a novel approach to control the local spectral response in a scanning probe setup for the reliable application of light coupling into a tip-sample junction.

This work is structured as follows.
Chapter 2 summarizes the physical concepts and precedenting works in the field of photochemistry. The historical development of the discipline is followed by the explanation of the mechanism of direct optical absorption by a molecule which governs photochemical reactions in the gas phase and solution. Subsequently, the explanation is expanded to the condensed phase. Furthermore, recent studies on plasmon-induced reactions over metallic nanoparticles are presented. The focus of this section lies on photoexcited charge carrier generation and its dissipation.
Chapter 3 describes instrumental and experimental methods, in particular STM combined with a quasi continuous wave (CW) laser system for wavelength variable excitation of the sample surface. The physical concept of quantum tunneling in a metallic tip-sample junction and the particular scanning probe system, used throughout this work is briefly introduced with focus on coupling the laser beam to the STM junction to conduct quantitative measurements of the photochemical reaction. As the structural and material dependent plasmonic properties of different STM tips is one of the main topics in this work, the tip preparation procedure is also outlined in detail.
Chapter 4 reviews previous STM studies on single-molecule tautomerization of porphycene on single-crystal copper surfaces which is, in this work, used as a sensitive sensor to the near-field excitation in the STM junction. General aspects of tautomerization including an intramolecular hydrogen atom transfer are also discussed. An overview of the studies on thermally and STM induced tautomerization has stimulated the exploration of the light-induced processes which is the main topic in this work. A comprehensive picture of far-field induced photoexcitation in porphycene and the subsequent reaction mechanism lead up to near-field mediated excitation.
Chapter 5 is comprised of two parts. In the first part, the formerly in the far-field investigated porphycene tautomerization is translated into the near-field within the STM junction with primary focus on differences arising between the excitation schemes. The second part will focus solely on the near-field mediated reaction with emphasis on the control of plasmonic properties within the STM junction which governs the spectral response of the reaction which is determined by microscopic structures of an employed plasmonic tip. An elaborate study of tip engineering sheds light on the plasmonic properties of commonly used scanning probe tips.
Chapter 6 describes the study of a photoinduced bi-stable flipping reaction of methanol derivatives which investigates the energy distribution of photoexcited charge carriers in the STM junction by introducing differently strong adsorbed molecules to understand the influence of resonant tunneling to molecule electronic states. The results infer that photoexcited tunneling via plasmon decay may attach charge carriers to the molecule with energies close to the excitation energy which suggests that tunneling happens before significant dissipation in the metal.

2 Photochemistry

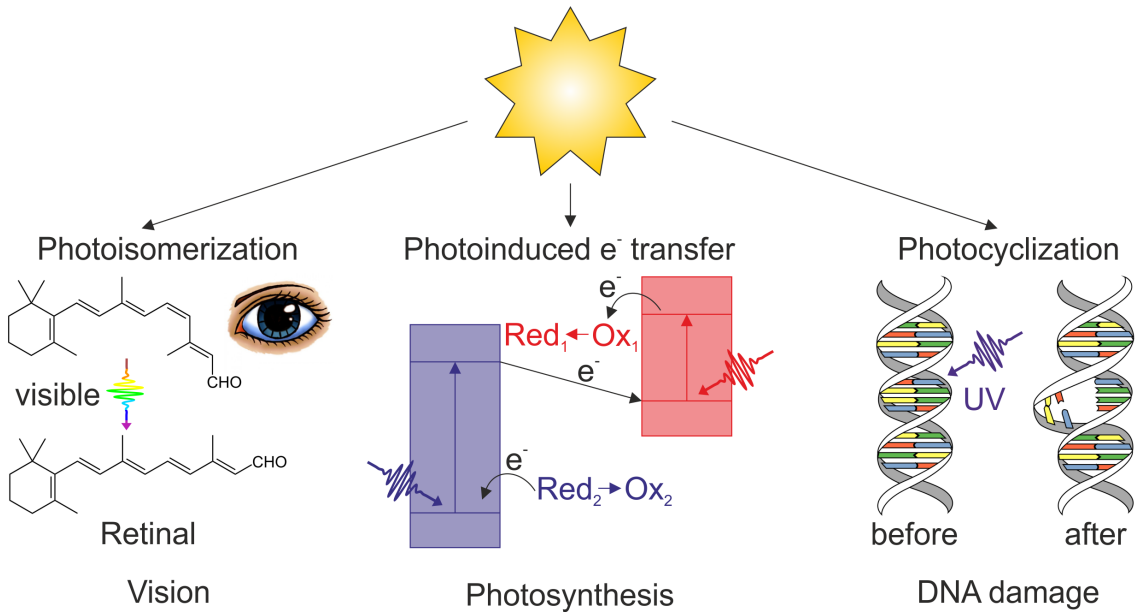

Figure 2.1: Examples of fundamental photochemical processes in nature, driven by sunlight.

Chemical reactions that occur under light are studied in the field of photochemistry. The light stimulus can drive reactions in a molecular excited state that may otherwise be forbidden in the ground state. Thus, photochemical pathways can reach thermally inaccessible states and overcome large activation barriers. This principle is fundamental for some of the most important biochemical reactions. Fig. 2.1 shows a graphic representation of only a few of the vital photochemical processes in nature. The *cis*→*trans* photoisomerization of the protonated Schiff base of 11-*cis*-retinal enables the sensation of vision in our bodies while photosynthesis, which is based on photoinduced electron transfer for water splitting and carbohydrate synthesis, enables the existence of life on earth itself by harvesting the sun's energy. On the other hand, the sun's ultraviolet (UV) radiation may damage the Deoxyribonucleic Acid (DNA) via photochemical cycloaddition, which may cause skin cancer, however, the same mechanism is responsible for vitamin D synthesis in our bodies. With regard to the huge potential that the implementation of photochemical conversion in artificial systems holds, it has become an active research field in science and technology.

2.1 Gas Phase and Solution

Control of photochemical reactions require a basic understanding of the principles that govern light-matter interaction and detailed knowledge of molecular dynamics in the electronically excited states. The Grotthus-Draper law states that only absorbed light may

induce photochemical changes of a compound. It was later found that light absorption by a molecule is quantized and hence, the absorption of one photon results in the activation of one molecule, which is described in the Stark-Einstein law. While seemingly obvious today, these findings were non-trivial at the time and form the basis of a mechanistic description of photochemical phenomena.
In a gas phase or solution, individual molecules are considered to be isolated, so that photonic energy may solely be transferred via direct absorption. The fundamental processes that may occur upon photon absorption are illustrated by considering a simple model of a diatomic molecule (e.g. Cl_2 or Br_2). Fig. 2.2(a) depicts the schematic potential energy landscape of a diatomic molecule as function of the bond length between the atoms. The molecule initially resides in its electronic ground state potential at the lowest vibrational level, if temperature induced effects are neglected. Photon absorption (A) rapidly promotes the molecule into an excited electronic state, before the atomic nuclei can follow the accompanied rearrangement of electron density and therefore the absorption strength is governed by wave function overlap of initial and final vibrational level, known as the Franck-Condon principle. Within a single particle formulation, the excitation rate $R_{i,f}$ between an initial and final state with respective wave function ϕ_i and ϕ_f is described by Fermi's golden rule:

$$R_{i,f} = \frac{\pi e}{imh\nu} \left|\langle \phi_f \left|\mathbf{E}\boldsymbol{\mu}\right| \phi_i\rangle\right|^2 \delta\left(\Delta E_{i,f} - h\nu\right) \tag{2.1}$$

where e and m are charge and mass of an electron, $h\nu$ is the photon energy, $\mathbf{E}$ is the electric field vector, $\boldsymbol{\mu}$ the transition dipole moment and $\Delta E_{i,f}$ the energy difference between the initial and final states. The δ-function enforces the resonance condition $\Delta E_{i,f} = h\nu$, while $\left|\langle \phi_f \left|\mathbf{E}\boldsymbol{\mu}\right| \phi_i\rangle\right|^2$ weights the absorption strength which is determined by the wave function overlap between initial and final state. Following the photon absorption, vibrational energy may dissipate within the excited state and relax the molecule to the vibrational ground state level. Radiative decay via fluorescence (F) relaxes the molecule to the electronic ground state, following again the Franck-Condon principle. This decay path does not involve a chemical change of the reactant. However, as the excited state usually exhibits an antibonding character, a sufficiently energetic absorbed photon or collisional activation can populate higher vibrational states and induce scission of the interatomic bond. For molecule cleavage, the reaction coordinate coincides with the bond length. When a wavepacket explores a higher vibrational level in the excited state, the bond length increases to an extent where the bond breaks, thus demonstrating a simple example of photochemistry.
For larger compounds which are comprised of more than two atoms, the simple one-dimensional spatial representation is not retained as the relevant potential landscape becomes multi-dimensional, so that the spatial representation of electronic states is neglected. Fig. 2.2(b) shows a Jablonski diagram which illustrates the relevant states without a spatial coordinate. The molecule is excited from the ground state (S_0) to a higher electronic state (S_i>0) via photon absorption. Internal conversion (IC) drives the system from higher excited states to the first excited state, according to Kasha's rule, before radiative via fluorescence or non-radiative emission dissipates the absorbed energy. Intersystem crossing (ISC) describes a spin flip of the excited electron which yields a transition from a singlet (S) to a triplet state (T), from where the system relaxes via non-radiative or slow radiative decay by phosphorescence (P). All non-radiative decay may occur via intermolecular energy transfer to surrounding molecules, thus activating these molecules for a chemical reaction or via intramolecular vibrational relaxation which couples to a specific reaction

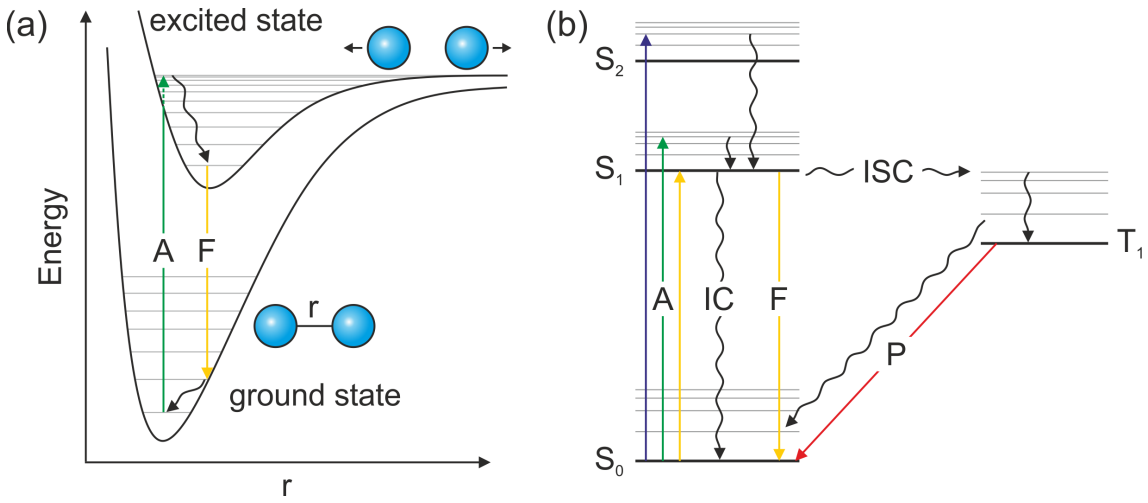

Figure 2.2: (a) Schematic potential landscape of a diatomic molecule as function of the bond length. Photon absorption (A) excites the molecule from the ground to the excited state potential energy surface which leads to bond scission or decays via vibrational relaxation and ends up in radiative decay via fluorescence (F). (b) Jablonski diagram of a polyatomic molecule. Photon absorption yields an excitation between singlet electronic states (S_i) which can non-radiatively decay by internal conversion (IC) or radiatively via fluorescence. An electron spin flip brings the molecule into a triplet state (T_1) via intersystem crossing (ISC) from which slow radiative decay occurs via phosphorescence (P).

coordinate of the molecule.

Many excellent studies have revealed manifold photochemical conversion mechanisms, including among others cycloaddition, ring-opening and -closing, isomerization, bond cleavage and H abstraction [14–19]. As this work focuses largely on photoinduced H transfer, one example that illustrates the concept is presented in more detail. The enol-keto conversion in compounds including an H-chelate ring in their structure is driven by photon absorption mediated excited state proton transfer [20]. Fig. 2.3 shows an H-chelate ring as part of a molecule in the enol form (O-H bond), which is stable in the electronic ground state. Upon photon absorption, the molecule is found in an electronically excited state and vibrational energy decays to skeletal vibrations, which reduces the reaction barrier for the enol-keto conversion, thus facilitating a unidirectional excited state conversion [21, 22]. After the initial Franck-Condon transition, the wavepacket accelerates along the vibrational coordinate, thereby causing an in-plane bending of the molecule skeleton which results in a modulation of the N···H-O distance. This modulation effectively reduces the barrier along the reaction coordinate and the molecule reacts to the keto form, which is the excited state potential minimum. Subsequent radiative and non-radiative decay relax the molecule to its electronic ground state from where it transfers back to the enol configuration, along the ground state potential which is barrierless along the reaction coordinate [23, 24]. This example illustrates the capability of light-induced reactions to reach thermally inaccessible chemical products via excited state pathways.

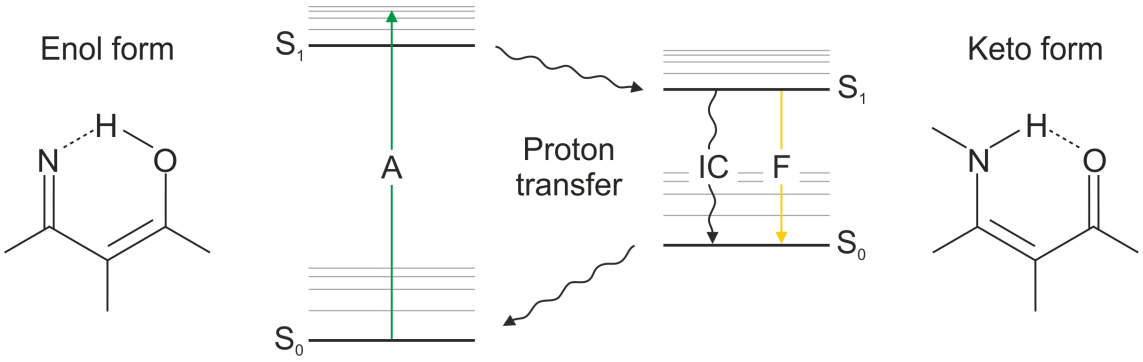

Figure 2.3: Photochemical conversion from enol to keto form. Photon absorption (A) promotes the molecule to an excited state potential and vibrational decay diminishes the barrier along the enol-keto reaction coordinate, thus facilitating a unidirectional excited state proton transfer reaction. (Non-)radiative decay (IC, F) and subsequent ground state proton transfer brings the molecule back to the enol form. (Adopted from [25])

2.2 Photochemistry on Metal Surfaces

When a molecule adsorbs on a metal surface, new degrees of freedom open up for manipulating and controlling photochemical properties.
Depending on the molecule-surface interaction, electronic and structural properties of the molecule is, however, heavily perturbed by orbital mixing and accompanying molecular reorientation, thereby altering available excitation and reaction paths. In the rare case of a very weakly bound molecule, the photon energy dependent excitation rate follows Eq. 2.1, analogous to the gas phase, thus following a direct excitation between molecular orbitals. Generally, this premise is not fulfilled and the photochemical process is governed by substrate mediated channels, which can indirectly excite the molecule via charge carrier attachment. Fig. 2.4(a) depicts a schematic representation of possible excitations on a metal surface. While a direct Highest Occupied Molecular Orbital (HOMO)-Lowest Unoccupied Molecular Orbital (LUMO) transition (mechanism 1) is rarely observed, the predominant excitation is from an initial state in the metal substrate either directly to a molecular orbital (mechanism 2), which can occur for very strongly bound molecules, or to a metal final state (mechanism 3) from which the charge carrier may attach to the molecule after transport and possible scattering. Since the lifetime of nascent excited charge carriers in noble metals is on the order of fs, scattering rapidly relaxes and thermalizes the initial photoeexcited energy distribution [26]. Fig. 2.4(b) shows the time evolution of the metal charge carrier distribution upon initial excitation. Directly after excitation, the distribution reflects the metal density of states but relaxes rapidly via electron-electron and subsequent electron-phonon scattering. If CW or quasi CW laser excitation is considered, the time averaged charge carrier distribution is constant as scattering and excitation reach a steady state. The accessible adsorbate states for charge carrier attachment are dependent on the initial photon energy and the number of scattering events before the charge carrier reaches the surface, while the generated number depends on the energy, polarization and incident angle dependent substrate absorption. The initiated chemical reaction in the molecule by charge carrier attachment can be regarded separated from the excitation process and relaxation in the substrate. Fig. 2.5(a) represents a model potential surface

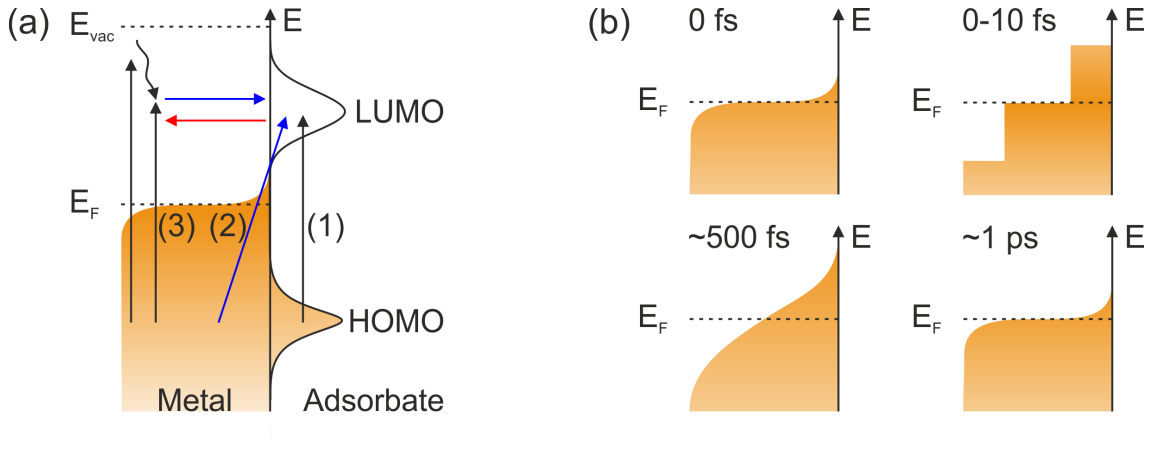

Figure 2.4: (a) Energy diagram of a prototypic molecular adsorbate on a metal surface. Different mechanisms may excite the molecule on the substrate. (1) direct HOMO-LUMO transition, (2) direct excitation of metal-adsorbate complex, (3) indirect excitation between metal states and subsequent scattering to adsorbate states. (b) Time-dependent photoexcited electron distribution. The initial Fermi-Dirac distribution (0 fs) is perturbed upon initial photoexcitation (0-10 fs) which relaxes primarily via electron-electron scattering (∼500 fs) and finally thermalizes by electron-phonon scattering (∼1 ps).

along the reaction coordinate of photo-induced desorption for a diatomic molecule (AB) adsorbed on the metal surface, as it was proposed by Menzel, Gomer and Redhead (MGR model) [27, 28]. Any of the above mentioned excitation processes promotes the molecule to an excited repulsive state potential, which is followed by vibration excitation and relaxation along the potential surface. Since the charged state lifetime is short, due to efficient coupling to substrate mediated relaxation channels, the photochemical reaction does usually not occur in the excited state, as the molecule returns to the ground state potential, before the reaction happens. If it gained enough kinetic energy in the excited state to overcome the reaction barrier, the reaction may occur. Otherwise, the energy is dissipated in the ground state potential. It should be emphasized that the deposited energy dissipates through many decay channels which may couple anharmonically in a multidimensional potential. The illustration along one reaction coordinate, however, reduces the complexity of the problem. The gained kinetic energy of the molecule may, for instance, excite the AB-stretch vibration. Fig. 2.5(b) shows the vibration harmonic potential as function of bond length. Upon excitation, the stretch vibration is excited and the molecule returns to the ground state potential. The desorbed molecule is then detected in a vibrationally excited state.

The resulting reaction yield, which quantifies the average number of reaction events per excitation attempt, is commonly expressed in photochemistry by means of a cross section, specific to a reaction product of interest, in this case the desorbed molecule. This cross section is dependent on excitation energy, adsorbate coverage, surface structure, composition and many other factors [2]. It may be determined by measuring the change in concentration of the reactant $d[AB]$ as function of incident photon fluence n_{ph}, provided that the reaction obeys a first-order rate law, i.e. the reaction yield is dependent on a single reactant concentration and linearly dependent on photon fluence. Regardless of the involved excitation mechanism, only the final reaction product is considered, which is here the des-

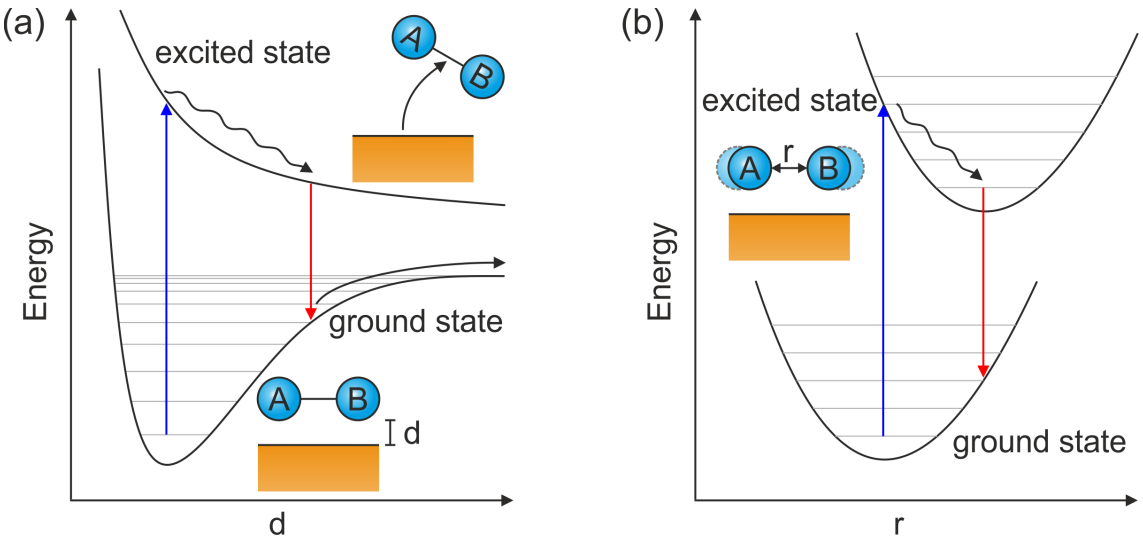

Figure 2.5: (a) Schematic of potential energy surface as function of the molecule-metal bond distance d. The molecule AB is excited to a repulsive potential and efficiently quenched to the ground state. If enough kinetic energy was gained, it may desorb from the surface. (b) Harmonic potential along the AB bond length r. Vibrational energy is gained by dissipation of the inital excitation. (Adopted from [2])

orbed molecule. Therefore, the change in adsorbate concentration is solely dependent on photon fluence:

$$\frac{d[AB]}{d[n_{ph}]} = -\sigma[AB] \tag{2.2}$$

where σ is the photodissociation cross section. Experimentally, it is determined from the initial reactant concentration $[AB]^0$ and the measured concentration at different photon fluences:

$$\sigma n_{ph} = ln\left(\frac{[AB]}{[AB]^0}\right) \tag{2.3}$$

The presented concept is transferable to other reactions, given that the above premises are fulfilled.

2.3 Surface Plasmons for Chemical Energy Conversion

Departing from the mature field of photochemistry on flat metal surfaces, more recently, the possibility of exploiting plasmonic excitations of metallic nanostructures for photochemical processes, specifically photocatalysis has sparked large interest to transfer the presented concepts to the emerging field of plasmon-driven photochemistry [7, 8, 10].
This section focuses on the physical concept of plasmonic excitation in metallic nanostructures and the resulting generation of photoexcited charge carriers which drive chemical

reactions on the surface. A brief overview of precedent-setting studies in the field provides a broader context for the research presented in this work.

2.3.1 Localized Surface Plasmon Resonance

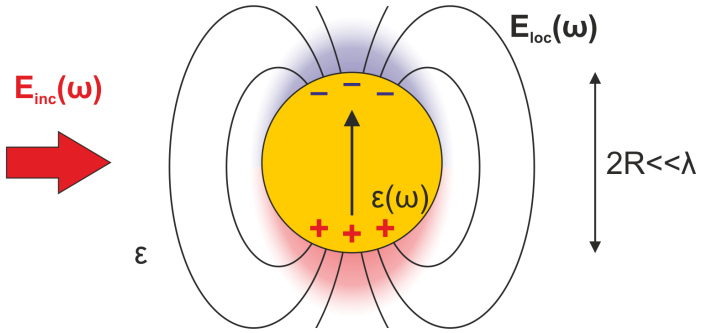

Figure 2.6: Schematic of an illuminated metal nanoparticle (radius R) by an oscillating incident electric field $\mathbf{E}_{inc}(\omega)$. The particle and surrounding medium are characterized by the dielectric constant $\epsilon(\omega)$ and ϵ, respectively. The induced dipole moment oscillation creates an evanescent field $\mathbf{E}_{loc}(\mathbf{r},\omega)$

The easiest and most instructive way to understand the interaction of light with metallic nanostructures is to consider an illuminated metallic particle, which is much smaller than the incident wavelength λ. In this situation, all surface valence electrons in the particle oscillate collectively at the frequency of the incident field and we can use the quasi-static approximation. The interaction of the particle with an incident electromagnetic field $\mathbf{E}_{inc}(\omega)$ is readily understood by approximating the particle with an effective dipole located at the center (Fig. 2.6). The induced dipole is described by [29]:

$$\mathbf{p}(\omega) = \epsilon\alpha(\omega)\mathbf{E}_{inc}(\omega) \tag{2.4}$$

where ϵ is the dielectric constant of the surrounding medium (ϵ=1 in air/vacuum) and $\alpha(\omega)$ the light frequency dependent polarizability:

$$\alpha(\omega) = 4\pi\epsilon_0 R^3 \frac{\epsilon(\omega) - \epsilon}{\epsilon(\omega) + 2\epsilon} \tag{2.5}$$

where ϵ_0 is the vacuum permittivity, $\epsilon(\omega)$ the incident frequency dependent dielectric constant of the particle material and R the particle radius.
The interaction of the induced dipole with the incident electric field results in a spatially confined local electric field in the particle vicinity:

$$\mathbf{E}_{loc}(\mathbf{r},\omega) = \mathbf{E}_{inc}(\mathbf{r},\omega) + \frac{1}{4\pi\epsilon_0}\frac{3(\mathbf{p}(\mathbf{r},\omega)\mathbf{r})\mathbf{r} - \mathbf{p}(\mathbf{r},\omega)}{r^3} \tag{2.6}$$

where $\mathbf{r}$ describes the radial position from the dipole center and r the corresponding scalar distance. Substitution with 2.4 yields:

$$\mathbf{E}_{loc}(\mathbf{r},\omega) = \mathbf{E}_{inc}(\mathbf{r},\omega) + \frac{\epsilon(\omega) - \epsilon}{\epsilon(\omega) + 2\epsilon}\left(\frac{R}{r}\right)^3 [3(\mathbf{E}_{inc}(\mathbf{r},\omega)\mathbf{r})\mathbf{r} - \mathbf{E}_{inc}(\mathbf{r},\omega)] \tag{2.7}$$

The local field intensity therefore rapidly decreases with distance from the particle, thus creating an intense, non-propagating near-field in its vicinity. The evanescent field results in a field enhancement which depends on the distance from the particle:

$$\frac{|\mathbf{E}_{loc}(\mathbf{r},\omega)|}{|\mathbf{E}_{inc}(\mathbf{r},\omega)|} = 1 + 2\left(\frac{R}{R+r}\right)^3 \frac{\epsilon(\omega)-\epsilon}{\epsilon(\omega)+2\epsilon} \tag{2.8}$$

The resonance condition of this simple shape is obtained from $\epsilon(\omega)+2=0$. This localized surface plasmon resonance (LSPR) is in the visible spectral range for noble metals [30]. For free electrons in metals, $\epsilon(\omega)$ is approximated under negligence of damping by the Drude model, where ω_p is the bulk plasma frequency:

$$\epsilon(\omega) = 1 - \left(\frac{\omega_p}{\omega}\right)^2 \tag{2.9}$$

The LSPR frequency is therefore given by:

$$\omega_{LSPR} = \frac{\omega_p}{\sqrt{3}} \tag{2.10}$$

At the resonance frequency, scattering and absorption are largely increased, which may be employed for focusing light into the nano-scale, thus overcoming the Abbe limit in conventional optics. This principle has been exploited in a number of applications including spectroscopy, non-linear optics, photodetection and solar energy harvesting [31–35].

2.3.2 Surface Plasmon Polariton

surface plasmon polariton (SPP) is the collective coherent oscillation of conduction electrons at a metal/dielectric interface which is coupled with an electromagnetic wave. It propagates along the interface but is confined along the normal direction [36]. Fig. 2.7(a) shows a schematic representation of an SPP propagating in x-direction along the metal boundary with an electric field E:

$$E_x = E_0 e^{i(k_x x + k_{z,n}|z| - \omega t)} \tag{2.11}$$

$$E_z = \pm E_0 \frac{k_x}{k_{z,n}} e^{i(k_x x + k_{z,n}|z| - \omega t)} \tag{2.12}$$

where E_0 is the electric field amplitude of the surface plasmon wave, k_x and k_z the wave vector in x- and z-direction, ω the wave angular frequency and t the time. The material interface is located at $z=0$, while $z<0$ is in the metal ($n=1$, $\pm$ is $+$) and $z>0$ is in the dielectric ($n=2$, $\pm$ is -). It follows from Maxwell's equations at the material interface:

$$\frac{k_{z,1}}{\epsilon(\omega)_1} + \frac{k_{z,2}}{\epsilon_2} = 0 \tag{2.13}$$

and

$$\epsilon_n \left(\frac{\omega}{c}\right)^2 = k_x^2 + k_{z,n}^2 \tag{2.14}$$

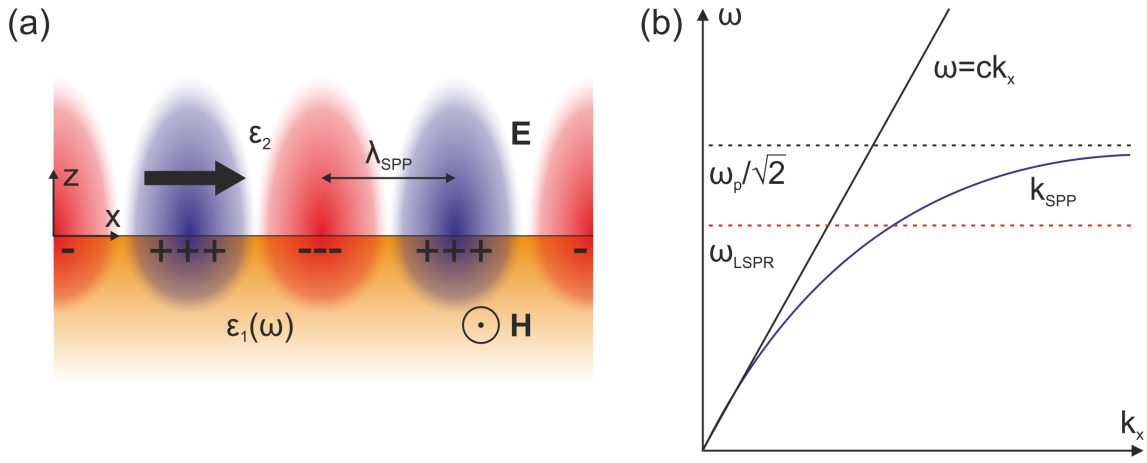

Figure 2.7: (a) Schematic of a propagating SPP with wavelength λ_{SPP} along a metal/dielectric interface. $\epsilon_1(\omega)$ and ϵ_2 are the dielectric constant of the metal and dielectric, respectively. Surface charge oscillation induces a bound electromagnetic field which penetrates into both media. (b) Dispersion relation of the SPP (k_{SPP}) with the light line ($\omega = ck_x$) indicated. The SPP dispersion approaches $\omega_p/\sqrt{2}$ at large k_x. Direct coupling between light and SPP mode may be achieved by a particle LSPR at the resonance frequency ω_{LSPR}.

The dispersion relation of the SPP along the interface follows from the above conditions as:

$$k_x = \frac{\omega}{c}\sqrt{\frac{\epsilon(\omega)_1\epsilon_2}{\epsilon(\omega)_1 + \epsilon_2}} \tag{2.15}$$

By assuming a real valued ϵ_2 and complex $\epsilon(\omega)_1$, then $k_x = k_x^{'} + ik_x^{''}$:

$$k_x^{'} = \frac{\omega}{c}\sqrt{\frac{\epsilon(\omega)_1^{'}\epsilon_2}{\epsilon(\omega)_1^{'} + \epsilon_2}} \tag{2.16}$$

$$k_x^{''} = \frac{\omega}{c}\left(\frac{\epsilon(\omega)_1^{'}\epsilon_2}{\epsilon(\omega)_1^{'} + \epsilon_2}\right)^{1.5}\frac{\epsilon(\omega)_1^{''}}{2(\epsilon(\omega)_1^{''})^2} \tag{2.17}$$

Fig. 2.7(b) depicts the real part of the dispersion relation as function of angular frequency. The surface plasmon does not directly couple to light, as the dispersion of free propagating light ($\omega = ck_x$) never crosses the SPP dispersion (k_{SPP}), it is therefore a non-radiative mode which asymptotically approaches $\omega_p/\sqrt{2}$, where ω_p is the plasma frequency, when the surrounding dielectric is air/vacuum ($\epsilon_2 = 1$). In order to excite an SPP with light, the wave vector mismatch at the given excitation frequency has to be overcome which may be achieved by different means, e.g. grating diffraction, attenuated total reflection, closely positioned metallic scanning tips, surface roughness or other structural inhomogeneities [36]. The LSPR of a metallic particle directly on the surface or within the particle near-field may also provide the necessary momentum to couple to the propagating SPP mode. Spatial confinement within the nanometer sized particle broadens the localized resonance in momentum space and may therefore transfer energy to the propagating mode, when excited at the resonance frequency (ω_{LSPR}).

2.3.3 Photocarrier Generation

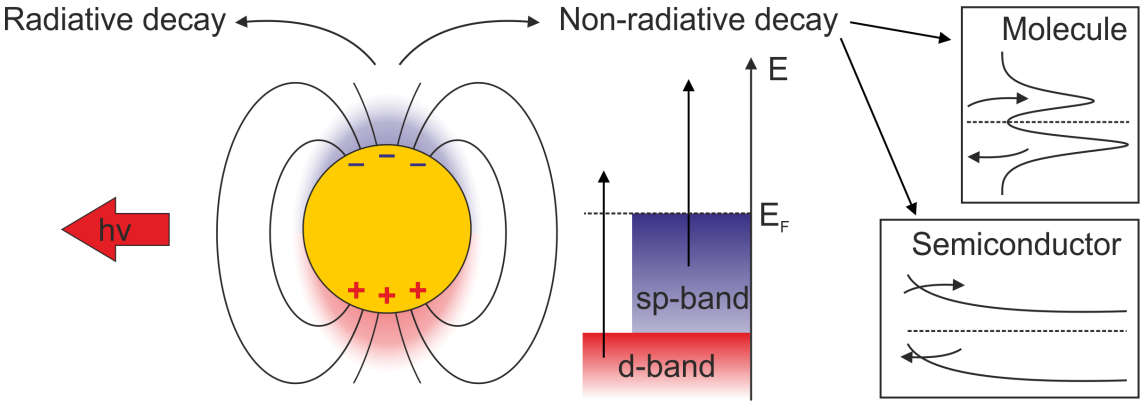

Figure 2.8: Decay channels of excited LSPR, generated in metallic nanoparticles. Radiative decay leads to photon re-radiation whereas non-radiative decay yields a non-thermal charge carrier distribution which may drive reactions in molecular adsorbates or be harvested at a semiconductor interface.

Surface plasmons decay rapidly on a few femtosecond timescale both radiatively via photon emission and non-radiatively via electron-hole pair excitation [26, 37, 38]. Fig. 2.8 depicts schematically the decay from a plasmonic particle. Radiative decay may be used to enhance the emission of nearby emitters, while non-radiative decay which proceeds both via inter- and intraband transitions in the metal provides energetic charge carriers which can be harvested by molecular adsorbates to drive chemical reactions or by semiconductors for use in photovoltaics and photoelectrochemical systems [7, 39–42]. Landau damping leads to dephasing of the initial plasmonic excitation and the formation of a photoexcited charge carrier distribution, similar to the scheme depicted in Fig. 2.4(b) after tens of femtoseconds. The created energy distribution of hot carriers depends on the plasmon frequency, the particle size, plasmon mode symmetry and material electronic structure [43]. Scattering of excited charge carriers gradually leads to a thermal distribution and energy dissipation to the nanoparticle lattice or the substrate which supports the particle. However, as the surface to bulk ratio is large in nanoparticles, a significant fraction of non-thermalized charge carriers reach the surface with high energies and can be transferred to electronic states at an interface formed by molecules or by a semiconductor. For noble metals, the initial charge carrier distribution is dominated by interband transitions, if those are available at the specific plasmon resonance. Below the interband threshold, either phonons need to provide the necessary momentum to excite electrons within the sp-band or the spatial confinement of electronic states in nanoscopic systems leads to an inverse effect in momentum space, thus softening the restrictions imposed by the uncertainty principle. Above the interband threshold, direct d- to sp-band transitions dominate. Fig. 2.9 shows the calculated charge carrier distribution from surface plasmon decay for the materials Au and Cu, which were used throughout this work. The transition from deep-lying d-bands at ∼-2 eV to the conduction band creates high-energy holes and low-energy electrons in this regime while the distribution is similar below the interband transition which must be taken into account for subsequent charge carrier harvesting [44]. In the reproduced study, the decay was calculated from a traveling surface plasmon polariton but the results are transferable also to localized resonances as geometric effects were found to only be significant below

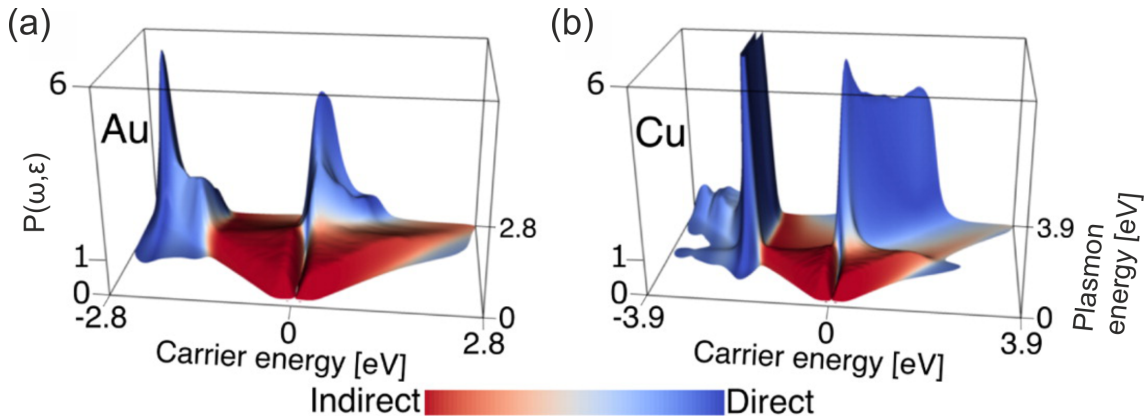

Figure 2.9: Photoexcited charge carrier distribution resulting from plasmon decay via intraband (indirect) or interband transitions (direct) as function of plasmon frequency (ω) and carrier energy (ϵ) for (a) Au and (b) Cu. (Reprinted figure with permission from Brown *et al.*, ACS Nano **2016**, 10(1), 957-966 [26]. Copyright 2016 by the American Chemical Society. Adapted with permission of the author.)

a particle radius of ∼10 nm. Even though charge carriers are generated primarily at the positions of highest surface electric field, they may travel ballistically and diffusively within the metal. Energetic charge carriers have a shorter lifetime and mean free path, so that scattering dissipates their energy after only ∼10 nm [31]. The maximum carrier mean free paths of ∼50 nm are similar in all noble metals so that photoexcited carriers within this spatial range may attach to an adsorbate of interest to induce a chemical reaction before thermalization [26]. It is therefore highly desirable to collect charge carriers within ∼10 nm to make use of their high energies in molecular reactions or photoelectrochemical cells [7].

2.3.4 Plasmon Mediated Chemistry

The possible resonant enhancement of both physical and chemical processes within the concentrated surface electromagnetic field of a metallic nanostructure has attracted increasing attention because of its application for surface-enhanced techniques. Coupling and energy transfer to the nanostructure environment can be exploited through different surface plasmon relaxation channels. Resonant light-induced heating due to energy dissipation to lattice phonons is used to locally confine a heating source. However, this process only leads to considerable temperature increase at high radiation intensities and does not offer the advantage to drive thermally inaccessible processes, which is a great benefit of photochemical processes [10]. It is therefore only briefly mentioned here that plasmonically enhanced heating has primarily impacted medical applications, where localized heat-induced destruction of carcenomas in the vicinity of nanoparticles was reported, thus offering the possibility to locally destroy cancer cells while leaving healthy tissue unharmed [45–47].
The electric field on the surface of the nanostructure further directly increases light-matter interaction of nearby absorbers and emitters. It was demonstrated that this concept can be used to tune the absorption and fluorescence of molecules via coupling and hybridization

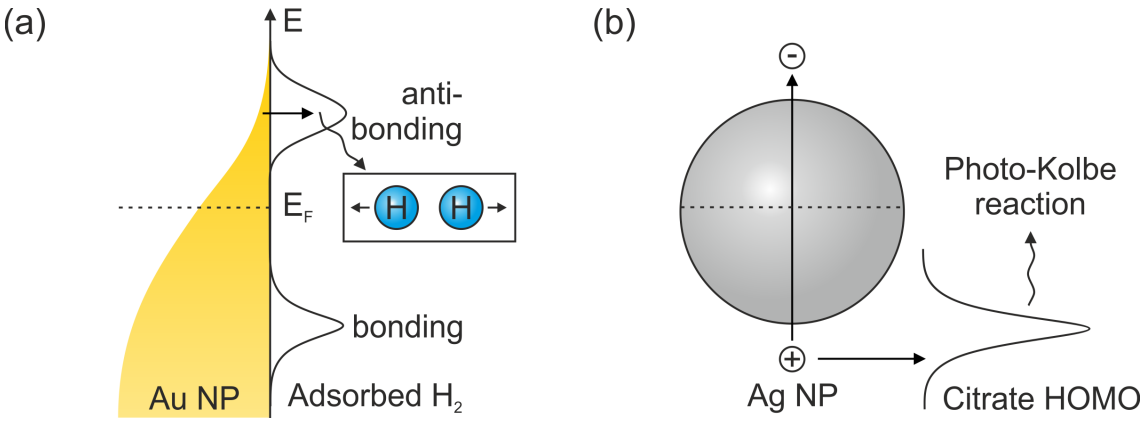

Figure 2.10: Schematic of nanoparticle (NP) LSPR mediated reactions (a) H_2 dissociation occurs via transfer of an electron from a non-thermalized photoexcited electron distribution in the gold nanoparticle to an antibonding molecular orbital (adopted from [40]). (b) Ag nanoparticle growth by photoexcited hole transfer from the Ag to the citrate HOMO, thus oxidizing the citrate and reducing Ag^+ ions at the particle (Photo-Kolbe reaction) (adopted from [9])

with the LSPR [48–51]. Perhaps the most important application is the development of Surface Enhanced Raman Spectroscopy (SERS), in which Raman scattering from molecules adsorbed on nanostructures is increased by as much as $\sim 10^{10}$ on plasmonic nanostructures [52–55]. While the exact enhancement mechanism is still under debate, it is commonly accepted that both electromagnetic enhancement from LSPR excitation as well as chemical enhancement through the formation of a charge transfer complex contribute to the Raman process [56]. The High enhancement factor is achieved as both incoming and scattered light are magnified, resulting in a quartic scaling of the Raman signal with electric field. For chemisorbed molecules, metal-adsorbate charge transfer, similar to the situation depicted in Fig. 2.4, can further lead to a population of molecular states, from where spectroscopic transitions may occur [57, 58].
While spectroscopic applications benefit primarily from the near-field itself, most photochemical reactions on metal nanostructures are mediated by charge carriers that are generated via plasmon decay. The combination of noble metal particles with semiconducting layers has been employed since early experiments of photochemical water splitting on metal-oxide electrodes which was first demonstrated with UV light and expanded to the visible spectrum via metal-semiconductor charge transfer [59–63]. Based on the observation of non-thermal optically excited reaction pathways on flat metal surfaces, the adoption of photochemical concepts for selective catalysis has furthermore been a driving force for departing from well-defined flat to particle decorated surfaces [3]. Plasmon mediated reactions are generally able to be path selective due to specific population of adsorbate resonances as non-thermal charge carrier distributions can be maintained with a longer lifetime than on extended surfaces [43, 64, 65]. It is therefore possible to toggle between reaction mechanisms like desorption, dissociation or translation by tuning properties of the catalyst or the excitation [8].

Two examples of photoexcited electron- or hole-induced reactions are presented here. Fig. 2.10(a) shows the schematic reaction mechanism of H_2 dissociation at a Au nanoparticle [40, 66]. As the molecule only weakly interacts with the surface, it is kept close to the particle by the presence of a porous oxide layer of either TiO_2 or SiO_2, which is only

uninvolved in the reaction and therefore not depicted in the schematic. The non-thermal electron distribution that follows an initial plasmon resonant photoexcitation reaches energies as high as the H_2 antibonding orbital to which it may attach to induce the dissociation reaction. There are no competing reaction pathways for this very simple molecule. Fig. 2.10(b) depicts the photoexcited hole driven reduction of a Ag nanoparticle which results from the citrate ion oxidation within the surrounding solvent (Photo-Kolbe reaction) [9, 67]. The negative charging of the nanoparticle upon optical excitation brings Ag^+ ions into solution which attach again to particles due to Coulomb interaction. While the electron driven H_2 dissociation was observed to follow the plasmon resonant absorption, the plasmon induced Ag particle growth does not image the absorption but increases monotonically with incident energy. It was argued that holes with higher energies are more strongly oxidizing and thus counteract the off-resonant decreasing absorption with larger excitation energy. Even though the mechanism is not entirely understood, both hole and electron harvesting may prove useful in future applications, as it was demonstrated that devices which combine plasmonic metal nanoparticles and semiconductors in a photoelectrochemical cell can use both carrier polarities in the half-reactions of water splitting and are therefore able to mimic photosynthesis [42]. However, the understanding of fundamental steps involved in photochemical reactions remains far from complete as yield, energy distribution as well as dynamics of photoexcited charge carriers and the resulting reaction yield within a molecular adsorbate remain unclear [8]. As nanoparticles form complex agglomerates with usually unknown geometry, the spatial and spectral variation of the plasmonic response and photoexcited charge carrier distribution is merely observable within an average by monitoring the reaction product yield. Microscopic access at the fundamental level of single nanoparticles and molecules has not been achieved and it remains a challenging task to relate the plasmonic response with the resulting charge carrier distribution and excited reaction pathways within single molecules [10].

3 Method: Combination of STM with Optical Excitation

This section outlines the working principle of STM, combination with laser excitation, and sample/tip preparations employed in this work.

3.1 Electron Tunneling in an STM

Shortly after its development by Binnig and Rohrer in 1982, scanning tunneling microscopy has developed into one of the most important surface science tools due to its ability to resolve single molecules/atoms [68]. Related techniques, such as local spectroscopy, potentiometry and atom manipulation have since then expanded its capabilities and provide a large tool set to investigate surface properties at the fundamental level [69–72].
The STM relies on electron tunneling to image conductive surfaces. At sub-nanometer distance between the STM tip and a metal substrate, electrons can tunnel through a finite barrier formed by the vacuum gap between an atomically sharp tip and a conductive surface. In this situation, a measurable current is obtained when a bias voltage is applied between the tip and sample.

The one dimensional current between a spherical STM tip and a planar sample can be calculated when weak coupling is assumed (∼9 Å separation) by using a first-order perturbation theory [74, 75]:

$$I = \frac{2\pi e}{\hbar} \sum_{\mu,\nu} \left(f(E_\mu) \left[1 - f(E_\nu \right] - f(E_\nu) \left[1 - f(E_\mu) \right] \right) \left| M_{\mu\nu} \right|^2 \delta(E_\nu + V - E_\mu) \tag{3.1}$$

where $f(E)$ is the Fermi distribution function, V the applied voltage, $M_{\mu\nu}$ the tunneling matrix element between states of tip ψ_μ and surface ψ_ν and E_μ / E_ν the energy of ψ_μ / ψ_ν. In the low temperature limit, the Fermi distribution functions can be replaced by a step function. At low applied voltage, the formalism further reduces to:

$$I = \frac{2\pi}{\hbar} e^2 V \sum_{\mu,\nu} \left| M_{\mu\nu} \right|^2 \delta(E_\mu - E_F) \delta(E_\nu - E_F) \tag{3.2}$$

where E_F is the Fermi energy. In order to understand the fundamental factors that govern the tunneling process, the tip is approximated by a point probe at position $\vec{r}_0$ with arbitrarily localized wave function, so that $M_{\mu\nu} \propto \psi_\nu(\vec{r}_0)$. The tunneling current is within this approximation solely dependent on the tip and surface local density of states at the Fermi energy and position $\vec{r}_0$ [76]:

$$I \propto \rho_T(E_F) \sum_{\nu} \left| \psi_\nu(\vec{r}_0) \right|^2) \delta(E_\nu - E_F) \equiv \rho_T(E_F) \rho_S(\vec{r}_0, E_F) \tag{3.3}$$

Modeling the tip by a spherical potential with radius R yields the well-known exponential current dependence with regard to tip-sample distance d:

$$I \propto \left| \psi_\nu(\vec{r}_0) \right|^2) \propto exp(-2k(R+d)) \tag{3.4}$$

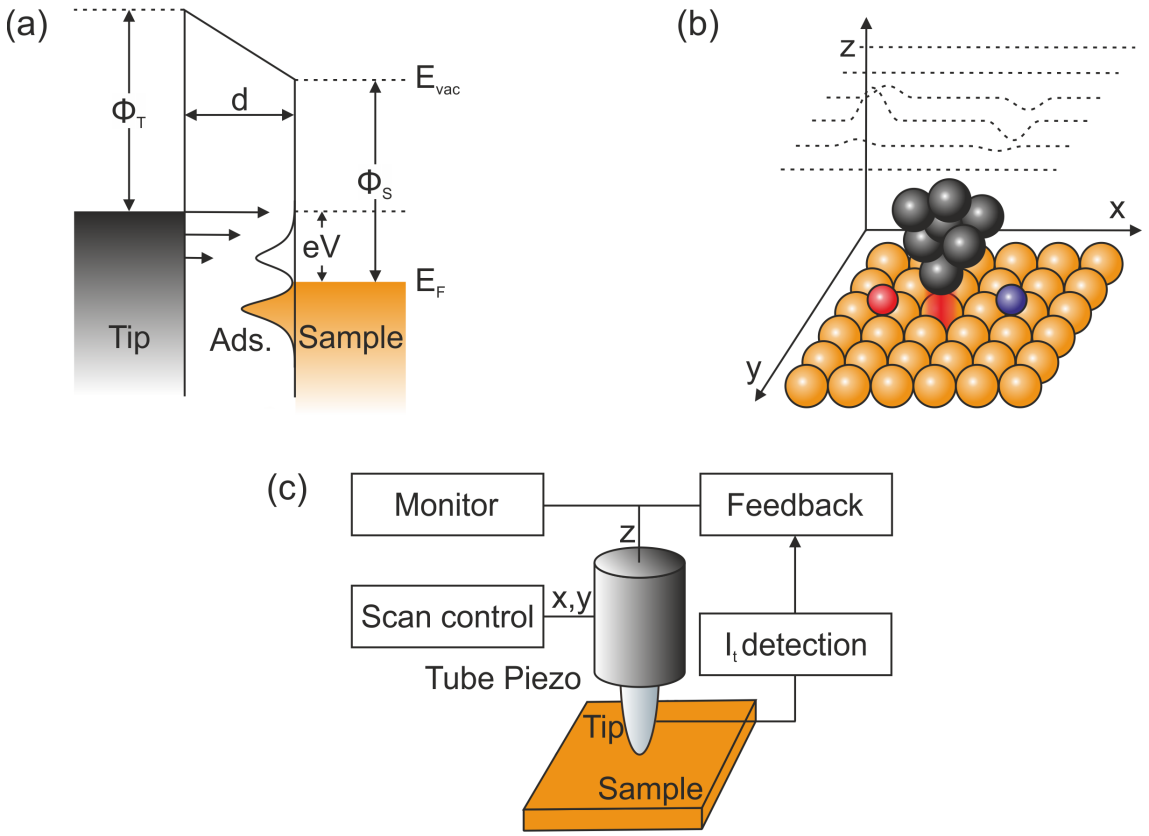

Figure 3.1: (a) Energy diagram of biased STM junction with adsorbate. (b) Tip scanning a surface with different adatoms (blue and red sphere). In constant current mode, adatoms appear as protrusion and depression in topography, according to their induced variation in local density of states. (c) Schematic representation on an STM. ((b),(c) adopted from [73])

$$k = \sqrt{\frac{2m\phi}{\hbar^2}} \tag{3.5}$$

where k is the inverse decay length, m the electron mass and ϕ the effective local work function. The tunneling current within an applied bias window is roughly estimated from the above relations [77]:

$$I \propto \int_{E_F}^{E_F+eV} \rho_{Tip}(E-eV)\rho_{Sample}(E)T(d,eV,E)dE \tag{3.6}$$

$$T(d,eV,E) \cong exp\left(-\frac{2d\sqrt{2m}}{\hbar}\sqrt{\frac{\phi_S+\phi_T}{2}+\frac{eV}{2}-E}\right) \tag{3.7}$$

where $T(d,eV,E)$ is the transmission function and ϕ_T, ϕ_S the local work function of the tip and sample, respectively. Fig. 3.1(a) depicts the energy diagram of a negatively biased metallic sample with tunneling current flowing from tip to sample. The local density of states is modified by an adsorbate on the surface, which induces a spatially confined variation of the tunneling current, hence creating a contrast between the recorded current

at different positions. Fig. 3.1(b) shows a schematic of an STM. The scanning motion of the tip is controlled by a piezo tube scanner, which provides precise motion in three spatial dimensions to scan the tip across a sample. The tip is scanned over a conductive surface while the vertical motion is controlled by a feedback loop to obtain a topography of the surface. In the constant current mode, the tunneling current, which flows upon bias application, is checked against a set value and the vertical tip position is adjusted to match them, while in the constant height mode, the vertical tip position is fixed and only the spatial variation in tunneling current is recorded. Real-space topographic imaging is realized in this way by monitoring the feedback voltage or tunneling current as function of applied voltages to lateral scanning piezos. Fig. 3.1(c) represents a sketch of the atomistic details in the STM junction, where the tunneling current is dominated by the foremost tip apex atom and individual surface atoms. During surface scanning, the variation in tunneling current and resulting vertical tip displacement is induced by variation in topography and local density of states, e.g. from adsorbed atoms or molecules. The recorded image is thereby not a directed representation of the surface topography but convoluted with available electronic states to tunnel into, which is directly apparent from Eq. 3.6. Therefore, different adsorbed species may result in protrusions (red sphere) or depressions (blue sphere) in the acquired image.

3.2 STM Setup

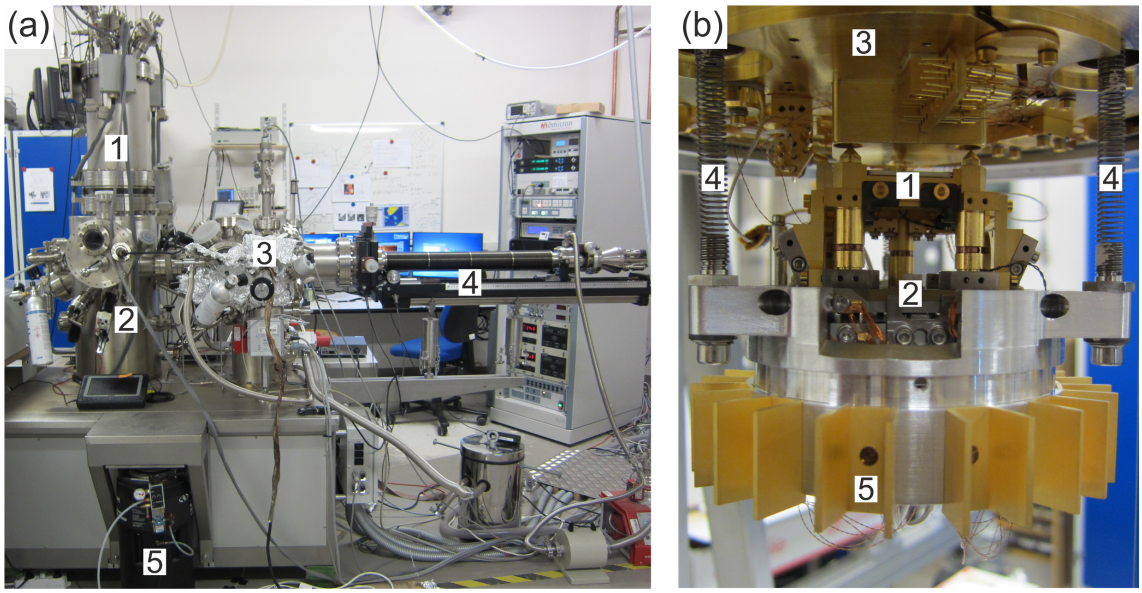

Figure 3.2: (a) Low-temperature Omicron SPM system with main components labeled 1: cryostat, 2: SPM chamber, 3: preparation chamber, 4: manipulator, 5: air damped stage. (b) Close-up of dismantled SPM head with main components labeled 1: cryostat bottom, 2: sample reception, 3: scan piezo, 4: suspension springs, 5: eddy current damper.

All work presented here was performed on a customer modified, commercial low-temperature Omicron SPM system with Nanonis control electronics from Specs GmbH [78, 79]. Fig. 3.2(a)

shows a photograph of the employed setup, situated in our lab at the basement in order to reduce vibrations that stem from structural vibrations of the building. The system consists of a cryostat (label 1) for liquid He and liquid N cooling, a main chamber, where the SPM head (label 2) is located, a preparation chamber (label 3) for sample preparation, a manipulator (label 4) for sample transfer from the preparation to the main chamber and an air damped stage (label 5), to isolate the SPM from external mechanical noise. ultra-high vacuum (UHV) conditions of $\sim 10^{-10}$ mbar are realized by pumping the preparation chamber with a turbo-molecular and an ion pump and pumping the main chamber with another ion-pump. Titanium sublimation may further reduce the pressure via gas adsorption whereas the cryostat surface acts as a cold trap for residual gases.
The preparation chamber is equipped with a load-lock for tip and sample transfer into UHV while it is separated from the main chamber by a gate valve to keep contaminations from transfer and sample preparation located in the preparation chamber. Samples and tips are transferred with a motorized manipulator into the main chamber, where they are passed to a wobble stick and stored in a sample garage. Within the main chamber, the SPM head is thermally isolated with two cooling shields which can be opened to insert samples and tips, where they are cooled down to cryogenic temperatures via thermally conductive contact to the cryostat and may subsequently be used for measurements.
Fig. 3.2(b) shows a photograph of the dismantled SPM head. The head is closely attached to the bottom of the cryostat (label 1) to ensure optimal thermal contact. Sequential cooling with liquid He and liquid N results in a temperature of $\sim$5 K, while radiative heating from the surrounding surfaces is suppressed by encapsulating the head with two surrounding shields, which are detached in the photograph. After transfer of a scanning tip into the sample reception (label 2), it may be placed onto the piezo crystal (label 3), which facilitates precise three dimensional motion of the scanning tip. A sample of interest is then placed into the sample reception for measurement. Vibrational isolation of the SPM head from the cryostat is ensured by a spring suspension (label 4) at the cryostat bottom and eddy current damping (label 5). Higher frequency noise is damped by the rigid design of the SPM head itself. The springs may be toggled between a clamped and unclamped configuration. The former pushes an attached Cu block against the cryostat for efficient cooling whereas the latter releases it for optimal vibration isolation during operation.

3.3 Sample Preparation

We employed single-crystal copper surfaces with 0.1° accuracy and 10 nm roughness from MaTeck GmbH [80]. Fig. 3.3(a) and (b) depict the atomic structure of the (111) and (110) surface orientation, respectively, including important crystallographic parameters. After entry of the samples into the preparation chamber from the load lock, they are transferred onto the manipulator. The metal surfaces are cleaned on the manipulator heating stage by repeated cycles of sputtering and annealing. A sputter gun is attached at the preparation chamber together with an Ar gas pressure bottle. For sample sputtering, an Ar partial pressure of 5×10^{-6} mbar is let into the chamber via a needle valve. Gas atoms ionize and accelerate in direction of the sample surface upon application of 1.5 kV high voltage for about 20 minutes. The resulting ion bombardment removes the topmost atomic layers and contaminations from the sample surface and creates a restructured surface morphology, which is converted back to an atomically defined configuration by heating the sample to

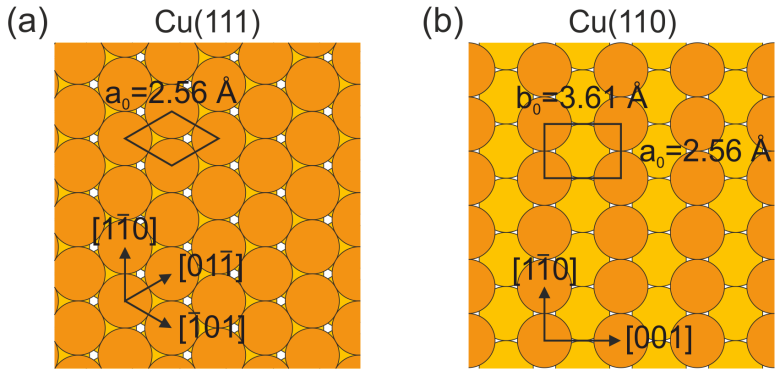

Figure 3.3: Schematic illustration of the (a) Cu(111) and (b) Cu(110) surface atomic structure. The unit cell with lattice constants a_0 and b_0 is indicated. High symmetry axes are marked with their crystallographic directions.

700-800 K for another 20 minutes. This procedure is repeated until surface contaminations are almost completely removed and the surface appears clean in STM images.
The subsequent evaporation of investigated molecules onto the clean Cu surface is performed differently for the relatively heavy porphycene molecule, which is available in form of a powder and the lighter H_2O and CH_3OH molecules, which are liquid at room temperature. Porphycene is evaporated from a Knudsen cell of a UHV temperature controlled Kentax evaporator [81]. The evaporation onset was found to be about 160°C but depends strongly on the amount of molecules in the crucible. For direct monitoring of the evaporation rate, a quartz micro-balance which oscillates at about 6 MHz is positioned in front of the crucible opening. The oscillation resonance frequency shifts upon molecular adsorption, thereby indirectly indicating the amount of molecules with evaporation duration, which is subsequently referenced to an obtained molecular coverage, observed by STM imaging. The sample is kept at room temperature during evaporation.
H_2O and CH_3OH are deposited by direct evaporation into the main chamber. The clean sample is introduced into the SPM head and cooled down to cryogenic temperatures to increase the sticking coefficient for small deposited molecules. After opening the cooling shields, the temperature rises to ∼12 K. A flask of the respective liquid is attached via a valve to a turbo-molecular pump. The contained liquid is frozen with closed valve by using liquid nitrogen and subsequently the flask volume is pumped to reduce the partial pressure of contaminants with higher melting point. This is repeated for purification of the precursor molecules which are then dosed from a needle valve into the main chamber at a partial pressure of $\sim 5\times10^{-8}$ mbar for 30-60 seconds to obtain a coverage much below a monolayer.

3.4 Tip Preparation

Scanning tips from polycrystalline W and Au wire were fabricated by electrochemical etching. Furthermore, tips were subsequently polished and structured by focused ion beam treatment to engineer the tip geometry and achieve desired optical properties.

3.4.1 Electrochemical Etching

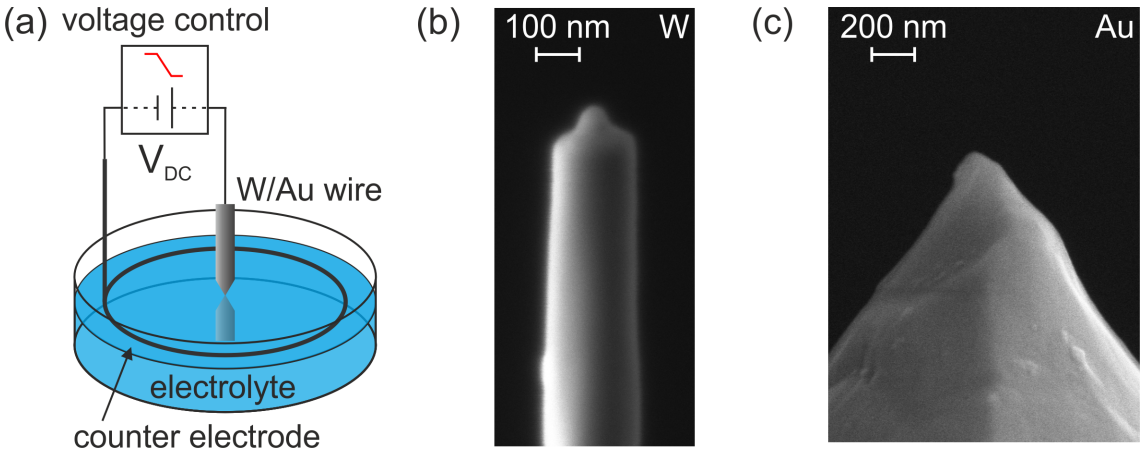

Figure 3.4: (a) Schematic of setup for electrochemical tip etching. W and Au tips were etched with KOH or HCl electrolyte solution, respectively. SEM micrograph of an etched (b) W tip with apex radius ∼20 nm and (c) Au tip with apex radius ∼20 nm. ((a) adopted from [82])

Usually, W or PtIr(80:20) are used as scanning tip materials for STM experiments, as these stiff metals provide mechanical stability for low-noise operation and a flat density of states around the Fermi level. However, for optical applications that exploit plasmonic resonances of the scanning tip, it is desirable to employ noble metals which exhibit resonances in the visible regime [30]. STM operation and Tip-Enhanced Raman Spectroscopy (TERS) was demonstrated with Au and Ag tips, obtained from specifically optimized electrochemical etching methods [83, 84]. In this work, PtIr(80:20), W and Au scanning tips are used in experiments, which were fabricated by following established procedures [85, 86].
Fig. 3.4(a) schematically depicts the electrochemical setup to etch sharp tips from polycrystalline wire. Mostly, a wire diameter of 125 μm is used for both Au and W tips. The wire is immersed in an electrolyte solution of potassium hydroxide (KOH) or concentrated hydrochloric acid (HCl) for W or Au, respectively. An applied voltage between the contacted wire and a Mo ring as counter electrode drives an electrochemical process that dissolves the immersed wire, while the meniscus that forms around the wire due to the electrolyte surface tension gradually tapers the tip towards the apex. Within ns after the lower wire part separates from the etched tip, the voltage is turned off to prevent further etching of the apex. The exact tip morphology further depends on electrolyte concentration, wire diameter, immersion depth and alignment and the applied voltage. Fig. 3.4(b) shows an SEM micrograph of a W tip, which was etched from a 125 μm wire in a 1.5-molar KOH solution at 9 V DC applied voltage and 2 mm immersion depth. The apex radius is ∼20 nm. Fig. 3.4(c) shows a micrograph of a Au tip, which was etched from a 125 μm wire in a 1:1 solution of 37% concentrated HCl and ethanol at an immersion depth of 2 mm. The applied voltage was dynamically adjusted, with regard to an empirically found optimum etch current of 6 mA to achieve as sharp tips as possible. The PtIr(80:20) tip was bought commercially from Omicron and the fabrication procedure is unknown.

3.4.2 Tip Engineering by Focused Ion Beam Bombardment

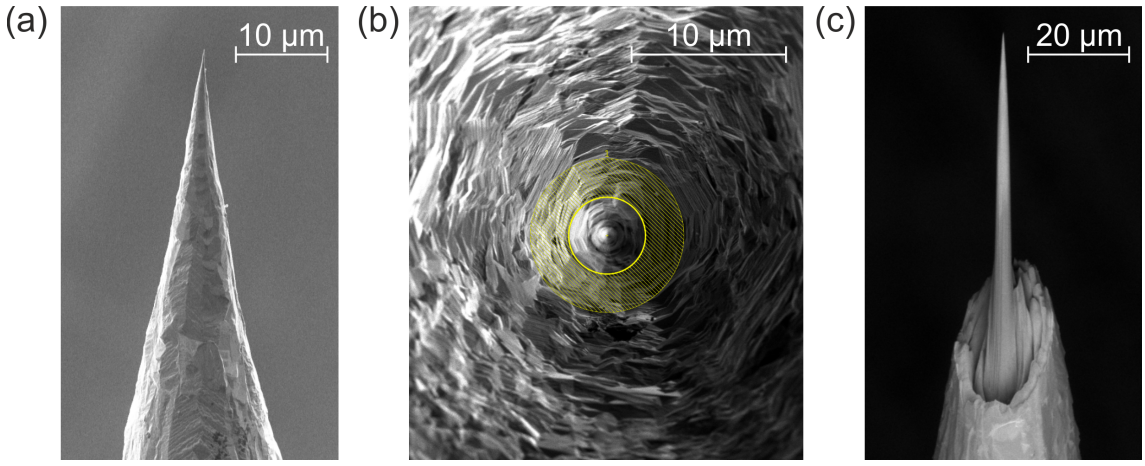

Figure 3.5: SEM micrographs of a Au scanning tip. (a) Side view of electrochemically etched tip, fabricated by following the described procedure. (b) Top view of the tip with the FIB exposed area indicated (yellow shaded). (c) Side view of FIB polished tip. The polished part is 50 μm long.

FIB milling is a technique which employs a focused beam of, in this case, gallium ions for directed material ablation with nanoscale precision. The system is incorporated in an SEM which allows both electron as well ion imaging. The combined FIB/SEM at the Fritz-Haber Institute for Inorganic Chemistry is the Helios NanoLab G3 UC from Thermo Fisher Scientific [87].
Fig. 3.5(a) shows an SEM micrograph of an electrochemically etched Au tip before FIB treatment. The tip is positioned to directly face the gallium ion source with minimal misalignment to manufacture a radially symmetric shape. Fig. 3.5(b) shows a micrograph of the tip facing the electron source before it is positioned towards the gallium source. The roughness is clearly visible on the tip shaft, which originates from differences in the etching rate, e.g. due to etch rate differences of different crystal faces. The yellow indicated area will be exposed to the ion beam, which yields a continuous ablation along the tip axis and minimum ion implantation into the remaining tip material, which may influence the plasmonic properties of the metal. Fig. 3.5(c) shows a micrograph of a FIB polished tip with a length of the polished part of 50 μm. The tip opening angle is usually below 5° at the shaft and increases at the apex, which is given by the fabrication procedure, while the tip apex diameter can be loosely controlled during the process and chosen minimal for our experiments. It ranges regularly below 20 nm. The polished length is only dependent on the sputtering time and may, in principle, be chosen arbitrarily. Structures in the tip shaft like grooves are achieved in a similar way by focusing the ion beam perpendicular to the tip axis.

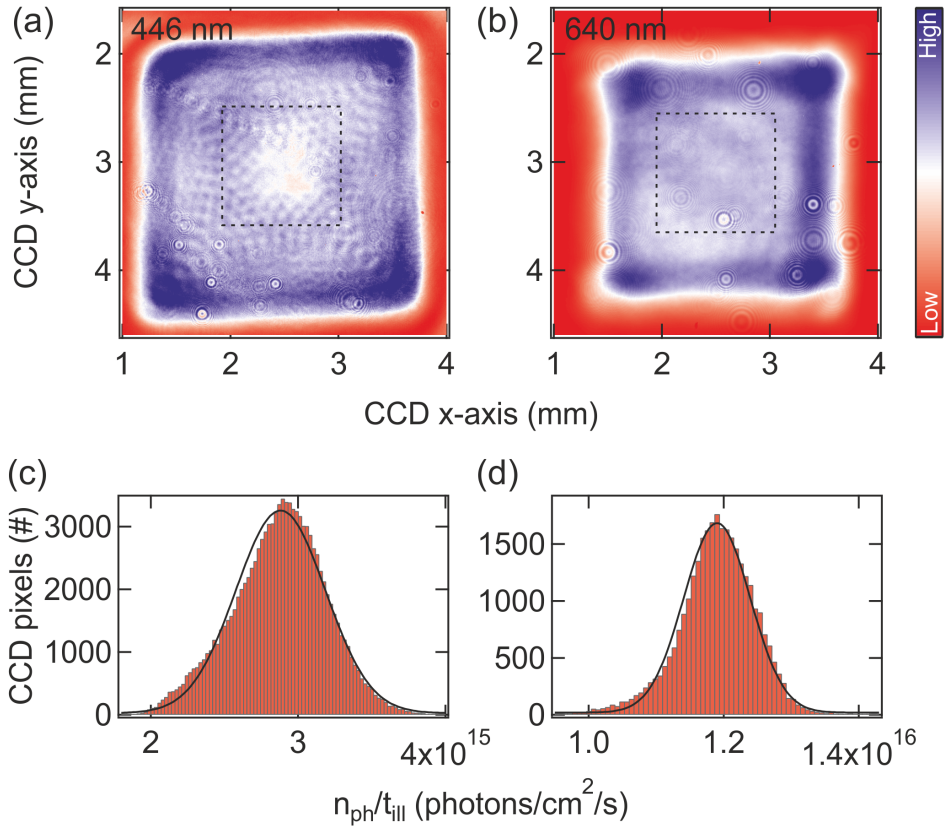

Figure 3.6: Top-hat shaped beam profile from an (a) 446 nm diode laser and (b) supercontinuum source at 640 nm. Dashed squares indicate a defined 1 mm^2 region of interest. (c),(d) Respective histogram of pixel intensity on the beam profiler as function of sample impinging photon flux. A Gaussian fit (black curve) yields the mean photon flux with standard deviation for 446 nm: $2.89(\pm 0.30)\times 10^{15}$ $cm^{-2}s^{-1}$ and 640 nm: $1.19(\pm 0.05)\times 10^{16}$ $cm^{-2}s^{-1}$.

3.5 Spectrally Tunable Optical Excitation in Combination with STM

In order to provide quantitative insight into STM probed photochemical reactions, precise control of the incident photon flux which impinges on the investigated sample is indispensable. As controlled positioning and alignment of an incident light source to the tip-sample junction is complicated, we have chosen a different approach.
Incident laser beams are shaped into a square top-hat, which redistributes the intensity from a Gaussian beam homogeneously across a broad spatial range, thus eliminating the prerequisite of precise junction alignment. The desired beam shape is achieved by using a Topag top-hat shaper with antireflective coating for visible and near-infrared (IR) laser beams (model GTH-3.6-1.75). Fig. 3.6(a) shows an exemplary beam profile from a 446 nm laser diode from Thorlabs, while Fig. 3.6(b) shows a profile from an NKT Photonics supercontinuum white light laser source at 640 nm [88]. At 446 nm, the shaped beam size is about 2.5 mm^2 while it is about 2 mm^2 at 640 nm. For evaluation of the incident photon flux, a spatial region of about 1 mm^2 in the beam center is selected (dashed square

in Fig. 3.6(a),(b)), which is easily aligned to the tip-sample junction, but also excludes the outer part of the beam that accumulates higher intensity due to slight misalignment of the incident beam to the top-hat shaper. Fig. 3.6(c) and (d) depict a histogram of intensity that impinges on each beam profiler pixel for 446 nm and 640 nm, respectively. The intensity is recalculated to the photon flux on the sample by taking into account the total emitted power into the SPM chamber and the experimental geometry:

$$\frac{n_{ph}(x,y)}{t_{ill}} = \frac{I(x,y)}{\sum_{x,y} I(x,y)} \frac{cos(65°)}{A_{pixel}} \frac{P_{inc}}{E_{ph}} T(CaF_2) \tag{3.8}$$

where $n_{ph}(x,y)/t_{ill}$ is the photon flux on the sample per beam profiler pixel in x- and y-direction and t_{ill} is the duration of exposure. $I(x,y)$ is the recorded intensity on each pixel and A_{pixel} its area. $T(CaF_2) \approx 0.9$ is the transmittance of the SPM chamber viewport window and $cos(65°)$ accounts for the unidirectional elongation of the beam, due to its incident angle, relative to the scanning tip axis (see Fig. 3.7(c)). E_{ph} is the spectrally dependent incident photon energy and P_{inc} the total measured power in front of the SPM chamber. From the intensity histogram, it is possible to derive a mean photon flux on the sample and its standard deviation by fitting the distribution to a Gaussian. For the exemplary profiles at 446 nm and 640 nm, the photon flux is determined as $2.89(\pm 0.30)\times 10^{15}$ cm^{-2}s^{-1} and $1.19(\pm 0.05)\times 10^{16}$ cm^{-2}s^{-1}. The incident photon flux is used to relate the measured photochemical activity to the incident intensity with an appropriate error, thereby a normalization is achieved when different laser sources are used.

Fig. 3.7(a) depicts a top-view of the laser table. For accessing a broad spectral range, different sources are employed. The supercontinuum laser source (super K) provides coherent quasi CW light in the entire range between 400-2400 nm (Rep. rate: 2-78 MHz), which is selectively filtered to pick out single laser lines with a spectral width of 6-10 nm, depending on the wavelength. With the current appliances, a spectral range of 480-1100 nm may be accessed. Through frequency doubling, the UV range 330-380 nm is further available. Light is coupled out to free space with a Gaussian profile from a non-polarizing fiber and subsequently polarized by a Glan-laser calcite polarizer. The arrangement of the beam expander is depicted in the grey shaded box in Fig. 3.7(a). Lens 1 (f=-50 mm) and 2 (f=175 mm) expand and collimate the Gaussian beam to a diameter of ∼3.6 mm, as the optimum input diameter of the top-hat shaper is 3.6(±0.15) mm. After the top-hat shaper, lens 3 (f=1000 mm) focuses the beam onto the sample or the beam profiler, which is positioned, so that the distance flip mirror - profiler is the same as flip mirror - sample. Therefore, the focus position at the beam profiler is considered approximately equal to the sample position. Frequency tripled and quadrupled CrysLas Nd:YAG lasers provide intense single-line UV light at 355 and 266 nm (Rep. rate: 1-10 kHz, Power: 40.3 mW and 7.3 mW, respectively), however, the latter does not overlap with the top-hat shaper working range. It is therefore strongly defocused in measurements to achieve a nearly homogenous intensity across a mm^2 spatial range. Thorlabs diode lasers with single-line wavelengths of 405, 446, 532 and 780 nm (Power: ∼4 mW) were further employed. The emitted beam profile from Nd:YAG and diode lasers, as opposed to the supercontinuum source, shows a strong astigmatism which is accounted for by a modified beam path which spatially filters the incoming beam (Fig. 3.7(b)). Lens 1 (f=100-175 mm, depending on source) focuses on a Mo pinhole (diameter: 25 μm), while lens 2 (f=75 mm) recollimates the filtered beam at the right distance from the pinhole to achieve a beam diameter of ∼3.6 mm. At a 65° angle, the shaped beam is directed towards the CaF_2 viewport of the SPM main chamber, which provides high constant transmittance from UV to near-IR

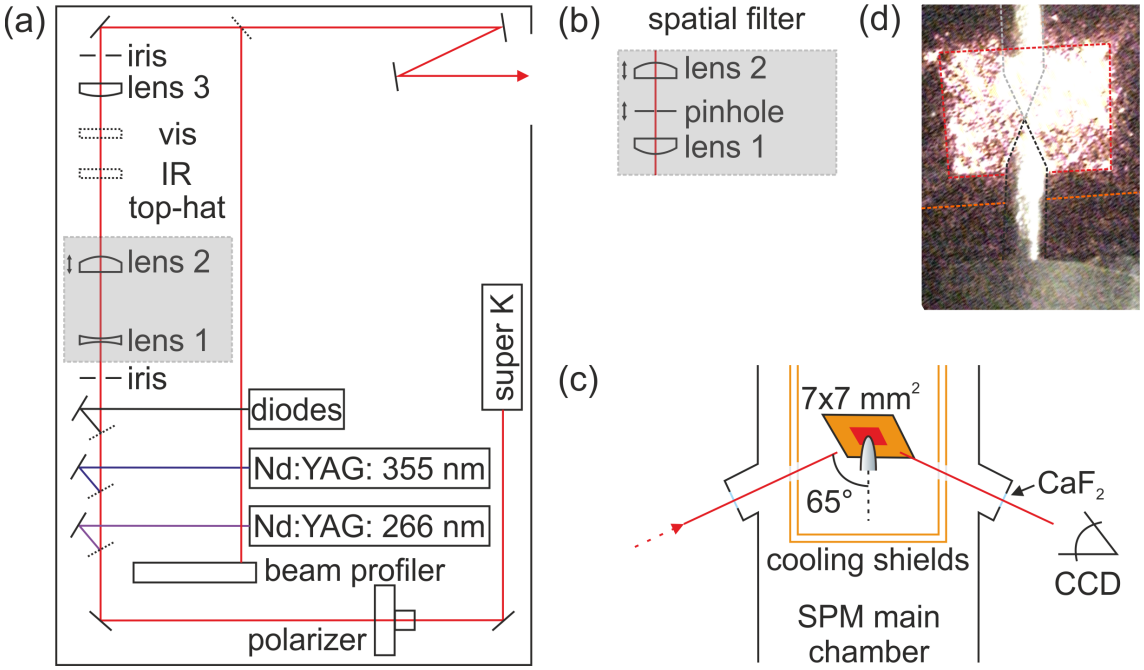

Figure 3.7: (a) Schematic top-view of the optical table with various light sources. (Flip) mirrors are represented by solid (dashed) lines that represent the beam (red). (b) Spatial filter for diode and Nd:YAG lasers. (c) Schematic side-view of a cross section of the SPM chamber. The incident top-hat beam impinges at the tip-sample junction and is reflected towards a camera outside the chamber. (d) Snapshot of the junction, illuminated with a 640 nm top-hat beam (red dashed). The tip (black dashed), its reflection on the sample (grey dashed) and partially the sample edge (orange dashed) are visible.

(Fig. 3.7(c)). IR windows in the cooling shields around the SPM head provide optical access to the tip-sample junction. The beam is visually aligned to the junction by observing its reflectance in a camera. Fig. 3.7(d) shows a snapshot of the junction, illuminated by a 640 nm top-hat beam (red dashed). The image of the tip (black dashed) is reflected on the sample (gray dashed), while the sample edge (orange dashed) is only partially visible. Visual alignment with precision of a few hundered micrometer is sufficient to estimate the incident photon flux, due to the homogenous intensity distribution.

4 Photoinduced Porphycene Tautomerization on Cu(111)

Interactions of molecules with their environment leads to complex functionality in nature, based on molecular switching to alter physical, chemical and biological properties. Important examples are signal conversion in vision or the bacterial energy production [89, 90]. In order to emulate and design this functionality to a specific purpose, the integration of molecular switches into controllable systems is indispensable. By anchoring molecules to surfaces, one can achieve highly ordered systems that are addressable by external stimuli like light, heat or electrical current. However, photochemically induced molecular bi-stability is specifically advantageous as it is a non-invasive process with high spatio-temporal precision [91, 92]. Especially in information technology, the quest of designing next-generation devices that operate faster and more efficiently at massively reduced production cost and functional unit size down to individual molecules has drawn increasing interest towards responsive molecular systems and established the field of molecular electronics, where switches may perform logic and memory operations [93]. Furthermore, photonic elements that carry information in nano-electronic circuits at THz frequencies may be readily integrable in devices that consist of coupled photoresponsive molecular units, thus reducing operation time and length scales to the very limit [94]. Despite the promising capabilities of all-optical operation, no working device has been demonstrated yet. Surface science techniques are capable to unravel the electronic structure as well as the interplay of molecule-substrate and molecule-molecule interaction in well-defined geometries, even at operation conditions by applying external stimuli, which provides the necessary basis for functional design and STM has been proven a useful tool to access elementary processes in single molecules under photoexcitation [95–101]. Nevertheless, most studies so far have focused on photoisomerization reactions that include drastic confirmational changes of the molecule. One of the major challenges towards device integration is, however, the coupling of molecular units while maintaining their individual functionality during operation [93]. The rapid and controllable conversion of tautomers between physically distinguishable forms has gained increasing attention as this class of molecules provides the ability to perform operations within an extremely small space ($\sim$1 nm) at a high efficiency, while the skeletal structure is maintained [102–105]. Albeit the demonstration of the working principle via electronic and thermal excitation, there has been no study yet focusing on the operation of a photoresponsive tautomeric switch.

Here, we present the photoexcited tautomerization of individual porphycene molecules on a Cu(111) surface which is investigated by low-temperature STM and wavelength tunable laser excitation. The thermodynamically stable *trans* form is found to unidirectionally convert to the metastable *cis* tautomer. Photogenerated charge carriers from the Cu substrate drive the reaction via attachment to the molecule and subsequent vibration excitation which initiates the reaction by intermode coupling to the tautomerization coordinate. The reaction mechanism is elucidated by combining photoexcitation and inelastic tunneling electron excitation of isotope substituted molecules. It is further demonstrated that the photoreaction is hindered at higher molecular surface coverage.

4.1 Introduction to Photoinduced Molecular Switching Studied by STM

The following section provides an overview of previous work on bi-stable conversion at the single-molecule level by external stimuli and specifically optical excitation. Focus of this review is laid on STM studies, which provide fundamental insight into molecular properties and operation performance at fundamental spatial resolution.

4.1.1 Single-Molecule Switching

Interconversion of molecules between bi- or even multi-stable states can be achieved with various external stimuli, which may be readily applied in an STM setup while different molecular states can be probed with atomic-scale resolution. The stimuli that were demonstrated to initiate molecular switching include light, electric field, temperature, current or even chemical stimuli. External excitations are usually not selective at the single-molecule level but applied to the molecular ensemble and probed by comparing initial and final states of the molecule, discriminated by their appearance in STM imaging, except for direct injection of the tunneling current. Depending on the individual molecule, the switched property includes molecular confirmation, dipole orientation, spin or charge state and chemical bonding [106–116]. Illustrative fundamental examples of this wide research field are selected here to demonstrate the capabilities of molecular functionality on solid surfaces.

A strong electric field may be generated by withdrawing the STM tip from the surface and applying a bias between tip and sample, which may distort the reaction potential landscape via dipole coupling up to a point where the reaction barrier is lowered so much that the stability between states is inversed. This mechanism was demonstrated to drive the reversible *trans* $\leftrightarrow$ *cis* conversion of Tetra-*tert*-butyl (TTB)-azobenzene on a Au(111) surface (see Fig. 4.1) as well as the transition of Zn(II) Etioporphyrin I on NiAL(110) from a saddle to clover shaped conformation [106, 117]. The STM tip is retracted during the experiment from the surface beyond the tunneling regime to discriminate the mechanism from direct charge carrier injection and a linear reaction threshold voltage dependence is observed with distance.

Thermal excitation of molecular switching may be achieved for low reaction barriers where the process is mediated by hopping diffusion and may only drive reversible conversion unless one state is energetically much more favorable so that the system is converted to its energetic ground state, as exemplary depicted for TTB-azobenzene in Fig. 4.1, where the molecule recovers to the thermodynamically stable *trans* state upon heating. TTB-azobenzene is a conformational switch that can be operated by various external stimuli to drive the same reaction. It was further observed that thermal excitation is responsible for interconversion between the achiral *meso*-form and chiral enantiomers of 1,4-bis[(5-*tert*-butyl-3-formyl-4-hydroxyphenyl)ethynyl]benzene on the Au(111)-(22$\times\sqrt{3}$) surface [118].

Electron induced reactions are excited in STM by charge carrier injection from a localized tunneling current which induces chemistry via inelastic scattering or dissociative electron attachment. Several studies have applied this concept to study switching both locally and non-locally on metal surfaces, where injected carriers can travel along the surface state [108, 113, 119–124].

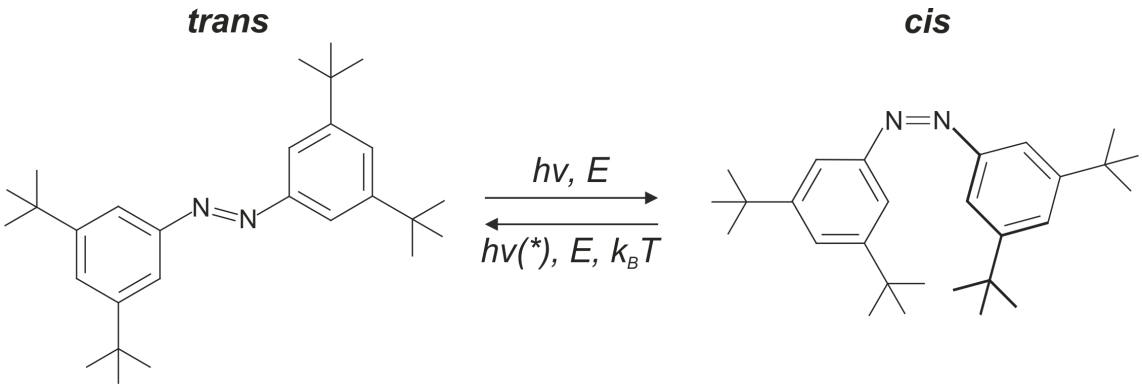

Figure 4.1: TTB-azobenzene isomerization between the thermodynamically stable *trans* and the metastable *cis* state. The reaction is selectively initiated by various external stimuli, i.e. light at different energies ($h\nu$, $h\nu^*$) and heat (k_BT) [95, 128]. On a metal surface, electric field (E) and light induces reversible isomerization [117].

Organometallic complexes consist of a π-conjugated systems and a metal ion center which acts as a local reactive site for chemical stimuli. Various molecular properties may be altered upon gas molecule adsorption. This concept was applied to control the molecular spin of manganese phtalocyanine on Au(111) upon CO or H adsorption [125, 126].

4.1.2 Photoresponsive Molecular Switches

Studies of photoactive molecular bi-stable conversion, investigated with STM, are strongly focused on conformational isomerism of azobenzene derivatives on metallic and insulating surfaces. Photochromism in azobenzene compounds is an established and well investigated phenomenon which has more recently gained increasing interest in the field of photomechanical energy conversion [127–129]. Upon UV light absorption in gas or liquid phase, the *trans* isomer converts to the *cis* form, while the reverse reaction is induced by visible excitation ($h\nu$ and $h\nu'$ in Fig. 4.1). Anchoring azobenzene to surfaces can strongly modify the molecular geometry and electronic structure due to molecule-substrate interaction, thereby quenching the isomerization process. To circumvent this effect and reduce the coupling, ligand groups were attached to the molecule which lift it from the surface and reduce the molecule-substrate coupling. It was successfully demonstrated that switching functionality is preserved in this way on a Au(111) surface, however, the photoisomerization was reversibly induced both by UV and visible light, in dramatic departure from gas and liquid phase behavior [95, 97, 98]. This is attributed to the still strong electronic and geometric modification, affecting both the behavior as well as the photoreaction cross section which decreases by about three orders of magnitude upon adsorption ($\sigma \approx 10^{-23} - 10^{-22}$) [97, 130]. The cross section could be increased by one order of magnitude by using a different derivative (4-Anilino-4'-nitroazobenzene) on Cu(111), but the desired gas phase functionality and efficiency remains unachieved [99]. Further decoupling of the molecule from the substrate is achieved by growing a thin insulating layer of NaCl between Ag(111) and deposited azobenzene derivative (4,4'-dihydroxyazobenzene) [100]. Even though the molecular electronic structure is less perturbed, the interaction with the polar surface led to a blockage of the reverse *cis* $\rightarrow$ *trans* pathway, which was rationalized by electrostatic

interaction.
Similar studies have been carried out on nitro-spyropyran which may undergo a ring-opening-ring-closing photoreaction and was demonstrated to reversibly switch under blue light excitation on Au(111) and Bi(110) at dramatically reduced cross sections, compared to solution ($\sigma \approx 10^{-22}$) [101, 131].
Albeit the extensive effort that is directed towards the transfer of photoresponsive molecular functionality to metal surfaces, the realization of a selectively addressable and efficient molecular photoswitch is yet to be realized. The exploration of conceptually different chemical mechanisms could hold the potential to overcome the inherent difficulties of conformational isomerization on metal surfaces.

4.2 Introduction to Tautomerization

This section provides an overview of the abundant tautomeric reactions that govern important processes in nature and introduces the special case of prototropic tautomerization. Recent studies that show the feasibility to implement tautomeric switches for applications in nanotechnology are further presented.

4.2.1 Prototropic Tautomerization in Chemistry and Biology

Tautomerization is a special case of structural isomerism and defined as the process of intramolecular atom or functional group migration. It leads to molecular structure change and electron density redistribution which is accompanied by a change of chemical and physical properties. Since structural isomerism often includes the rearrangement or rotation of whole functional groups, it is difficult to induce and can be sterically hindered, whereas tautomerization is rapid and sensitive to suddle environmental changes which influence the dynamic equilibrium between tautomeric forms. The most common subclass of tautomeric reactions and focus in this work is prototropic tautomerization which describes the intramolecular migration of a hydrogen atom (proton). Albeit the limited number of molecules in which it can occur, prototropic tautomerization represents a fundamentally important process in organic chemistry and biology as it is directly related to thermo- and photochromism [132, 133], enzymatic reactions [134] and base-pairing mutation [135]. It is therefore of vital importance for understanding biological systems and chemical processes therein such as mutagenic transformations in DNA replication which is determined by the ability of different tautomers of DNA bases to bind to specific acceptors/receptors [136–138]. One illustrative example for tautomerization induced thermo- and photochromism is depicted in Fig. 4.2 where the uncolored enol form of N-salicylidene aniline in (a) converts into the yellow *cis*-keto in (b) upon heating while it can convert to the red *trans*-keto form in (c) via UV photoexcitation [139]. The intramolecular migration of a single H atom is here accompanied by electron redistribution in the aromatic system and therefore changes the physical properties of the molecule as manifested in a color change which may be exploited in view of potential applications in sensor or display technology [140].

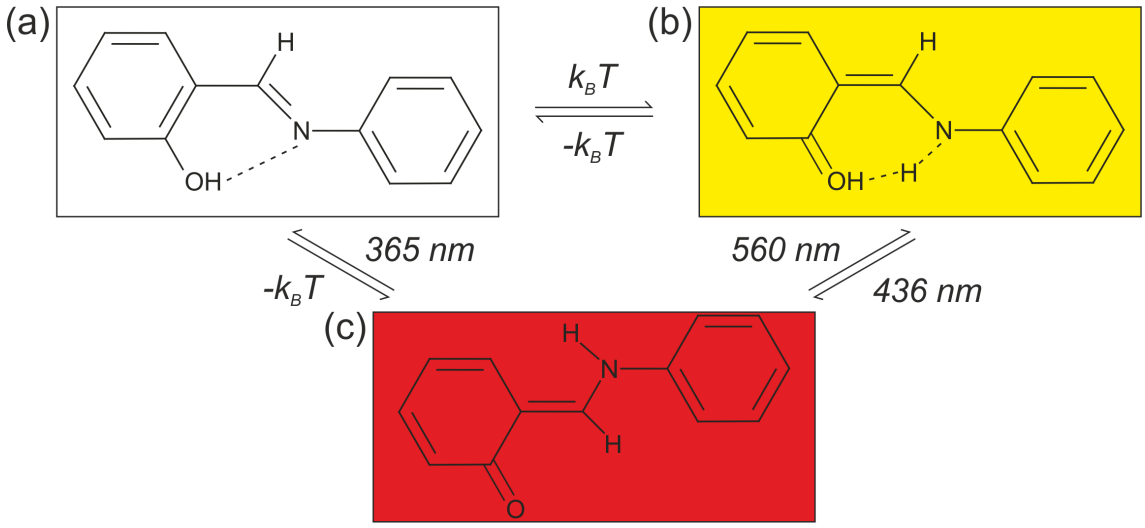

Figure 4.2: Thermo- and photochromism pathways of N-salicydilene aniline. (a) Uncolored enol form converts to the (b) Yellow *cis*-keto form via thermal excitation or the (c) red metastable *trans*-keto form. Photoexcitation converts the enol and *cis*-keto form to the red metastable *trans*-keto form (bottom). (Adapted figure with permission from Robert *et al.*, Chrystal Engineering Communications **2012**, 14, 4396-4406 [139]. Copyright 2012 by the Royal Society of Chemistry. Adapted with permission of the author.)

4.2.2 Tautomerization on Surfaces

Recently, the rapid and controllable conversion of tautomers between physically distinguishable forms has gained increasing attention in nanoscale science as it seems promising to implement tautomers as functional building blocks for future molecular electronic devices, where all device functionality stems from single interacting molecules [141–143]. Tautomers resemble here the behavior of molecular switches which form a functional unit in molecular electronics analogous to logic and memory components like transistors in modern solid state electronics as demonstrated in STM studies. The reversible interconversion between tautomeric forms is induced through vibrational excitation by inelastic electron tunneling, as depicted in Fig. 4.3(a) [102, 103, 105, 144]. The pioneering works, reproduced in Fig. 4.3(b) and (c), demonstrate the working principle based on STM probed conductance switching upon tautomerization of individual free-base naphtalocyanine and porphyrin derivative molecules. Upon adsorption of the molecules and cooling to cryogenic temperatures, one tautomeric form is stabilized on the surface and then reversibly interconverted between two stable conductance states by electron injection above the LUMO of the molecule as observed in the current trace in Fig. 4.3(b). Here, the two intracavity H atoms within the naphtalocyanine molecule switch between two bonding sites which corresponds to a *trans*↔*trans* conversion. Analogous to this experiment, tautomerization in free-base tetraphenyl-porphyrin was demonstrated on a Ag(111) surface (Fig. 4.3(c)). These classes of molecules provide the ability to perform logic and memory operations within an extremely small space (∼1 nm) without undergoing drastic confirmational changes like other isomerization based molecular switches, e.g. azobenzene derivatives [117, 119, 121]. They are therefore readily integrable into molecular electronic circuits where functionality and coupling to other units may be preserved during operation. Moreover, tautomeric single

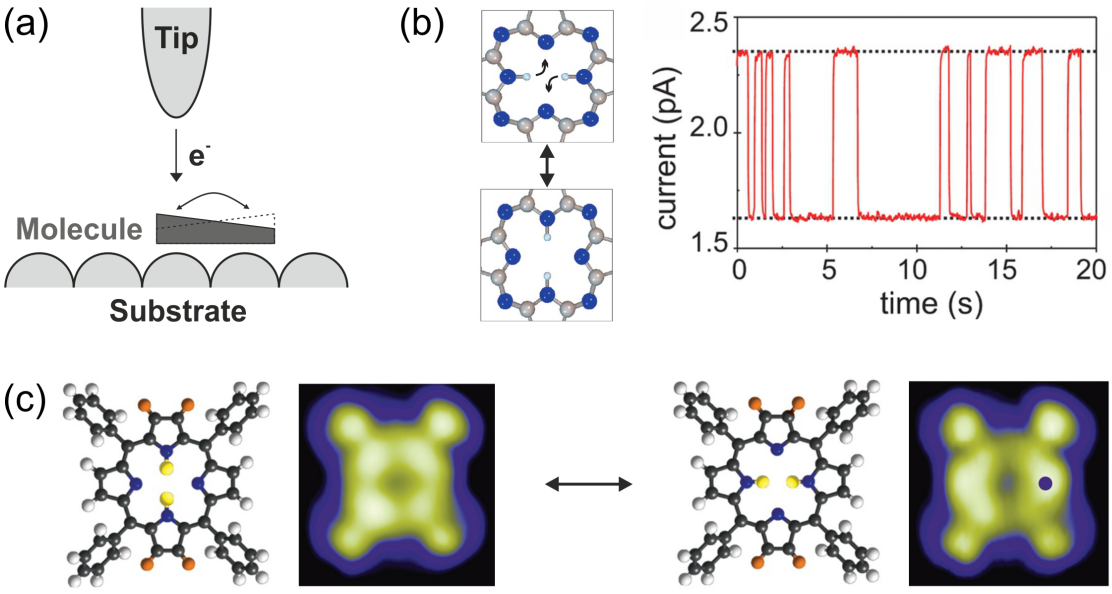

Figure 4.3: (a) Measurement schematic of STM induced switching. The molecular reaction is induced by energetic tunneling electrons and detected in the STM current trace. (b) Naphtalocyanine on a NaCl bilayer on Cu(111). The structure model shows the inner cavity H atom tautomerization upon electron injection. The recorded current trace exhibits two levels that correspond to the tautomeric forms. (c) Tetraphenyl-porphyrin (TPP) on Ag(111). Structure model and STM images show two equivalent states. The tautomerization is induced and detected as in (b). ((b) is adapted by permission from Liljeroth *et al.*, Science **2007**, 317(5842), 1203-1206 [102], copyright 2007, (c) is adapted by permission from Auwärter *et al.*, Nature Nanotechnology **2011**, 7, 41-46 [103], copyright 2011)

molecule switches can potentially not only replace but extend the functionality that is known today from solid state devices since not only two-state but multi-state switching between tautomeric forms has been demonstrated [103, 145].

4.3 Porphycene

Porphycene (Fig. 4.4(a)) is a structural isomer of porphine (free-base porphyrin) (Fig. 4.4(c)) with comparable chemical properties [146]. However, the inner cavity of porphycene has a rectangular shape (Fig. 4.4(b)) in contrast to the square shaped porphine inner cavity (Fig. 4.4(d)). The rectangular geometry in porphycene leads to a more favorable arrangement of the N-H$\cdots$N configuration to form intramolecular H bonds in the cavity as compared to porphine [147]. The distance between neighboring N atoms is reduced from 2.89 Å to 2.63 Å and the N-H$\cdots$N bond angle is increased from 115° to 152° [146, 148, 149]. Formation of H bonds in the cavity further yields a significant modification of the tautomerization potential energy surface which is manifested in a lower reaction barrier. The transition between the doubly degenerate *trans* states, where the H atoms are located at opposite N atoms (Fig. 4.4(e)) was observed in gas phase at room temperature at a

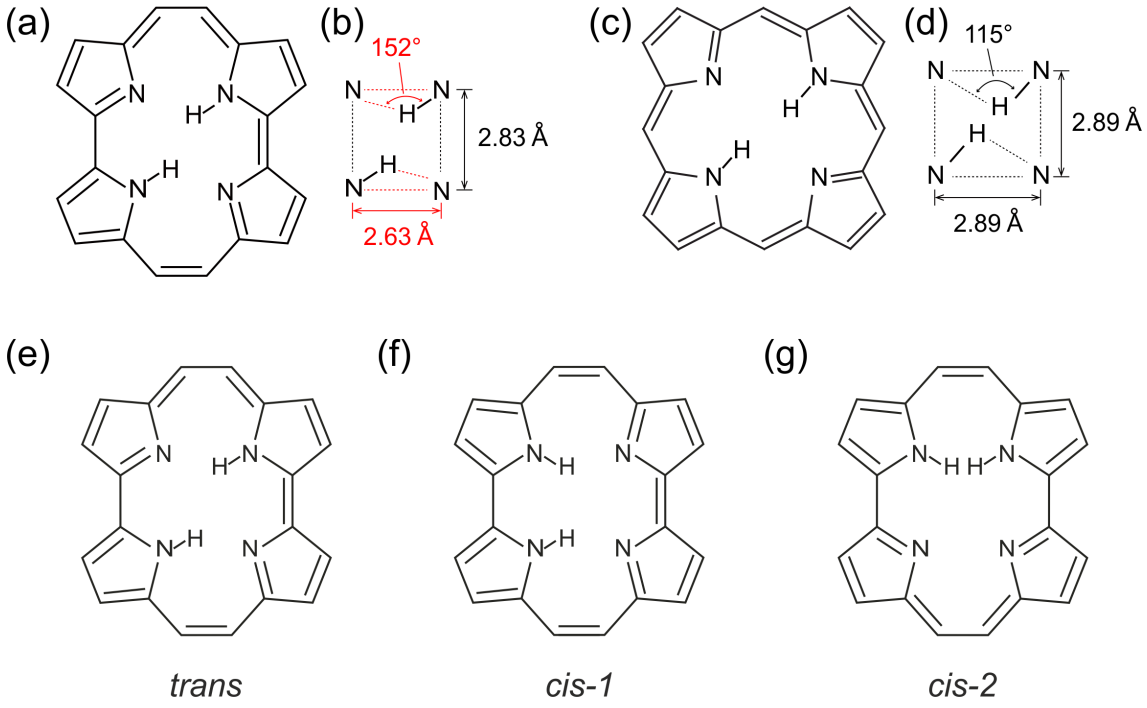

Figure 4.4: Porphycene and porphine *trans* state structure model (a),(c) and gas phase inner cavity geometry (b),(d) respectively. (e) *trans*, (f) *cis-1*, (g) *cis-2* porphycene tautomer.

rate of 2×10^4 s^{-1} and 5.8×10^{11} s^{-1} for porphine and porphycene, respectively, hence demonstrating the influence of H bond formation on the tautomerization dynamics [150, 151]. Besides the *trans* state, porphycene can exist in two other doubly degenerate tautomeric forms, the *cis-1* (Fig. 4.4(f)) and *cis-2* (Fig. 4.4(g)) state, where the H atoms are located at neighboring N atoms. Porphycene tautomerization has been extensively studied in gas phase, solution and polymer films [147, 148, 152, 153]. It was demonstrated that porphycene tautomerization is mediated by proton tunneling and coherent delocalization in the cavity which results in state splitting both in the electronic ground and first excited state [151, 154, 155]. The investigation of porphycene derivatives has revealed the crucial role of the H bond strength for the tautomerization dynamics which is readily understood by the exponential dependence of the tunneling rate on barrier width, modulated by the N atom distance in the cavity . Furthermore, population of low-frequency vibration modes of the molecule may either promote or hinder the reaction, since the tautomerization is described by a multi-dimensional model where vibrations may couple to the reaction coordinate [156]. However, upon condenstation on a substrate, the molecule potential surface may be drastically influenced due to molecule-substrate interaction and the functionality needs to be evaluated directly in the condensed phase at the single-molecule level. Tautomers are highly sensitive to subtle changes in environment which can determine the thermodynamic stability of one tautomeric state over another and the potential surface for interconversion between stable and metastable forms. Upon adsorption on a substrate, the molecule-substrate interaction determines the relative potential energy of the tautomers. During the course of this work, porphycene tautomerization was studied on the (111) and (110) surface of copper. Fig. 4.5 shows the total calculated energy of the tautomers in gas phase and on the copper surfaces. The *trans* state is predicted to be more stable in gas

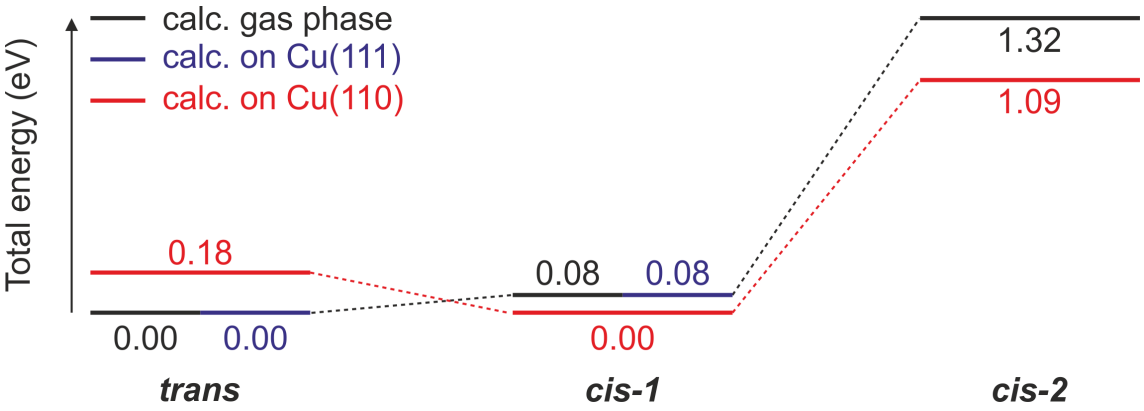

Figure 4.5: Calculated relative total energies for (a) *trans* (b) *cis-1* and (c) *cis-2* configuration in gas phase [157, 158], on Cu(111) [159] and on Cu(110) [158].

phase and on Cu(111) with a slightly lower energy than the *cis-1* state which is stable on the Cu(110) surface. The *cis-2* state is considered unstable in all configurations, due to steric hindrance, which is why the *cis-1* state will be referred to as the *cis* state from here on.

Porphycene Tautomerization on Cu(111)

Porphycene adsorbs on the Cu(111) surface as isolated molecules in the *trans* state as determined from the appearance in STM images (Fig. 4.6(a)). Fig. 4.6(b) shows a schematic of the molecule structure on the surface [159–161]. Two point symmetric protrusions are observed in the image in agreement with the *trans* configuration. The molecule adsorbs around a hollow site and appears in six different orientations, resulting from the three high symmetry axes of the (111) surface and two mirror symmetric *trans* tautomers (Fig. 4.6(e)). There is no island formation which may be explained by strong bonding between the porphycene N atoms and the substrate Cu atoms. Upon adsorption, all molecules are found in the *trans* state, thus confirming its thermodynamic stability. However, by injecting energetic tunneling electrons from the STM tip into the molecule, the unidirectional conversion to the metastable *cis* state is induced, which may also appear in six different adsorption configurations (Fig. 4.6(c)). The asymmetric appearance in the STM image with a single protrusion and axis symmetry infers the conversion by comparison with the calculated *cis* structure (Fig. 4.6(d)). The *trans* molecules in (Fig. 4.6(e)) can be individually converted to the *cis* tautomer by applying a short voltage pulse at the indicated tip position, while the *cis* tautomers only interconvert between the mirror symmetric *cis* states (Fig. 4.6(g)-(h)). Due to the symmetry mismatch between molecule and substrate, the molecule laterally moves by ~ 0.14 nm ($a_0/2\sqrt{2}$) along the high symmetry axis during *cis* $\rightarrow$ *cis* conversion (a_0: Cu lattice constant [162]). From STM studies it was revealed that porphycene tautomerization is induced both via inelastic tunneling electrons and thermal excitation. Fig. 4.7(a) shows the bias voltage dependent tautomerization yield (observed reactions per electron) for the *trans* $\rightarrow$ *cis* and *cis* $\leftrightarrow$ *cis* reaction. The reaction yield exhibits a bias polarity independent onset threshold at about ± 150 mV for both reactions, which indicates that the reaction is induced via excitation of molecule vibrations by inelastic

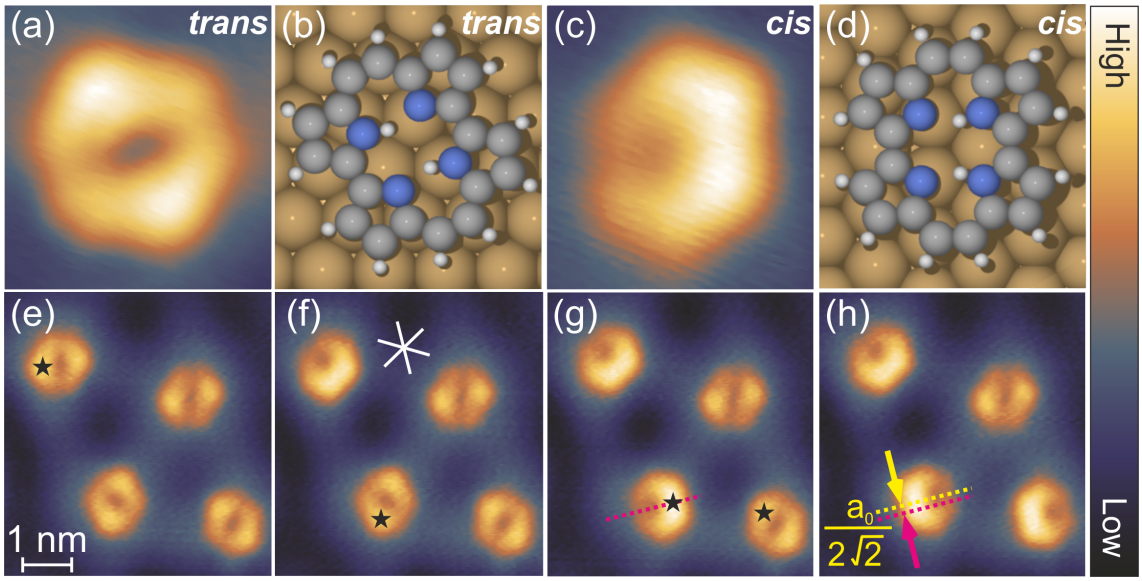

Figure 4.6: STM images and calculated adsorption geometry of a porphycene molecule adsorbed on Cu(111) in the (a),(b) *trans* state and (c),(d) *cis* state. (e) Porphycene molecules after adsorption in the thermodynamically stable *trans* state. Upon energetic electron injection from the STM tip (black star, V_s = -280 mV, I_t = 100 pA, δt = 100 ms), the molecule converts to the metastable *cis* state (f) and aligns along one of the substrate high symmetry axes, indicated by white lines. (g) Conversion of a second molecule to the *cis* state but oriented along a different high symmetry axis. (h) *cis* → *cis* conversion of the same molecule to the mirror symmetric *cis* state. The conversion involves the movement of the molecule along the high symmetry axis by ∼ 0.14 nm ($a_0/2\sqrt{2}$) (Image parameters: V_s = 100 mV, I_t = 100 pA). ((b),(d) is adapted by permission from Novko *et al.*, J. Phys. Chem., 145, 244701, 2016 [159]. Copyright 2016 by the American Institute of Physics. Adapted with permission of the author. (a),(c),(e)-(h) is reproduced by permission from Ladenthin *et al.*, ACS Nano **2015**, 9(7), 7287-7295 [161], copyright 2015)

tunneling electrons. Resonant electron tunneling to a well defined HOMO or LUMO state can be excluded due to the small gap between the reaction thresholds in comparison with the gas phase calculated HOMO-LUMO gap of 2.2 eV [163]. However, a clear signature of the electronic structure of porphycene on Cu(111) has not been observed in experiments with Scanning Tunneling Spectroscopy (STS) and Angle Resolved Photoemission Spectroscopy (ARPES). This may be attributed to a strong hybridization of molecular orbitals with the surface electronic system through the interaction of imine N atoms in the molecular cavity with surface Cu atoms as suggested by calculations [159]. It was found susequent to the cited study that the calculated attractive forces between molecule and surface were initially overestimated which had to be revised, thus questioning the obtained results [160]. Furthermore, it should be noted that the choice of employed functional crucially influences the obtained molecular electronic structure in Density Functional Theory (DFT) calculations and it remains challenging to address this problem theoretically.
Fig. 4.7(b) shows the temperature dependent tautomerization rate in an Arrhenius plot of $R \propto exp(-E_a/k_BT)$, where E_a is the reaction activation energy, k_B is the Boltzmann

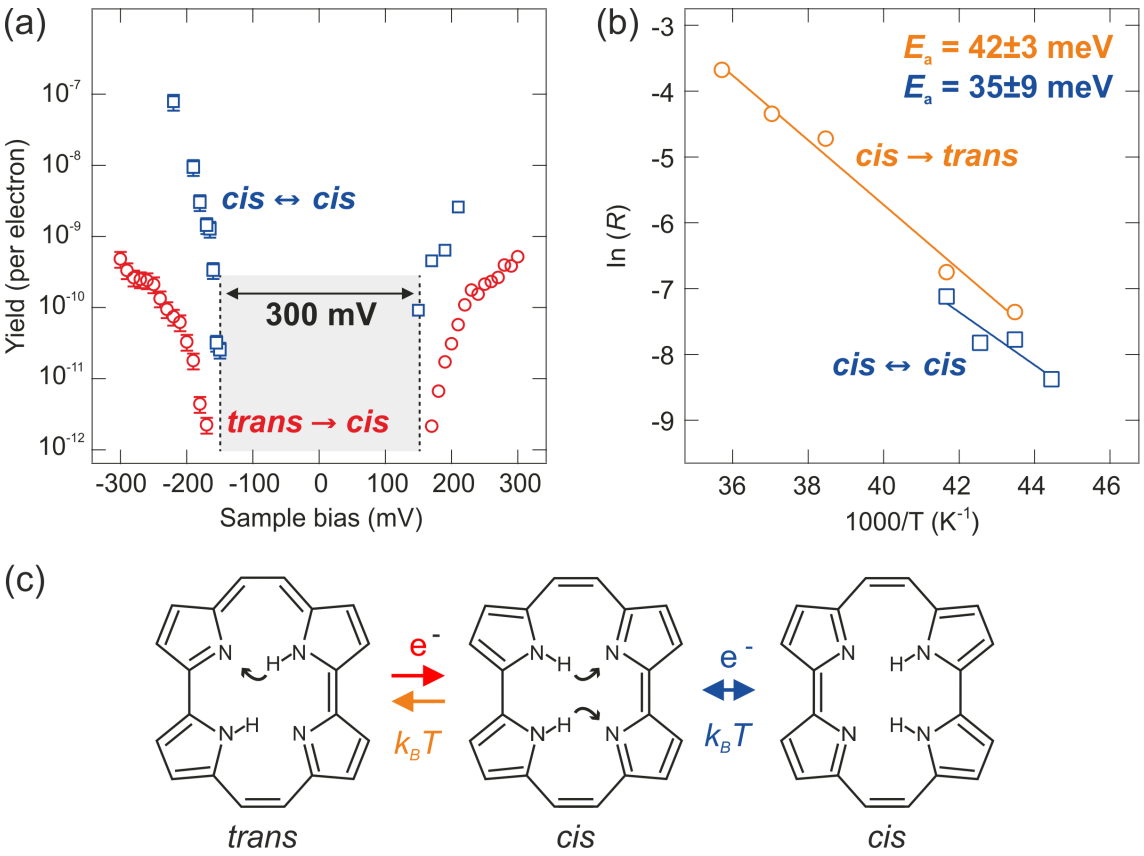

Figure 4.7: (a) STM bias dependence of the tautomerization yield for the *trans* → *cis* (red circles) and *cis* ↔ *cis* (blue squares) reaction. The polarization independent threshold voltage is determined as about ±160 mV for the *trans* → *cis* and ±150 mV for the *cis* ↔ *cis* reaction. (b) Arrhenius plot of the thermally induced tautomerization rate R, measured at V_s= 50 mV, I_t= 50 pA, far below the in (a) indicated threshold. Thermal excitation interconverts the molecules between the energetically degenerate *cis* states and from the metastable *cis* to the thermodynamically stable *trans* state. The activation energies are determined as E_a = 42(±3) meV and E_a = 35(±9) meV respectively. (c) Schematic depiction of the interconversion between the porphycene tautomers on Cu(111). The selective unidirectional *trans* → *cis* conversion is induced via energetic tunneling electrons (e^-) and can be reversed via thermal excitation (k_BT). The reversible *cis* ↔ *cis* conversion is induced by both stimuli. ((a),(b) is adapted by permission from Ladenthin *et al.*, ACS Nano **2015**, 9(7), 7287-7295 [161], copyright 2015)

constant and T is the temperature. During the experiment, the applied voltage was kept below the threshold for electron induced tautomerization to exclusively access the thermal reaction channel. The directionality of the unidirectional *trans* → *cis* is reversed upon thermal excitation with regard to electron induced tautomerization. The activation energies for the *cis* → *trans* and *cis* ↔ *cis* reaction are determined as E_a = 42(±3) meV and E_a = 35(±9) meV, respectively. The conversion between observed porphycene tautomers on Cu(111) by thermal and energetic tunneling electron excitation is summarized in Fig. 4.7(c). It is revealed that molecule vibration excitation via electron attachment yields

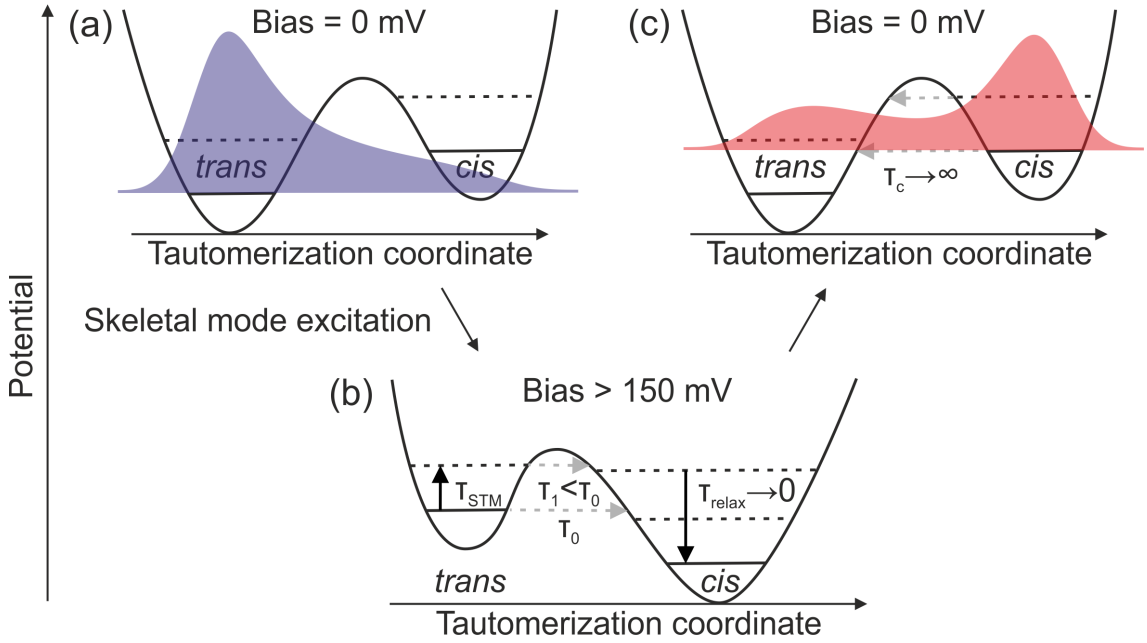

Figure 4.8: Schematic representation of the tunneling electron induced selective *trans* → *cis* conversion. (a) Initial potential energy surface along the tautomerization coordinate at zero bias with corresponding zero-point energies (solid lines), excited vibrational states (dashed lines) and the vibrational ground state nuclear probability density of the H atoms (blue shaded area). (b) Distorted potential due to quasi-thermal excitation of skeletal vibrations by non-adiabatic coupling to the metal electrons above 150 mV applied bias. τ_{STM} is the inverse excitation rate from ground to first excited vibrational state by electron tunneling from the STM tip. τ_0, τ_1 are the *trans* → *cis* tunneling times in the ground and first excited vibrational state. The molecule relaxes almost instantaniously to the ground state in the *cis* configuration with time τ_{relax}. (c) After conversion, the molecule remains in the *cis* configuration at zero bias, as manifested in the nuclear probability density (red shaded area). The tunneling time τ_c for *cis* → *trans* conversion becomes infinite. (Adapted by permission from Novko *et al.*, Journal of Physical Chemistry **2017**, 8(5), 1053-1059 [164], copyright 2017)

a unidirectional conversion from the thermodynamically stable *trans* to the metastable *cis* form, while this process is reversed by thermal excitation. The interconversion between mirror symmetric *cis* tautomers is induced by both stimuli. Since the time resolution in STM is limited to μs, the missing observation of *trans* → *cis* tautomerization via thermal excitation is rationalized by the rapid back-conversion, which lowers the lifetime of the *cis* state below the detection limit. The mechanism of selective electron induced *trans* → *cis* tautomerization was examined theoretically using DFT calculations by taking into account non-adiabatic coupling between molecular vibrations and electron-hole pairs in the substrate [164]. Since the exact molecular structure on the surface is still ambiguous, mechanistic insight into porphycene tautomerization can only remain qualitative at this point. Fig. 4.8(a) shows a schematic representation of the potential energy surface along the *trans* → *cis* reaction coordinate for a single molecule which is found in the *trans* configuration after deposition on the surface. STM electron tunneling indirectly distorts the potential non-uniformly along the reaction path via intermode coupling due to non-adiabatic cou-

pling between hot surface electrons and molecular vibrations (Fig. 4.8(b)). In the voltage range below 350 mV, only skeletal vibrations are accessible as the H-H stretch mode at about 350 meV is inaccessible. The stability inversion between the *trans* and *cis* form is rationalized by stronger bond formation between the *cis* tautomer with surface Cu atoms. In the *trans* configuration, porphycene is planar, at about 3.5 Å above the surface while the *cis* tautomer is buckled at about 2.5 Å above the surface. Therefore, electron mediated vibrational excitation is dissipated faster to substrate electrons and the excitation rate decreases while the potential remains relatively undistorted. Skeletal mode lifetimes are calculated to decrease significantly along the reaction path (*trans* : 5-10 ps and *cis* : 2-5 ps). Below the experimentally observed threshold voltage of 150 mV for *trans* → *cis* tautomerization, the skeletal vibrations may not inverse the stability and the molecule remains in the *trans* state. Above the threshold, resonant tunneling from the ground state or the first vibrationally excited state shifts the probability density between the two tautomers to the *cis* state due to fast relaxation of the vibrational excitation. After recovery of the initial conditions at zero bias, the molecule is trapped in the local potential minimum of the metastable *cis* state, which is reflected in the nuclear probability density which has shifted after excitation. The reverse reaction rate due to thermal fluctuations at 5 K is negligible and can only be triggered at higher temperatures where it is mediated by hopping diffusion. While porphycene tautomerization in the gas phase is mediated by proton tunneling and coherent delocalization in the cavity, on Cu(111) it is driven by molecule vibration excitation which modifies the tautomerization potential surface and transfers energy via intermode coupling to the reaction coordinate. The thermodynamic stability of the tautomers is governed by substrate interaction, so that the *trans* tautomer is stable on Cu(111) while on Cu(110) the *cis* tautomer is stable. Inelastic electron tunneling from the STM tip drives the tautomerization reaction to the metastable *cis* state and between mirror symmetric *cis* states on Cu(111). Thermal excitation can react the molecule back to the thermodynamically stable tautomer via hopping diffusion.

4.4 Photoinduced Porphycene Tautomerization

Porphycene molecules are adsorbed on the Cu(111) surface which is prepared as described in section 3.3. The molecules adsorb homogeneously distributed on clean surface terraces in the thermodynamically stable *trans* state (Fig. 4.9(a)), isolated from each other and without the formation of clusters and islands. Upon laser irradation, the molecules convert to the metastable *cis* state (Fig. 4.9(b)) in a unidirectional fashion. Fig. 4.9(c) shows a typical STM image of a 25×25 nm^2 section on the surface directly after molecule evaporation at a surface coverage of ∼0.08 nm^{-2}. STM imaging is performed at an applied bias below the threshold for tunneling electron induced tautomerization so that all molecules appear stationary in the *trans* configuration (see section 4.3). After imaging, the STM tip is retracted by ∼2 μm from the surface and the entire sample is exposed for 2 min to 405 nm wavelength CW laser radiation with a total power of 2.7 mW. The same spot on the sample is imaged again which reveals that a fraction of the *trans* molecules has converted to the *cis* state (white circled in Fig. 4.9(d)). In order to convert all molecules back to the *trans* state, the sample is heated up to ∼35 K (Fig. 4.7). Reversible *cis* ↔ *cis* conversion was also observed upon photoexcitation (red circle in Fig. 4.9(d)) but no *cis* → *trans* or *trans* → *trans* reaction, analogous to the tautomerization reactions which are

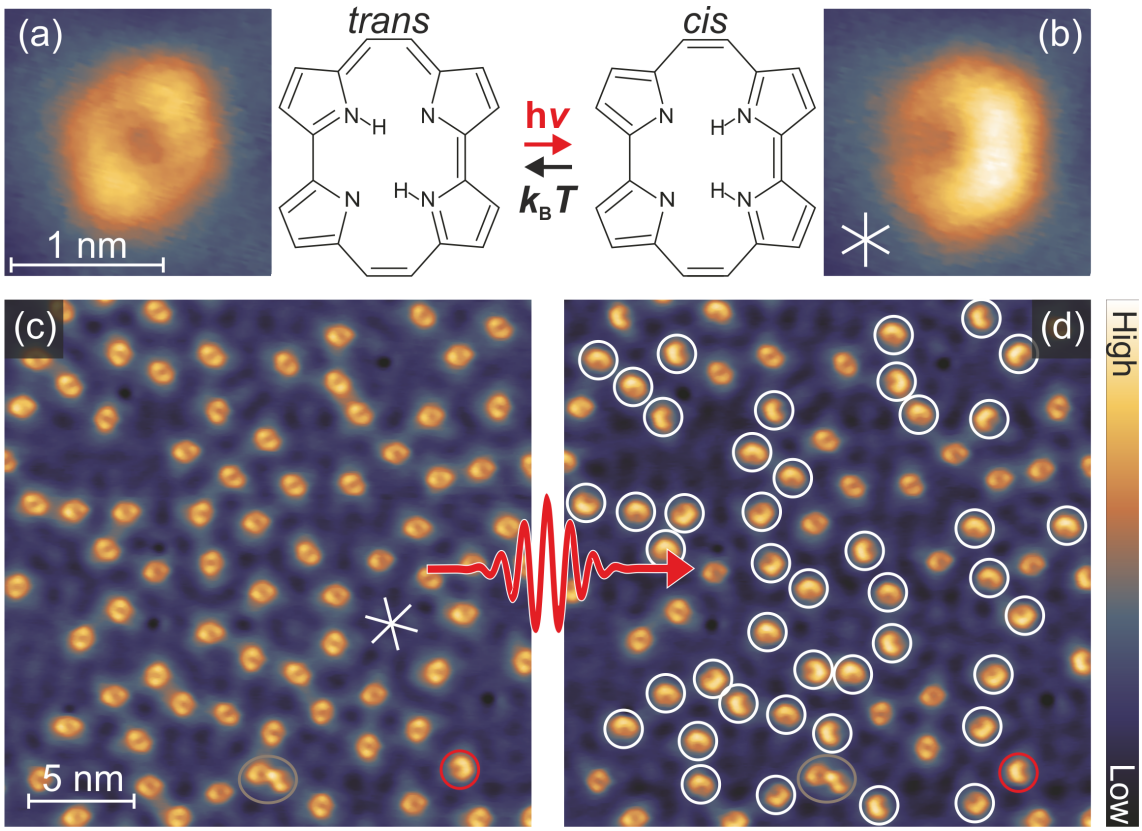

Figure 4.9: STM images of a single porphycene molecules in the (a) *trans* and (b) *cis* configuration on Cu(111) at 5 K (size: 1.75×1.75 nm^2 , V_t = 100 mV, I_t = 100 pA). The chemical structures are displayed next to the image. The white lines in image (b) represent the high-symmetry axes of the surface. (c) Large-scale STM image after molecular deposition (size: 25×25 nm^2, V_t = 50 mV, I_t = 50 pA). (d) The same area as (c) after irradiation with a 405 nm diode laser (CW, 2.7 mW) for 2 min. Switched molecules are marked by white circles. The STM tip was retracted by ∼2 μm from the surface during irradiation. Grey circle marks defect bound molecules and red circle *cis* ↔ *cis* conversion.

induced by inelastic tunneling electrons on Cu(111) (see section 4.3). The experimental conditions to quantitatively examine the photoinduced tautomerization reaction however require the observation of a unidirectional process to unambiguously determine molecules which have undergone tautomerization. Since the tip needs to be retracted during light exposure, reversible conversions are not discernible since only the initial and final states of the molecule may be observed. For this reason, the following study will exclusively discuss the *trans* → *cis* conversion. It should be further noted that porphycene is found to bind to surface defects which alters the reaction potential landscape so that these molecules are excluded from the quantitative study of photoinduced tautomerization, as the reaction dynamics are expected to differ significantly (grey circle in Fig. 4.9(d)). Fig. 4.10(a) shows the proportion of tautomerized molecules (N_{cis}/N_{total}, blue filled circles) and the corresponding fraction of unreacted molecules (N_{trans}/N_{total}, red filled circles) as function of incident photon fluence (n_{ph}, dosed photons per cm^2) at 405 nm wavelength excitation. The number of total molecules N_{total} (∼1000 in all here presented measurements)

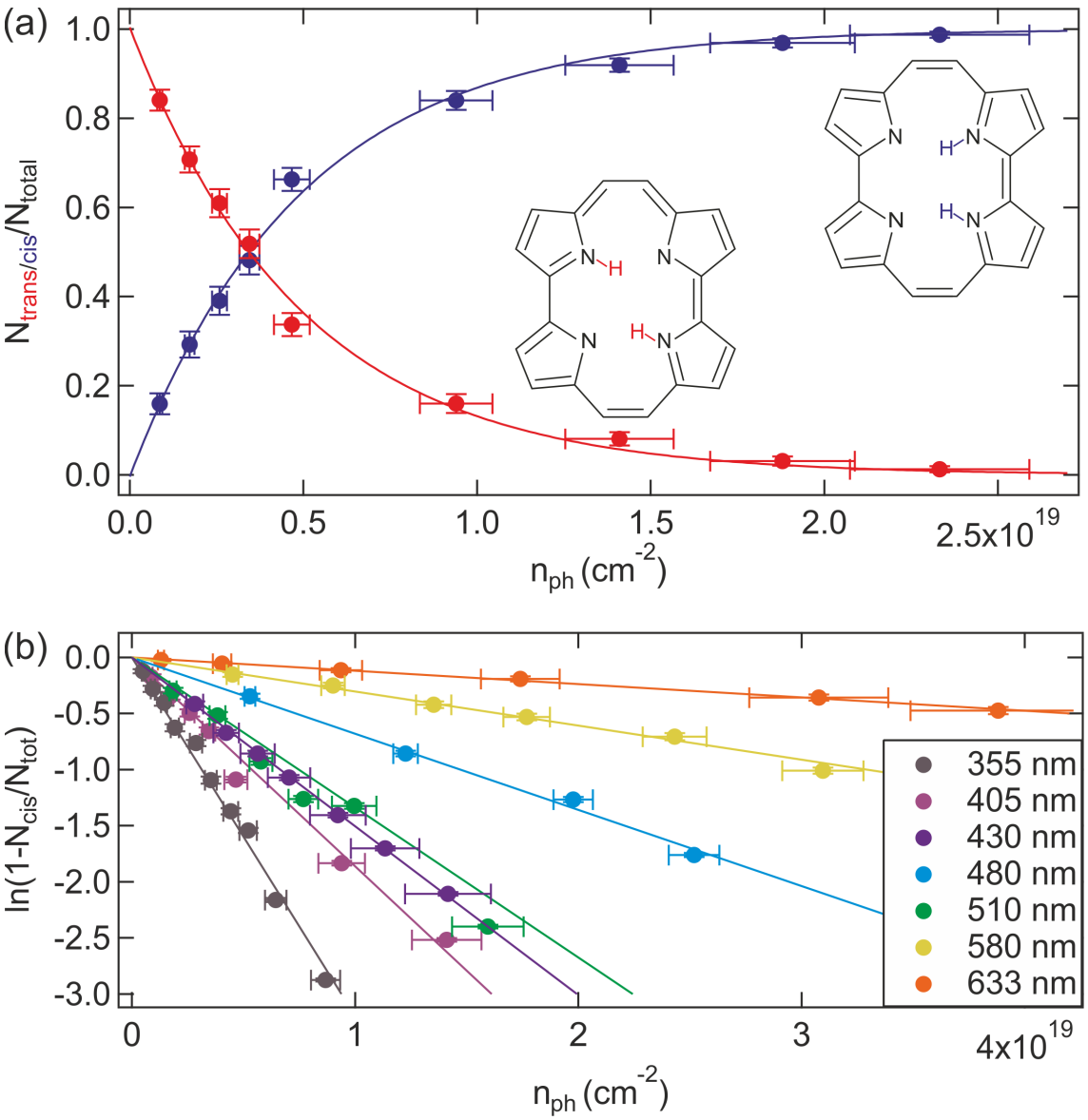

Figure 4.10: (a) Fraction of reacted molecules N_{cis}/N_{total} (blue) and corresponding unreacted molecules N_{trans}/N_{total} (red) as a function of n_{ph} at 405 nm wavelength excitation. The solid curves represent a fit to Eq. 4.2 (red) and Eq. 4.3 (blue). (b) Semi-logarithmic plot $ln(\frac{1-N_{cis}}{N_{total}})$ as a function of n_{ph} at various excitation wavelengths. The solid lines represent a fit to Eq. 4.2.

is a statistical subset from the entire population of molecules adsorbed on the surface, which is determined from the number of molecules, captured in multiple STM images from random spots on the surface. Since only two tautomers are found on the surface when spatial orientation and mirror symmetric states are omitted, N_{total} is the sum of N_{trans}, which is the number of *trans* molecules within this subset and N_{cis}, the number of *cis* molecules, which are discriminated by their specific appearance in STM images. At n_{ph}=0 cm^{-2}, all molecules are found in the *trans* state. However, upon irradiation, the entire population converts unidirectionally to the *cis* state. The photon fluence at the sample is determined from the photon flux and the cumulated duration of light exposure. The

measurement procedure is described in detail in section 3.5. The reacted proportion of molecules N_{cis}/N_{total} can be deduced after each time interval of light exposure by STM imaging. The statistical error of this procedure that stems from the fact that only a subset of the molecule population is randomly probed, can be estimated by:

$$\frac{N_{cis}}{N_{total}} \pm z\sqrt{\frac{1}{N_{total}}\frac{N_{cis}}{N_{total}}\left(1-\frac{N_{cis}}{N_{total}}\right)} \tag{4.1}$$

where z is the percentile of a standard normal distribution at a specific confidence interval, which becomes 1.96 at a 95% interval. The meaning of this error estimation is that the true reacted proportion of the molecule entity is with 95% probability within 1.96 standard errors of the determined proportion from random sampling.
The evolution $N_{cis/trans}/N_{total}$ can be fitted by exploiting that the *trans* $\rightarrow$ *cis* tautomerization follows a first-order rate law which is described by a single exponential:

$$\frac{N_{cis}}{N_{total}} = 1 - exp\left(-\sigma_{t\rightarrow c} n_{ph}\right) \tag{4.2}$$

$$\frac{N_{trans}}{N_{total}} = exp\left(-\sigma_{t\rightarrow c} n_{ph}\right) \tag{4.3}$$

where $\sigma_{t\rightarrow c}$ is the photoreaction cross section at the specific excitation wavelength. The experimental data in Fig. 4.10(a) is fit to Eq. 4.2 (blue curve) and Eq. 4.3 (red curve), respectively.
Fig. 4.10(b) displays a semi-logarithmic plot of $1 - N_{cis}/N_{total}$ as a function of photon fluence at varying incident wavelength in p-polarization with the corresponding fits, according to Eq. 4.2. The cross section may be directly deduced as it is given by the fit slope:

$$\sigma_{t\rightarrow c} = -\frac{\left(1 - ln\left(\frac{N_{cis}}{N_{total}}\right)\right)}{n_{ph}} \tag{4.4}$$

It is clear that $\sigma_{t\rightarrow c}$ is dependent on incident wavelength, while the process obeys a first-order rate law for all wavelength, so that the influence of a photoinduced backward reaction *cis* $\rightarrow$ *trans* which may result from surface heating can be excluded. In order to ensure the reproducibility of the above results, we examined possible sources for systematic error in the experiment, additional to the statistical error that we accounted for. Possible sources of systematic error could stem from variations in the generated laser beam profile and power which is used to determine the incident photon flux as well as from sample to sample variations after repeated preparation. Fig. 4.11(a) and (b) show two different beam profiles, generated from a 445.8 nm diode laser. The corresponding photon flux is indicated at the bottom of both profiles. Albeit the variation in photon flux, the measured cross section reveals a statistically negligible difference between the measurements from (a) $2.06(\pm 0.11)\times 10^{-19}$ cm^2 to (b) $2.08(\pm 0.43)\times 10^{-19}$ cm^2 (Fig. 4.11(c)), thus we conclude that the photon flux is correctly examined and the beam conditions have no significant influence on the measurement. We examined the sample to sample variation by measuring the cross section at 532 nm wavelength photoexcitation for two different samples which were prepared with a molecule surface coverage of $\sim$0.08 nm^{-2}. The corresponding cross sections were determined as $1.34(\pm 0.04)\times 10^{-19}$ cm^2 and $1.23(\pm 0.02)\times 10^{-19}$ cm^2 for sample #1 and #2, respectively, hence the sample to sample variation was estimated to be $\sim$10%. Within these limits, the spectral variation of the photoreaction cross section will be discussed in the following.

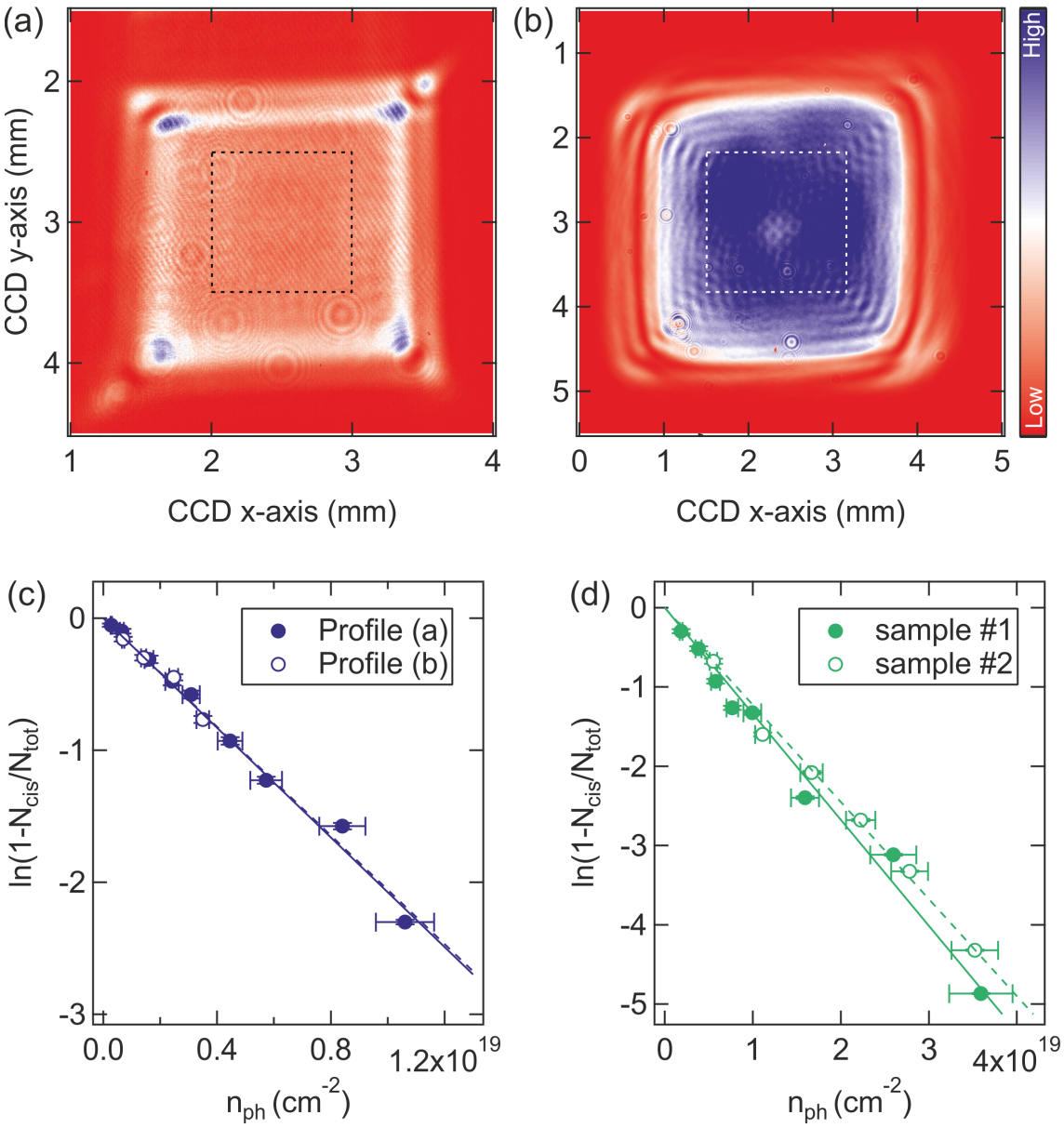

Figure 4.11: (a),(b) Beam profiles from a 445.8 nm diode laser. The corresponding photon flux (n_{ph}/t_{ill}, where t_{ill} is the duration of sample exposure) within the junction aligned beam part (dashed square) is (a) $4.59(\pm0.31)\times10^{15}$ $cm^{-2}s^{-1}$ and (b) $1.16(\pm0.05)\times10^{16}$ $cm^{-2}s^{-1}$. (c) Semi-logarithmic plot of the tautomerized molecule proportion as function of incident photon fluence. The cross section is determined from fitting the data to a first-order rate law which yields for beam profile (a) $\sigma_{t\rightarrow c}=2.06(\pm0.11)\times10^{-19}$ cm^2 (solid line) and (b) $\sigma_{t\rightarrow c}=2.08(\pm0.43)\times10^{-19}$ cm^2 (dashed line). (d) Sample to sample variation for repeated measurements at similar molecule surface coverage ($\sim$0.08 nm^{-2}), examined at 532 nm excitation wavelength. Sample #1: $\sigma_{t\rightarrow c}=1.34(\pm0.04)\times10^{-19}$ cm^2 (solid line), Sample #2: $\sigma_{t\rightarrow c}=1.23(\pm0.02)\times10^{-19}$ cm^2 (dashed line).

4.5 Photogenerated Charge Carrier Driven Excitation Mechanism

The photoexcitation of adsorbates on metal surfaces can be classified into direct and indirect mechanisms, where the former involves an electric-dipole transition within the adsorbate-metal complex which initiates nuclear dynamics while the latter describes charge carrier excitation within the metal which can scatter through adsorbate electronic states to transfer energy [2]. Details of these processes are described in section 2.2. The photoexcitation energy, polarization and power dependence on the reaction yield is a valuable information to discriminate between the mechanisms and determine the dominant excitation channel [165, 166].

Fig. 4.12(a) displays the photoinduced cross section $\sigma_{t\to c}$ as function of photon energy (wavelength), measured for both p- (red filled circles) and s-polarization (blue filled circles) at an incident angle of 65° from the surface normal (Fig. 4.12(b)). The cross section steeply rises up to ∼2.3 eV and moderately increases at higher excitation energies. Furthermore, p-polarized excitation yields larger cross sections across the entire investigated energy range. The spectral dependence suggests a substrate absorption dominated excitation mechanism which is governed by d-sp interband transitions (Fig. 4.12(d)). Within the boundaries of a simple approximation, the spectral variation of the cross section should follow the polarization dependent absorption of the Cu substrate $A_{p,s}$, which quantifies the number of generated charge carriers N_{cc}. The fraction of charge carriers which may reach the surface and attach to the porphycene is estimated from the mean free path in copper which is simplified with an excitation energy independent cutoff distance $\delta \approx$10 nm within which we assume a constant probability to reach the surface and induce the tautomerization. The relation between $\sigma_{t\to c}$ and N_{cc} is modeled by [165]:

$$\sigma_{t\to c} \sim N_{cc} = \left[N_{ph} A_{p,s} \left(1 - exp\left(-\frac{\delta}{D} \right) \right) \right]^m \tag{4.5}$$

where N_{ph} is the number of photons and D the penetration depth of a photon into the copper substrate which is estimated by $D = \lambda/(2\pi k)$. λ is the incident excitation wavelength and k the extinction coefficient of copper. k and $A_{p,s}$ are taken from experimental data provided in ref.[168]. The parameter m accounts for multi-photon processes which may occur, for example in strong laser fields and it can be derived from the power dependence of $\sigma_{t\to c} \propto P^n$, where P is the incident laser power and $m = n + 1$, since $\sigma_{t\to c}$ is a quantity that is already normalized to the power. Fig. 4.12(c) shows the power dependence in the accessible intensity range for 405 nm (purple filled circles) and 445.8 nm (blue filled circles) exitation wavelength. A power law fit yields $m \approx 0.98$ and $m \approx 0.67$ for 405 nm and 445.8 nm, respectively. Since m can only take integer values, we conclude that photoexcited tautomerization is a single-photon process and assume $m = 1$ to estimate the hot carrier excitation rate, which is depicted in Fig. 4.12(a) for p- (red curve) and s-polarization (blue curve). The fit qualitatively reproduces the data which supports the assumption that the generation of substrate charge carriers is the main excitation channel to drive photochemistry on the surface. Nevertheless, the fit does not entirely match the magnitude of cross section variation with incident energy and systematically overestimates at excitation energies below about 2.3 eV and underestimates above. This mismatch may result from the simplifications made in the model, e.g. the energy independence of δ and discrimination of the charge carrier energy distribution at the surface, since a larger reaction yield can be

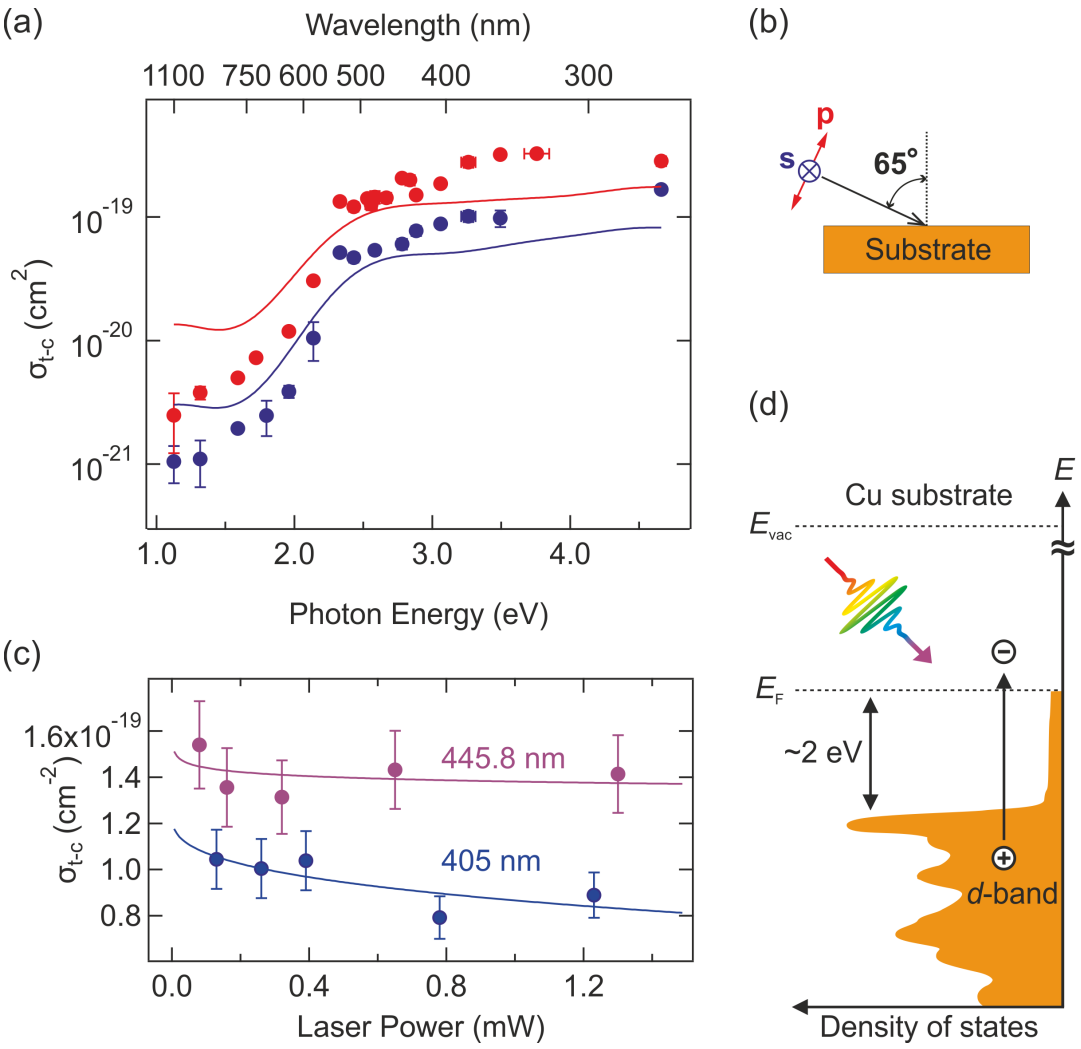

Figure 4.12: (a) Excitation energy (wavelength) dependent cross section $\sigma_{t\to c}$ measured with p- (red filled circles) and s-polarized (blue filled circles) incident light. The cross section is fit to Eq. 4.5 (curves) (b) Schematic of experiment geometry. The incident beam angle is 65° with respect to the surface normal. (c) Cross section dependence on incident laser power at 445.8 nm (purple filled circles) and 405 nm (blue filled circles) excitation wavelength. The solid lines represent a power law fit. (d) Schematic of the proposed photoexcitation mechanism as a function of substrate electronic density of states (calculated [167]). The photogeneration of charge carriers in the copper substrate creates a distribution of energetic charge carriers which can attach to the molecule and drive the tautomerization.

expected for higher energy charge carriers which attach to the porphycene molecules (see section 4.3). The higher the photoexcitation energy, the more charge carriers may retain larger energies before randomization via electron-electron scattering.

4.6 Non-Adiabatic Coupling to Reaction Coordinate

The main contribution to the photoexcitation of porphycene tautomerization was elucidated to be substrate charge carriers which may attach to the molecule. Photoexcitation is therefore similar to direct vibrational excitation via energetic tunneling electrons which are directly injected from the STM tip. In order to clarify how the initial excitation relaxes to the tautomerization coordinate, we therefore compare STM-induced with photoinduced tautomerization for both undeuterated (H-Pc) and cavity deuterated porphycene (D-Pc) (Fig. 4.13(a)). The substitution of inner cavity hydrogen with deuterium should have profound impact on the reaction dynamics as both intermode coupling as well as the zero-point energy are influenced [104].
Fig. 4.13(b) shows the evolution of converted porphycene molecules as function of photon fluence at 532 nm wavelength p-polarized excitation. The photoreaction cross section for H- and D-Pc was determined as $\sigma_{t\rightarrow c}$=1.34($\pm$0.04)$\times10^{-19}$ cm^2 and $\sigma_{t\rightarrow c}$ = 1.55($\pm$0.14) $\times$ $10^{-21}cm^2$, respectively, thus revealing an isotope ratio of 86$\pm$8. For photoexcitation of a planar metallic surface, the short mean free path of excited charge carriers in the substrate causes thermalization so that the majority should have an energy close to the Fermi energy when they reach the surface and attach to the adsorbate [2]. Therefore, porphycene tautomerization by low-energy photoexcitation and direct STM excitation are directly compared to gain insight into the reaction mechanism. Fig. 4.13(c) displays the STM bias dependent reaction yield for H-/D-Pc. Similar to vibrational excitation by tunneling electrons of the *cis* $\leftrightarrow$ *cis* conversion on Cu(110), as described in section 5.3.1, within the bias range, where only excitation of skeletal vibration modes is possible, D-Pc shows a lower yield by a factor of 100-360, whereas the yield rises steeply as soon as the N-D stretch mode (ν(N-D)) is excited. The reason for this large isotope ratio in the skeletal mode range is investigated by measuring the tunneling current dependent reaction rate at V_t = -250 mV for H-Pc and V_t = -230 mV for D-Pc, thus below the threshold of the N-D stretch vibration (Fig. 4.13(d)). It is observed from a power law fit ($R \propto I^N$), that $N \approx 1$ for H-Pc and $N \approx 2$ for D-Pc. Hence, the tautomerization of cavity deuterated porphycene requires multiple excitations of skeletal mode vibrational quanta to overcome the reaction barrier, which is less likely to occur and consequently manifests in a much lower reaction yield. It is therefore proposed that the isotope ratio of photoexcited *trans* $\rightarrow$ *cis* conversion is similarly high, because most attached charge carriers exhibit an energy within the range of skeletal vibrations below about 260 meV, so that the situation closely resembles STM-induced conversion. The proposed mechanism is summarized in Fig. 4.14. The primary excitation from attached charge carriers excites the molecules into a transient ionic state from which it relaxes (Fig. 4.14(a)). Skeletal vibrations are excited upon relaxation to the ground state by non-adiabatic coupling and distort the reaction potential non-uniformly along the tautomerization coordinate via intermode coupling. The required number of vibrational quanta which is needed to overcome the reaction barrier is observed to be higher for D- than for H-Pc, due to weaker anharmonicity and lower zero-point energy, so that the potential landscape may be less deformed upon vibrational excitation which significantly lowers the observed reaction cross section. The photoexcited process closely resembles the mechanism of inelastic tunneling electron induced conversion which is described in section 4.3. The stability inversion between *trans* and *cis* state, due to the difference in lifetime of the tautomers on the Cu(111) surface explains the unidirectionality of the photoreaction. Our experimental results may, however, not clarify the dominant na-

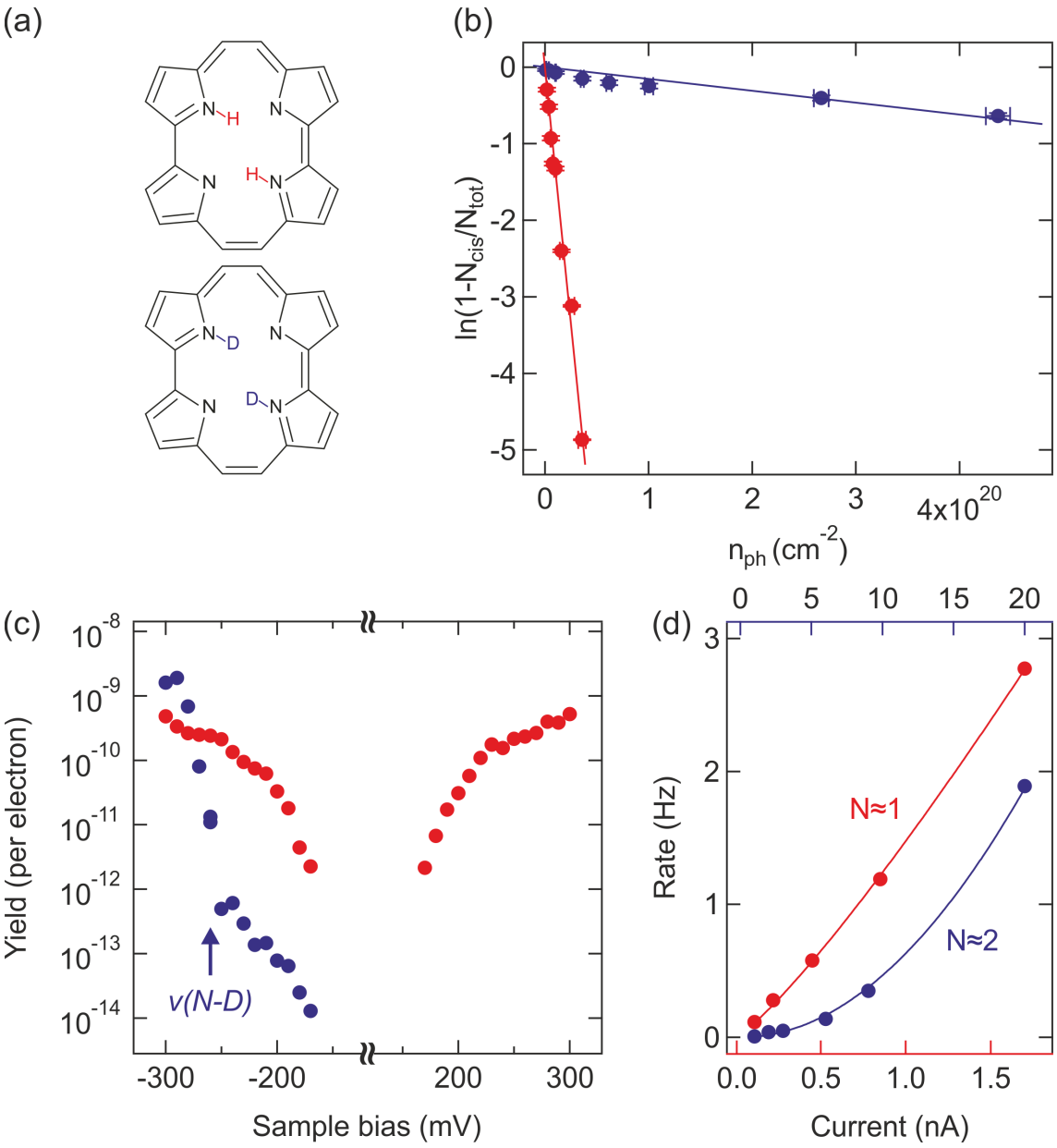

Figure 4.13: (a) Structure model for H-Porphycene (Pc) (top) and D-Pc (bottom) (b) $ln(\frac{1-N_{cis}}{N_{total}})$ as a function of n_{ph} at 532 nm excitation wavelength, measured for H- (red) and H-Pc (blue). The solid lines represent a fit to Eq. 4.2. (c) Voltage dependence of tunneling electron induced *trans* $\rightarrow$ *cis* conversion yield for H- (red) and D-Pc (blue). (d) Tunneling current dependent tautomerization rate measured at V_t = -250 mV for H-Pc (red) and V_t = -230 mV for D-Pc (blue). The experimental data was fit to a power law (Rate$\propto I^N$), thus revealing a one electron process for H- and a two electron process for D-Pc at the applied bias.

ture of attached hot carriers which drive the reaction, as it was shown that both, holes and electrons, can induce the reaction with the same efficiency (Fig. 4.13(c)). Hole attachment has been identified to be dominant for isomerization of azobenzene derivatives on Au and

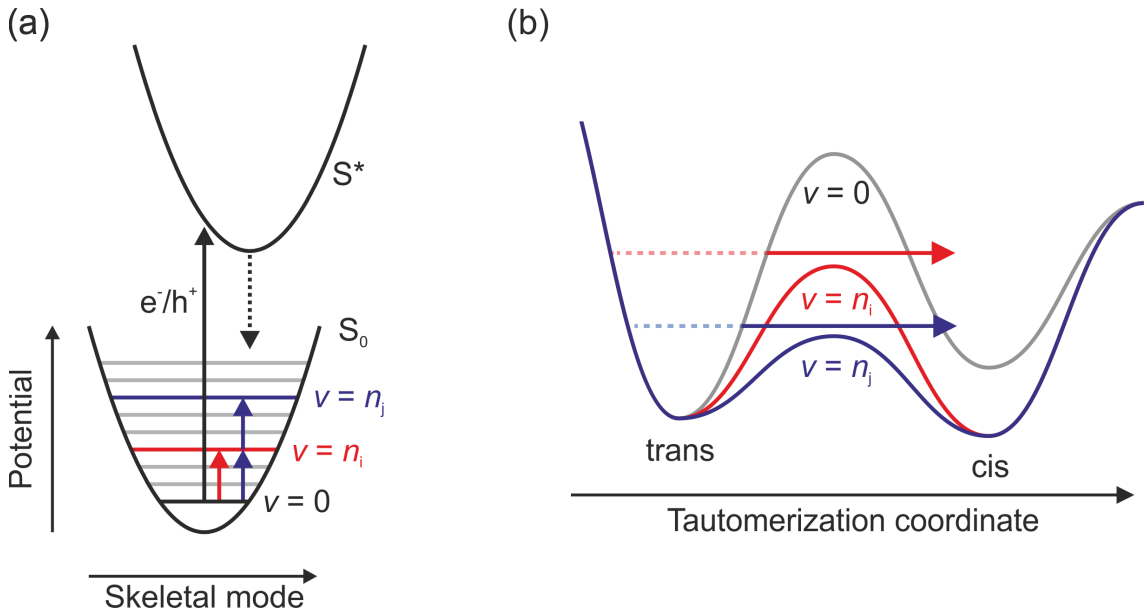

Figure 4.14: (a) Schematic of the ground state ($S_0, \nu = 0$) and ionic state (S^*) potential. The molecule is transiently excited to the ionic state by photoexited charge carrier attachment. After relaxation to the ground state, molecular skeletal vibrations are excited which couple to the tautomerization coordinate. (b) Schematic potential along the tautomerization coordinate. Upon skeletal mode excitation, the activation barrier is reduced and the reaction from the thermodynamically stable *trans* to the metastable *cis* state is promoted. Different vibrational quanta $n_{i,j}$ where $i < j$ are required to induce the reaction for H- (red arrow) and D-Pc (blue arrow). The dashed lines represent the zero-point energy.

Cu surfaces upon d-sp band excitation [130, 169]. Within this regime, the deposited energy to electrons is small but the low reaction threshold of about 150 meV can be overcome even by low-energy carriers, so that we do not ascribe the reaction excitation to be dominated by either.

4.7 Modulation of Potential Landscape by Surface Coverage Variation

It was found in STM studies of porphycene tautomerization on Cu(110) that a single Cu adatom, located within ∼1 nm from a porphycene molecule, can strongly distort the reaction potential landscape through electronic and elastic interaction, thereby underlining the importance of the local environment on the stability of the observed tautomeric form [158]. Furthermore, on Cu(111) the existence of the surface state resonance was proven to have a crucial impact on the observed reaction yield by inelastic electron excitation, as electrons from the STM tip may travel along the surface and induce the reaction several nanometer away from the tip position. At higher coverages, the surface state is quenched, which is accompanied by a drop of the reaction yield [161]. The reaction potential can

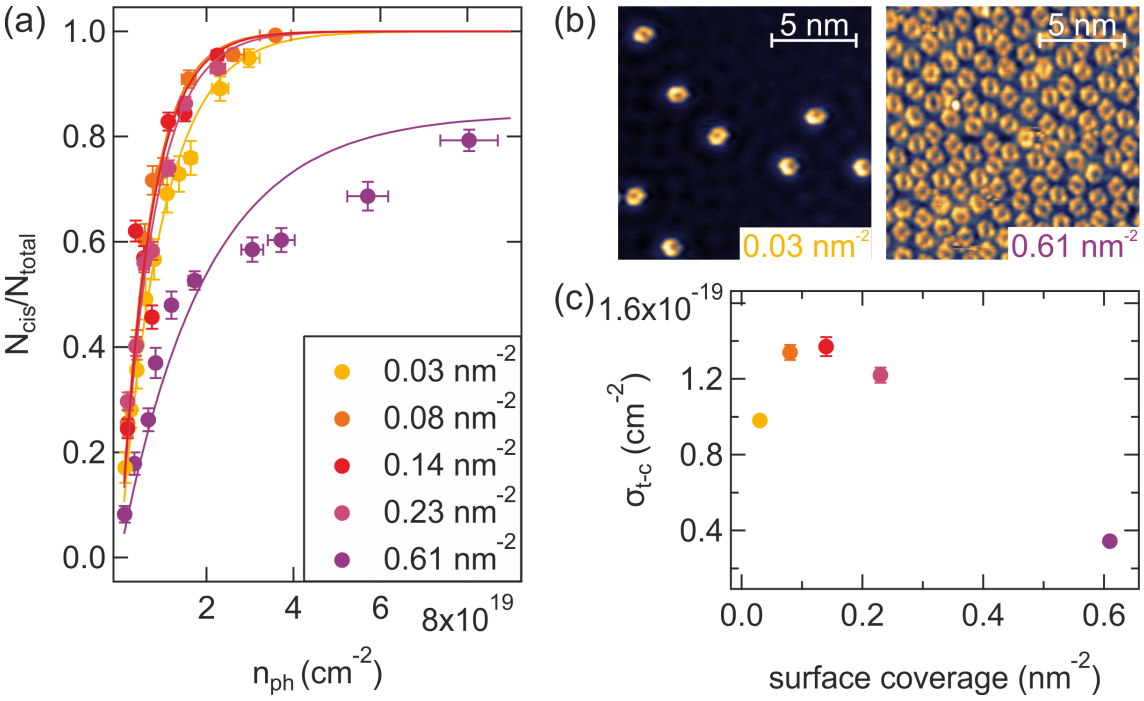

Figure 4.15: (a) Fraction of reacted molecules N_{cis}/N_{total} as function of n_{ph} at 532 nm excitation wavelength at various surface coverages of adsorbed molecules. The solid curves represent a fit to Eq. 4.2. (b) STM images at representative coverages of 0.03 nm^{-2} and 0.61 nm^{-2} (size: 15×15 nm^2, V_t = 50 mV, I_t = 50 pA). (c) Measured tautomerization cross section $\sigma_{t\rightarrow c}$ as a function of surface coverage.

further be influenced by the proximity of other molecules, so that the local environment and surface coverage are important parameters which are expected to impact also the photoexcited reaction. Fig. 4.15(a) displays the proportion of reacted molecules as function of photon fluence at 532 nm excitation wavelength at various surface coverages of adsorbed molecules. Exemplary STM images at 0.03 nm^{-2} and 0.61 nm^{-2} measured coverage are shown in Fig. 4.15(b). It was previously found that the arrangement of porphycene on Cu(111) is mediated by the Cu(111) surface state, thereby causing an oscillatory pattern of intermolecular distance that matches a modulation with the Fermi wavelength [161]. At higher coverages, the molecules cannot maintain long-range order along the surface state anymore and the nearest neighbor distance decreases at a threshold of ∼0.1 nm^{-2}. Due to scattering and interference with adsorbed molecules, the surface state is quenched at higher coverages which results in a drop of the STM-induced reaction yield as injected carriers may not travel anymore along the surface state. Fig. 4.15(c) shows the measured cross section as function of coverage which exhibits a maximum at ∼0.1 nm^{-2}, thus suggesting a correlation of the photoexcited reaction with the surface state. Excited charge carriers are not confined efficiently to the surface when the surface state is quenched which lowers the number of charge carriers that attach to porphycene molecules. At a coverage of 0.61 nm^{-2}, it is further observed that the reaction does not follow a first-order rate law anymore (purple solid curve in Fig. 4.15(a)) and complete conversion of all molecules to the *cis* state is impeded. As the nearest neighbor distance at this coverage is below 1 nm, strong distortion of the reaction potential landscape may be expected, similar to

intentional positioning of adatoms near the molecule. Therefore, the reaction dynamics are dependent on the individual molecular environment and cannot be assumed to be equal for all molecules which is a necessary precondition for extracting a cross section from a single exponential fit to the reacted molecular proportion. The observation of non-reacting molecules may stem from defect pinning or potential landscape deformation in a way that the reaction cannot be induced by photoexcitation at the incident photon energy. The cross section coverage dependence therefore suggests that photoexcited charge carriers distribute along the surface state on Cu(111) and that intermolecular interaction may distort the potential landscape of the individual molecule.

4.8 Conclusion

The presented work demonstrates the photoexcited unidirectional porphycene tautomerization from the thermodynamically stable *trans* to the metastable *cis* state on Cu(111). We found that the photoreaction follows a first-order rate law with a strong cross section dependence on incident excitation energy, which was studied across the entire near-IR to UV range. The reaction cross section follows qualitatively the substrate absorption, which was verified by a simple estimation of the charge carrier excitation rate. It is therefore concluded that porphycene tautomerization is mediated by photoexcited substrate charge carriers via non-adiabatic coupling. A pronounced isotope effect of the measured cross section suggests primarily molecular skeletal mode vibration excitation, as rationalized from voltage and current dependent tunneling electron induced tautomerization. Anharmonic intermode coupling leads to non-uniform deformation of the potential landscape along the reaction coordinate, which is less pronounced for isotope substituted porphycene. Interaction between molecules was further demonstrated to strongly influence the photoreaction as the potential landscape may be distorted.
Tautomerization within a H-bonded system inherently acts on an ultrafast timescale, as only intramolecular proton motion is involved. This motion may compete with the timescales of excited state relaxation due to strong molecule-substrate coupling on metal surfaces. Photoresponsive selective conversion can be readily realized with a single-molecule tautomeric switch which provides high efficiency and operates without skeletal rearrangement.

5 Plasmon Mediated Porphycene Tautomerization in an STM Junction

Optical near-field enhancement in metallic nanostructures can be used to significantly increase the reaction yield of photochemical reactions. Nanostructures made of Au, Ag, and Cu are commonly employed as a photocatalytic substrate because of plasmonic resonances in the visible and near-IR spectral range, which can facilitate the use of sunlight to drive photochemistry [170]. However, few studies have yet addressed the microscopic details of optical near-field induced chemistry, as it remains a challenging task to investigate near-field reactions in individual nano-gaps with spectroscopic methods on the molecular level. Quantitative insight into the photochemical enhancement has not yet been demonstrated as the direct observation was not achieved with active control over the near-field coupling strength. The presented work explores a new possibility to directly study near-field enhanced chemistry at the single-molecule level in a nanoscopic gap.
We report the near-field enhanced tautomerization of porphycene on a Cu(111) and Cu(110) surface in an STM junction. The light-induced tautomerization using far-field excitaion is mediated by photogenerated carriers in the Cu substrate, whereas in the tunneling regime optically excited tunneling dominates the process. Direct photoexcitation of the molecule can be excluded by examination of different adsorbate species. It is revealed that the reaction cross section is significantly enhanced by surface plasmon excitation in the presence of a Au tip compared to the far-field induced process. The strong enhancement implies an enhancement factor of $\sim 10^2$-10^3 and occurs in the red and near-IR spectral range for Au tips, whereas a W tip exhibits almost no enhancement, as W does not exhibit plasmonic resonances in the investigated energy range.
Plasmon mediated porphycene tautomerization is further employed to locally probe the near-field properties within the STM junction. It is found that surface plasmon excitation from structural features on the tip shaft by a spatially broad light source yields standing wave resonances between multiple excitation sources. The near-field response at the apex can be engineered by tip surface structuring and the formation of cavity resonances between apex and fabricated microstructure. Scanning Tunneling Microscopy Luminescence (STML) provides direct evidence for the formation of a resonator using the inelastic tunneling current as a local source for surface plasmon excitation.

5.1 Local Spectroscopy and Photochemistry in an STM Junction

On the basis of a fundamental description of electromagnetic interaction between a nanoscopic tip and a flat surface, the principles of plasmonic excitation and field enhancement in a nano-gap are outlined. Commonly employed methods that exploit this interaction to probe elementary excitations at the nanoscale are further introduced, with specific emphasis on the yet sparsely explored field of near-field mediated reactions in an SPM junction.

5.1.1 Plasmonic Coupling to a Sharp Metal Tip

The interaction of a sharp free standing metallic tip with an incident electromagnetic field $\mathbf{E}_{inc}(\omega)$ is described by approximating the tip with an effective point dipole at the tip apex, analogous to the description of a metallic sphere in section 2.3. When the polarization of the incident field is taken into account, the polarization dependent dipole moment is given by [29]:

$$\mathbf{p}_{Tip}(\omega) = \begin{bmatrix} \alpha_\perp & 0 & 0 \\ 0 & \alpha_\perp & 0 \\ 0 & 0 & \alpha_\parallel \end{bmatrix} \epsilon \mathbf{E}_{inc}(\omega) \tag{5.1}$$

where ϵ is the dielectric constant of the surrounding medium (ϵ=1 in air/vacuum) and the z-axis coincides with the tip axis. The transverse and longitudinal polarizabilities $\alpha_\perp$ and $\alpha_\parallel$ are defined by:

$$\alpha_\perp(\omega) = 4\pi\epsilon_0 R^3 \frac{\epsilon_{Tip}(\omega) - \epsilon}{\epsilon_{Tip}(\omega) + 2\epsilon} \tag{5.2}$$

$$\alpha_\parallel(\omega) = 2\pi\epsilon_0 R^3 f_e(\omega) \tag{5.3}$$

where ϵ_0 is the vacuum permittivity, $\epsilon_{Tip}(\omega)$ the incident frequency dependent complex permittivity of the tip material, R the tip apex radius and $f_e(\omega)$ the complex field enhancement factor, which may be obtained from electromagnetic analytical or numerical calculations. In this approximation, $\alpha_\perp(\omega)$ is identical to the polarizability of a nanoscopic sphere.

Fig. 5.1(a) displays a schematic of the dipole approximated metallic tip, illuminated by an incident electromagnetic field, polarized along the tip axis. The electric field is strongly increased in the apex vicinity and decays rapidly on the apex radius length scale. The incident field drives free electrons in the metal along the direction of polarization and induces an oscillating surface charge density which forms standing waves with a node at the apex, when the incident field is polarized along the tip axis. For perpendicular polarization, the apex remains uncharged and the field enhancement is negligible. In addition to the resonant plasmonic enhancement which strongly depends on the frequency dependent metal dielectric constant, there is non-resonant enhancement at the apex which results from the lightning rod effect. The induced surface electron density is concentrated at the tip apex, as the electrons are accelerated in the direction of the electric field. Hence, the geometrically imposed spatial confinement at the apex results in an accumulation of electrons and yields a near-field enhancement which is largely independent of the excitation frequency. The enhancement magnitude is mainly governed by the curvature radius. However, sharp tips were shown to poorly couple to far-field radiation which is circumvented by coupling to evanescent wave excitation or nanofabricated structures on the tip like apex attached nanoparticles or surface engraved gratings which may couple to optically dark traveling surface plasmons with subsequent adiabatic focusing to the apex [171–173].

The local field enhancement and confinement can be further increased by bringing the tip in close proximity of a metallic substrate, whereby a nano-gap is formed. Upon incident excitation polarized along the tip, the induced tip dipole moment itself induces an image dipole moment in the surface, hence creating a tip-sample coupled effective dipole resonance. For perpendicular excitation, the dipole and image dipole depolarize each other,

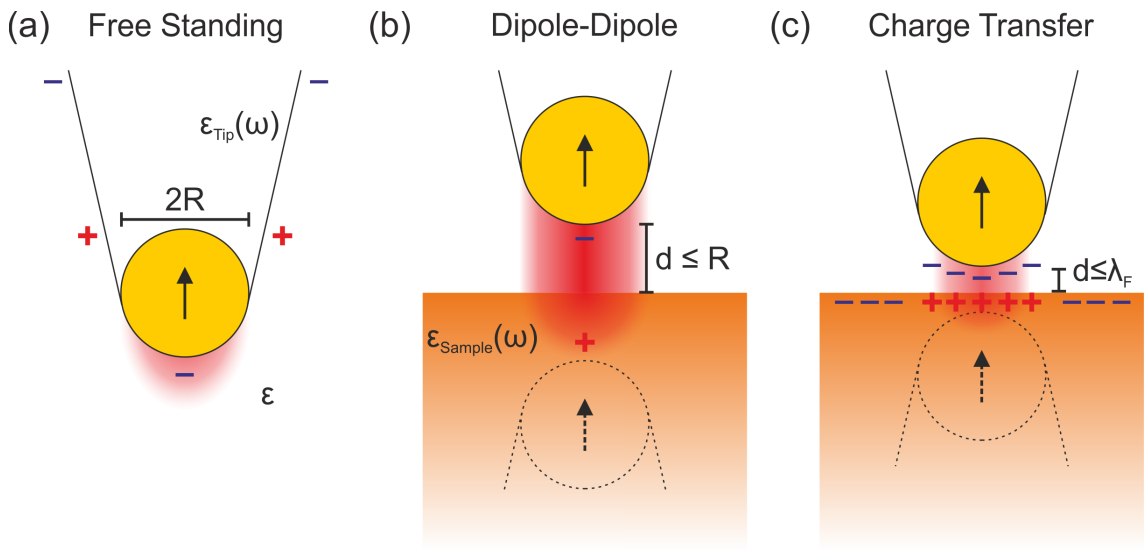

Figure 5.1: (a) Schematic of a free-standing metallic tip, illuminated along the tip axis. The induced dipole oscillation launches a propagating surface plasmon along the tip. (b) Tip in proximity of a metallic sample. Dipole-dipole coupling with the induced image dipole results in increased field enhancement in a formed nano-gap. (c) Tip in tunneling charge transfer distance to sample. The near-field weakens and the plasmonic response is heavily modified.

so that only very weak enhancement occurs in the gap. Consequently, only the former case is considered in the following. Fig. 5.1(b) displays a tip in proximity to the sample. The tip and image dipole mutually polarize each other thus increasing the electric field in the junction. The tip polarizability is given by Eq. 5.2, while the sample polarizability is analogously derived from Maxwell's equations as:

$$\beta(\omega) = \frac{\epsilon_{Sample}(\omega) - 1}{\epsilon_{Sample}(\omega) + 1} \tag{5.4}$$

where $\epsilon_{Sample}(\omega)$ is the frequency dependent sample dielectric constant. The effective coupled polarizability is obtained from a superposition of incident and dipole emitted electric field [29]:

$$\alpha_{eff}(\omega) = \frac{\alpha_{\perp}(\omega)(1 + \beta(\omega))}{1 - \frac{\alpha_{\perp}(\omega)\beta(\omega)}{16\pi(R+d)^3}} \tag{5.5}$$

where d is the gap distance between tip and sample. The distance dependent local field enhancement magnitude at fixed incident frequency is therefore given by:

$$\frac{|\mathbf{E}_{loc}(d)|}{|\mathbf{E}_{inc}|} \propto \frac{2R + d}{d} \tag{5.6}$$

In this relation it is clear that the classical approximation breaks down, when $d \to 0$, resulting in an infinite electric field intensity and red shift of the coupled plasmonic resonance. It was found that the classical model fails when d approaches the Fermi wavelength λ_F and quantum effects become relevant, i.e. non-local screening and electron tunneling (Fig. 5.1(c)). This regime was subject of extensive investigation during the past years both

experimentally and theoretically [32, 174–180]. The red-shifting dipole plasmon resonance progressively disappears with decreasing gap distance, while spectrally distinct blue-shifted charge transfer plasmon modes emerge [179]. The plasmonic response can be modeled by introducing an effective dielectric constant in the gap that includes the distance dependent conductivity, thereby accounting for tunneling charge transfer.

5.1.2 Tip-Enhanced Optical Spectroscopy

The interaction of light with metallic scanning probes provides the possibility to realize optical spectroscopy with high spatial resolution in a controlled environment below the diffraction limit. Local optical amplification in an Atomic Force Microscopy (AFM) setup from metal coated fibers has been used to spatially confine incoming light and enhance radiated light, guided through a fiber, as in scanning near-field optical microscopy or with metallic or metal coated silicon tips that couple the near-field with external far-field excitation and detection schemes as in apertureless Scanning Near-Field Optical Microscopy (SNOM) [181–183]. These techniques have been demonstrated to provide broadband enhancement with spatial resolution down to ∼20 nm [184, 185]. The STM can readily provide atomically resolved surface topography and electronic structure, while the tip may focus an electromagnetic field to a nanometer region or enhance locally emitted radiation to the far-field which holds the potential for combination and simultaneous characterization of neutral and charged excitations in solid state systems. Powerful surface science techniques have been developed, based on this combination which are highlighted in the following.
Tip-enhanced Raman spectroscopy (TERS) exploits optical near-field excitation to probe vibrational information via enhanced Raman scattering, analogous to the SERS mechanism, as discussed in section 2.3.4. The technique was pioneered by using metal-coated AFM and solid metallic STM tips to overcome the limitations in SERS, which stem from limited control of the nanostructure geometry and the achievable spatial resolution [83, 186–189]. Single-molecule TERS was achieved in vacuum environment with controlled sample surface morphology and even sub-molecular resolution was recently achieved by using a UHV low-temperature STM with high light collection efficiency and spectral matching of the plasmonic nanocavity resonance with the molecule Stokes emission [190–192]. These achievements have pushed the technique to a point, where vibrational recognition approaches the spatial resolution of STM imaging to provide chemical and electronic information on a sub-nanometer level, with application in catalysis, nanotechnology and biotechnology [191].
STM-induced luminescence is based on electroluminescence from an electronic sample excitation, induced by the voltage driven tunneling current which is collected with a far-field optical read-out. The current between an STM tip and sample can induce luminescence from the junction via inelastic electron tunneling or electron-hole pair excitation with subsequent radiative emission, efficiently coupled to the far-field by tip plasmonic modes, which are enhanced in the cavity. First observations of light emission from metal-insulator-metal junctions have quickly sparked interest after the invention of STM to collect light from the tunneling junction with high spatial resolution, initially demonstrated on polycrystalline metal surfaces and semiconductors [193–196]. Voltage independent maxima observed in emission spectra were attributed to resonant excitation and radiative decay of plasmonic modes which exist in the formed nanocavity, consisting of coinage metal single-crystal surfaces [197, 198]. The concept was further extended to study systems with well defined

electronic states which exhibit fluorescence upon electron attachment. Emitted fluorescence can couple to the plasmonic field and allow for efficient far-field conversion, thus enabling highly localized spectroscopy which was demonstrated for metal nanoparticles, semiconductors, heterostructures, quantum dots and molecules, down to the sub-molecular regime [199–204]. The combination of STM-induced luminescence together with imaging and tunneling spectroscopy provides a powerful tool set to study fundamental excitations in nanoscale objects.
The combination of STM with ultrashort optical pulses has also led to the development of techniques that provide time resolution down to picoseconds or even femtoseconds. In shaken-pulse-pair-excited-STM, pump and delayed probe light pulses excite a delay dependent tunneling current which provides information on dynamics in the picosecond regime [205]. The employment of terahertz radiation may even provide sub-picosecond time resolution which was demonstrated by opening up an otherwise forbidden tunneling channel with terahertz gating through an electronically isolated pentacene molecule in a time window, shorter than the light wave oscillation cycle [206]. However, general applicability of this concept in surface science is yet to be demonstrated. The lightning rod effect of the tip is expected here to enhance the local field which is not much investigated as it works in a non-resonant fashion, with plasmonic excitations spectrally far beyond reach.
Light excitation or detection has added complementary information which may be acquired by STM with similar high spatial resolution, due to the local confinement of electromagnetic fields in the tip-sample junction. Spectroscopy at fundamental time and length scales has been demonstrated, thereby providing viable tools for future nanoscale science.

5.1.3 Tip-Enhanced Photochemistry

Surface plasmon mediated reactions on metallic nanoparticles are introduced in section 2.3.4. The plasmonic excitation on noble metal surfaces can decay non-radiatively into electron-hole pair excitations which may scatter into an excited adsorbate state and trigger chemistry via vibrational relaxation to the reaction coordinate [10].
This principle was successfully transferred to scanning probe experiments, where a plasmon driven reaction can be directly monitored in the tip-sample junction. Analogous to SERS studies of photochemistry, AFM based high-vacuum TERS was used to reveal the plasmon driven reduced dimerization of 4-Nitrobenzenethiol (4NBT) to p,p'-dimercaptoazobisbenzene (DMAB) on Au nanoplate with a glass support and a Ag coated tip [207]. The same reaction was monitored in an STM based system, where the unidirectional conversion could be controlled by laser power [208]. It was observed that DMAB vibrational mode intensity shows positive correlation with laser power, while 4NBT vibration modes start disappearing. Further studies have revealed the plasmon mediated oxidized reaction of Aminothiophenol (ATP) to DMAB, which shows that DMAB cannot only be catalyzed by reduced but also oxidized reaction [209–212]. These studies are sensitive on the scale of near-field confinement under the tip, while molecules are adsorbed as self-assembled monolayers on the substrate. Therefore, the resolution may reach several nanometer, thus collecting signal from an ensemble of molecules. The STM based TERS study shows reversible isomerization within a single molecule of the azobenzene derivative [4-(phenylazo)phenoxy]hexane-1-thiol (ABT) which is anchored by a thiol-terminated alkyl chain to the Ag STM tip [213]. Observation of telegraph noise between vibrational spectra of two structural isomers demonstrated single molecule detection.

Near-field enhanced single molecule photochemistry in a controlled UHV low-temperature STM environment introduces the possibility to directly couple light into the tip-sample junction, where locally excited photoreactions are monitored by the tunneling current through an observable change in molecular confirmation or electronic structure. The resulting intense electric field in the junction can either directly couple to the transition dipole moment of a molecule to induce a reaction or indirectly induce the reaction via photoexcitation of charge carriers in the metal leads with susequent attachment to the molecule. The former mechanism was very recently demonstrated level by coupling wavelength tunable laser excitation into an STM junction to cleave the S-S bond a single dimethyl disulfide molecule. The reaction mechanism was rationalized by an intramolecular transition from the nonbonding lone pair–type orbitals on the S atoms to the antibonding orbital localized at the S-S bond which is enhanced within the near-field [214].
The plasmon enhanced indirect (substrate-mediated) excitation was not yet demonstrated on a single-molecule. However, it was shown that photogenerated tunneling current transiently charges an electronically decoupled magnesium porphine molecule on an oxidized NiAl(110) surface with energies up to the photon energy [215]. In the tunneling regime, photo-induced resonant tunneling further confined the excitation to the spatial resolution of the STM [216, 217]. The reversible conformational transition of a single molecule was later demonstrated in a pyrrolidine molecule on Cu(001), which was excited by femtosecond laser radiation [218]. It was found that the reaction rate consists of a delay independent, constant incoherent rate and a delay dependent, sinusoidal oscillation of the rate. The oscillation frequency was found to match molecular vibration frequencies which may couple to the reaction coordinate.
Most performed experiments employ photogenerated current in the STM junction for molecule charging and confirmational changes, however, the nature of the excitation mechanism remains unclear, whereby an effect of the near-field is implied but not explicitly demonstrated. The combination of spectrally variable laser excitation with STM holds the potential to study photo-induced reactions and explore plasmonic coupling in a wide parameter space, where not only the properties of the nano-cavity may be altered by precise control of the tip-sample distance but also the excitation can be tuned to match molecular or plasmonic resonances.

5.2 Tip-Enhanced Tautomerization on Cu(111)

The near-field enhanced photoexcited tautomerization of porphycene on a Cu(111) surface was observed in an STM junction. Lateral and vertical spatial confinement as well as spectral variation of the photochemical enhancement are investigated with different tip materials. The results are discussed with regard to mechanistic insight of photochemical enhancement in sub-nanometer junctions by optical near-field excitation in the classical and tunneling regime.

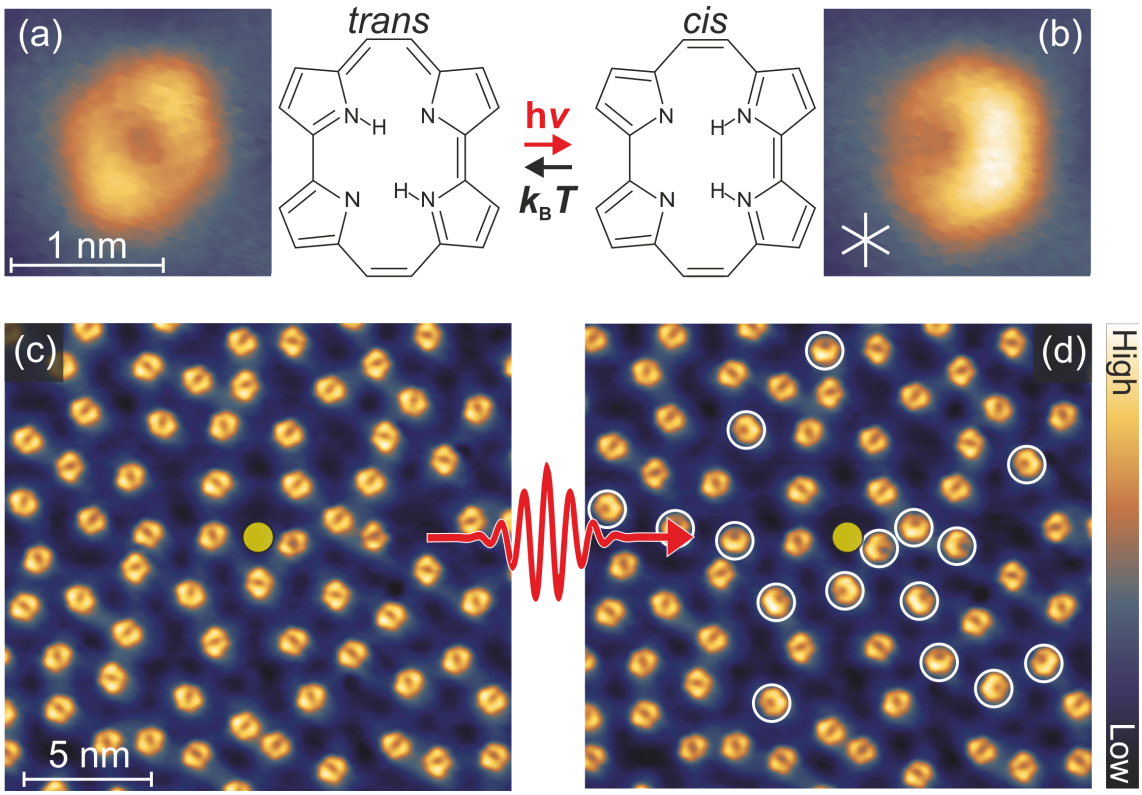

Figure 5.2: STM images of a single porphycene molecule in the (a) *trans* and (b) *cis* configuration on Cu(111) at 5 K (size: 1.75×1.75 nm^2, V_t = 100 mV, I_t = 100 pA). The chemical structures are displayed next to the image. (c) STM image (size: 25×25 nm^2, V_t = 50 mV, I_t = 30 pA) before illumination. The Au tip is located at the center of the image (indicated by yellow circle). (d) Same area after illumination at 720 nm wavelength with $n_{ph} = 2.9(\pm 0.2) \times 10^{17}$ cm^{-2}. Converted molecules to the *cis* configuration are marked by white circles.

5.2.1 Localized Enhancement of Unidirectional Tautomerization in an STM Junction

A porphycene covered Cu(111) surface is prepared, analogous to the procedure, described in section 4.4. All molecules adsorb in the thermodynamically stable *trans* state (Fig. 5.2(a)) and may be unidirectionally converted to the metastable *cis* state (Fig. 5.2(b)) upon photoexcitation. The backward *cis* → *trans* conversion is selectively induced by heating the surface above ∼35 K (see Fig. 4.7). In contrast to the experimental procedure, described in section 4.4, the STM tip is kept in tunneling during illumination and not retracted from the surface. The employed tip is prepared by electrochemical etching of a Au wire (see section 3.4). Fig. 5.2(c) shows an STM image of the prepared surface, where all molecules are found in their *trans* form. The tip is positioned at the image center in tunneling (V_t = 50 mV, I_t = 30 pA) while the surface is illuminated with a photon fluence of $n_{ph} = 2.9(\pm 0.2) \times 10^{17}$ cm^{-2} at 720 nm wavelength at an incident beam angle of 65° from the surface normal and polarized along the tip axis (p-polarized) (see section 3.5). The bias voltage is kept well below the threshold for tunneling electron-induced tautomerization of ∼150 mV (Fig. 4.7). Thermal expansion of both tip and sample is limited by

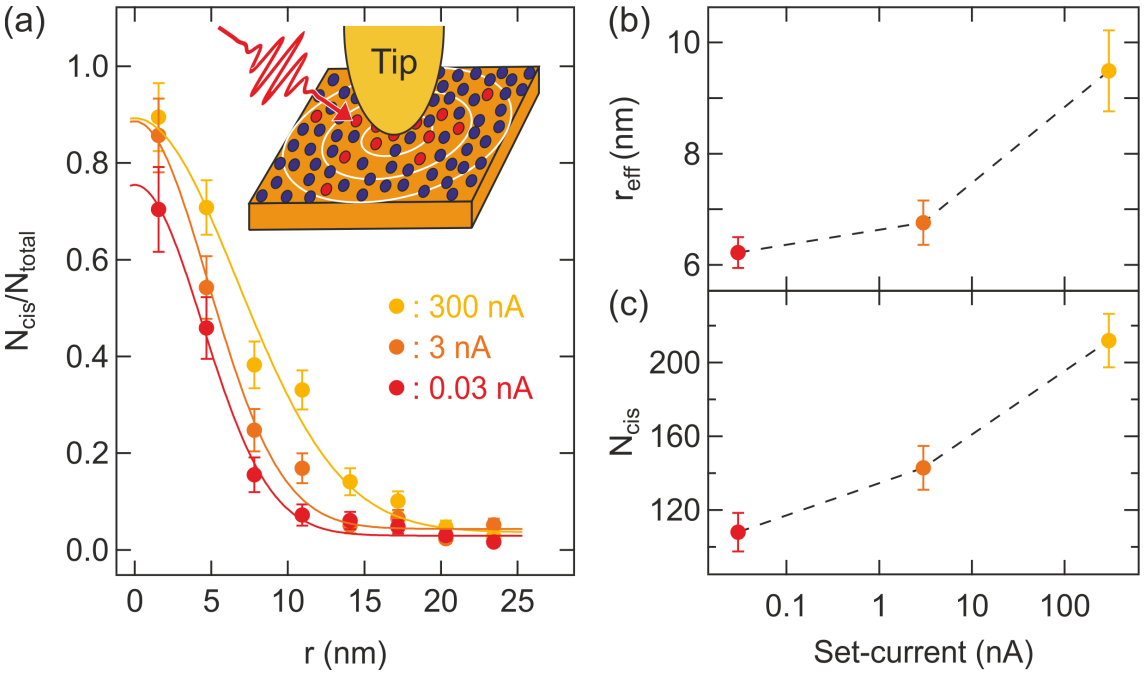

Figure 5.3: (a) Radial distribution of the *trans* → *cis* conversion probability measured at three different tip-surface distances, determined by the STM set-point (V_t = 50 mV, I_t specified in the figure). Solid curves represent a Gaussian fit ($A\ exp\left(-r^2/2\sigma^2\right)$, where $\sigma = r_{eff}$). Inset shows sketch of the experiment, where the proportion of *cis* molecules (red spots) to *trans* molecules (blue spots) is evaluated in incremental distances from the tip position (white circles). Set-current (tip height) dependence of (b) r_{eff}, determined from the Gaussian fit and (c) the total number of reacted molecules N_{cis} (dashed lines represent guide to the eye).

employing a low photon flux which allows for compensation by the STM feedback loop to maintain a constant tip-sample distance, while the measured sample temperature was raised from 5.2 K to 6-7 K upon irradiation, depending on the incident wavelength. This temperature is insufficient to thermally induce the *cis* → *trans* backward reaction which is therefore negligible in the photoinduced process. After surface irradiation, we observe that the photoexcited *trans* → *cis* conversion is locally enhanced in proximity of the STM tip position, where a significantly larger proportion of molecules are reacted, compared to the molecule population further distant on the surface. The enhancement may be illustrated by mapping the radial distribution of the tautomerization probability from the central tip position (see inset in Fig. 5.3(a)). Fig. 5.3(a) displays the proportion of reacted molecules from repeated measurements as function of the radial distance in incremental steps of about 3.1 nm and the STM set-current. The relative tip height displacement from variation of the set-current corresponds to ∼4 Å, assuming a tunneling current decay constant of ∼11 nm^{-1} [219]. Gaussian fits to the radial decay of the tautomerization probability reveal a strong enhancement in the tip vicinity with an effective radius r_{eff} within ∼10 nm, in agreement with the expected lateral near-field localization in an STM junction [220–223]. Effective radius and number of total reacted molecules N_{cis} are found to increase significantly with decreasing tip-surface gap distance (Fig. 5.3(b),(c)), thus suggesting an inverse dependence on gap size. However, the observed tip-enhanced spot cannot be regarded

equivalent to the optical near-field in the junction as it is determined from a convoluted process with the photoexcited tautomerization in porphycene. It should be noted that the enhanced photoreaction still follows a first-order rate law (see Eq. 4.2), as discussed in the following, where the cross section is modulated via optical near-field enhancement in the STM junction. This has important implications regarding the discussion of spatial field enhancement variation in atomically terminated junctions, where strong sub-nanometer near-field confinement is proposed to occur [224, 225]. Such drastic local changes, however, are not observed, as we find good agreement with radial decay, expected in a simple cone-flat geometry without atomic protrusions [226, 227]. We may rationalize the absence of sub-nanometer confinement in tautomerization probability by the exponential saturation to the *cis* state of the anyhow very small number of molecules in this area, given by Eq. 4.2. Furthermore, the radial decay is discussed at a resolution of about 3.1 nm in order to probe a statistically relevant number of molecules, which is why the found results are not suitable for the discussion of sub-nanometer laterally confined near-fields.

5.2.2 Spectral and Tip Material Dependent Near-Field Generation

The qualitative finding of enhanced *trans* $\rightarrow$ *cis* conversion in a nanometer confined area underneath the STM tip is quantified by evaluation of the cross section in presence and absence of a metallic tip during photoexcitation, hence with and without optical near-field excitation. The cross section $\sigma_{t\rightarrow c}$, measured in the tip presence and absence is further referred to as σ_{NF} and σ_{FF}, respectively. In section 4.5, the full spectrum of σ_{FF} in the UV to near-IR is shown and the photoexcitation origin is denoted to a dominant contribution of substrate-mediated charge carrier generation, which follows the polarization dependent substrate absorption.

The near-field enhanced cross section, on the other hand, was evaluated by scanning the surface (60×60 nm^2) with a Au tip in constant current mode during irradiation (schematically depicted in left cartoon of Fig. 5.4). This procedure ensures that a statistically sufficient number of molecules ($\sim$600 molecules) is subjected to the spatially confined near-field in the tip-sample junction to reliably determine σ_{NF}. Fig. 5.4 shows the evolution of converted *cis* molecules as function of photon fluence at 720 nm excitation wavelength both with near-field enhancement and without, further referred to as far-field excitation. The evolution is fit with a first-order rate equation (see Eq. 4.2), both for near- and far-field excitation. At 720 nm we find $\sigma_{NF} = 5.59(\pm0.35)\times10^{-19}$ cm^2 and $\sigma_{FF} = 7.27(\pm0.18)\times10^{-21}$ cm^2, thus revealing a strong photochemical enhancement through near-field excitation in the STM junction (employed tip Au#1 in Fig. 5.5). Fig. 5.5 depicts the near-field enhanced tautomerization cross section, measured across the entire accessible spectral excitation range, while the material dependent enhancement was explored by employing different STM tip materials, i.e. W, PtIr(80:20) and two Au tips. Far-field excited cross sections are also shown for comparison (identical to p-polarized cross section in Fig. 4.12(a)). The process obeys first-order dynamics across the investigated range. It was found that photoinduced tautomerization may be largely enhanced via near-field excitation below $\sim$2.2 eV excitation energy by Au tips and the PtIr tip, while this effect is not observed for the W tip. The enhancement is attributed to strong localization of the electromagnetic field in the tunneling junction, which may stem from excitation of an LSPR in the nano-gap and the lightning rod effect [226, 228]. As the tip structure was not controlled in this experiment,

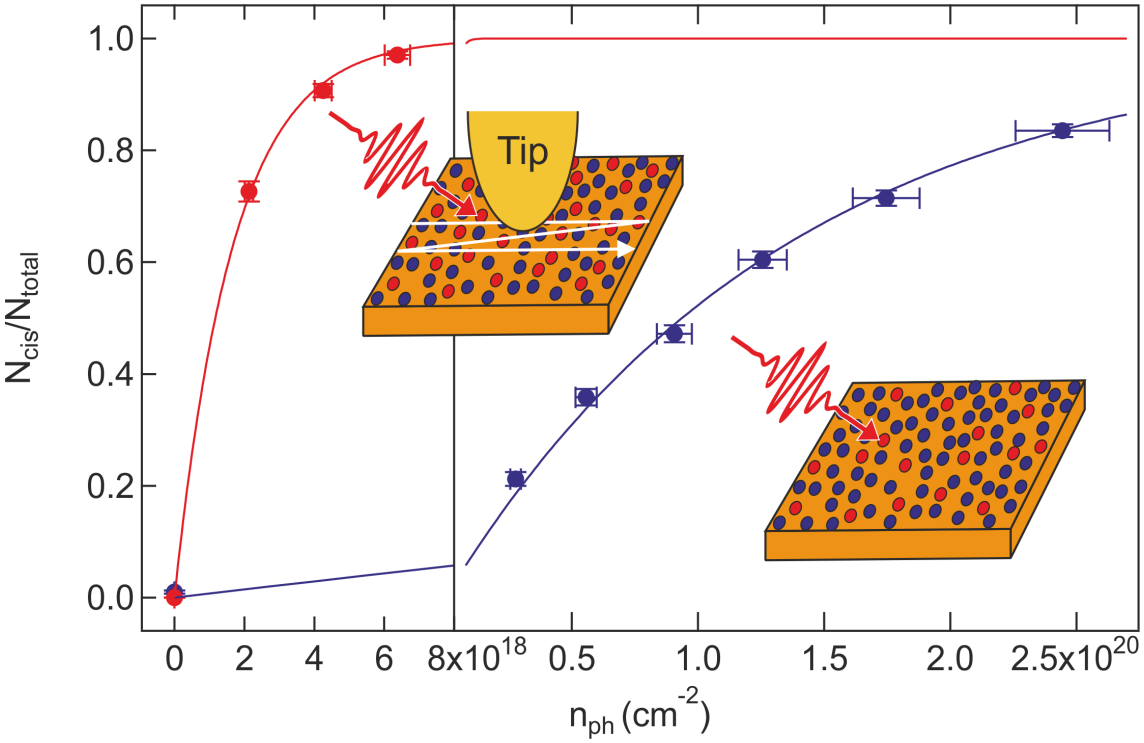

Figure 5.4: Fraction of *trans* → *cis* reacted molecules under 720 nm wavelength excitation as function of photon fluence, measured both in presence (red) and absence (blue) of a Au tip, scanning across the surface (60×60 nm^2, 580 molecules, V_t = 50 mV, I_t = 30 pA). The solid curves represent a fit to the data, according to a first-order rate law (see Eq. 4.2). The cartoons sketch the experimental procedures in presence (left) and absence (right) of the tip. Converted *cis* molecules are depicted red, *trans* molecules blue.

the detailed enhancement origin was not identified here but subject of section 5.3. Albeit the limitations in geometrical control, a distinct spectral structure is observed for different Au tips. Thereby, the origin of spectral variation is attributed to the geometry dependent enhancement, while a resonant excitation of the molecule transition dipole is excluded to cause resonant structure, as this may be regarded as tip independent, with limited geometrical influence on the coupling [229]. The enhancement dependence on tip material is explained by the plasmonic properties of the individual materials, as gold and copper can support localized plasmon resonances at energies below ∼2.2 eV, while tungsten may not support a plasmonic resonance in the investigated spectral range [30]. Interband transitions between d- and sp-band in the metal quench the excitation of a plasmonic resonance which is observed in Fig. 4.12(a) by a sharp drop of the near-field cross section. D-band transitions are excited at about 2 eV in copper and gold, while the d-band in tungsten crosses the Fermi energy, which prohibits an efficient plasmon excitation, as electromagnetic energy is directly absorbed by electron-hole pair excitations. PtIr on the other hand also exhibits high lying d-bands but we still observe a considerable enhancement, which is speculated to stem from coating of the tip apex by substrate metal in the tip formation process, thus changing the electronic structure at the apex from repeated tip-forming. Since this tip was in use for years, the apex structure is believed to be heavily modified, while all other tips were freshly prepared and only mildly prepared *in-situ* by application

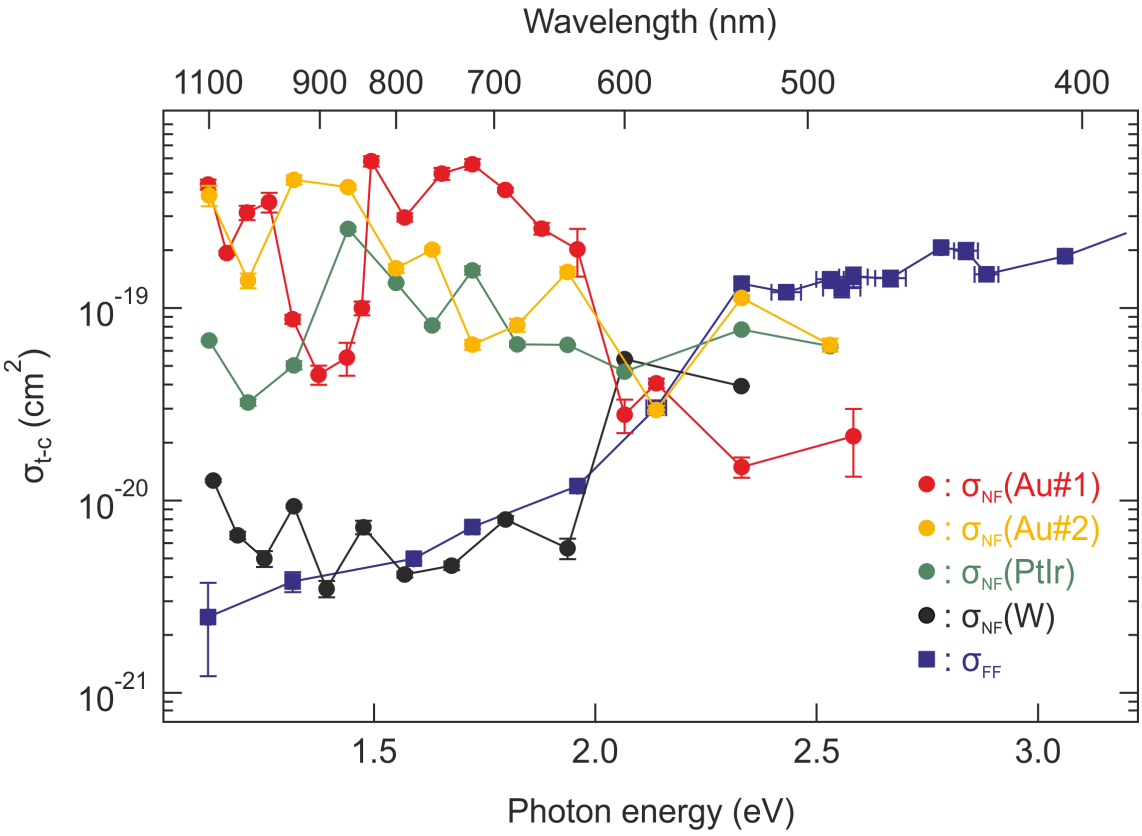

Figure 5.5: Photoexcitation energy (wavelength) cross section dependence for near-field excitation for two different Au tips (Au#1: red filled circles, Au#2: orange filled circles), a PtIr tip (green filled circles) and a W tip (black filled circles) in comparison to the far-field cross section (blue filled squares). All near-field data was obtained by scanning 60×60 nm^2 in constant current mode at V_t = 50 mV, I_t = 30 pA.

of voltage pulses and controlled surface indentation.

In order to identify the photochemical enhancement from the experimental results, σ_{NF} should be directly comparable to σ_{FF}. However, we note that σ_{NF} is significantly underestimated in the spectral range, where enhancement is observed as the tip is scanned across the surface scan area ($A_{scan} = 60 \times 60 nm^2$) during photoexcitation, which is necessary for statistical relevance of the data but leads to an apparent reduction of the actual near-field cross section. The effectively enhanced radius r_{eff} underneath the tip was estimated for tip Au#1 from Fig. 5.3 as 6.2(± 0.3) nm. Analogous to this precedure, r_{eff} was determined for tips Au#2, PtIr and W as 7.0(± 0.3) nm, 9.7(± 1.8) nm and 4.6(± 0.3) nm, respectively (Fig. 5.6(a),(b),(c)). Therefore, σ_{NF} is corrected by a geometrical factor to estimate the near-field enhanced cross section underneath the tip:

$$\sigma_{NF,corr} \approx \left(\frac{A_{scan} + 2\sqrt{\pi A_{scan}} r_{eff} + \pi r_{eff}^2}{\pi r_{eff}^2} \right)^{1-\frac{\sigma_{FF}}{\sigma_{NF}}} \cdot \sigma_{NF} \tag{5.7}$$

The exponent accounts for relative contributions to σ_{NF} from near-field and far-field excitation. Above ~2.2 eV, σ_{NF} drops below σ_{FF}, which is explained by reflection and scattering from the tip, thus blocking the incident electromagnetic field from the investigated

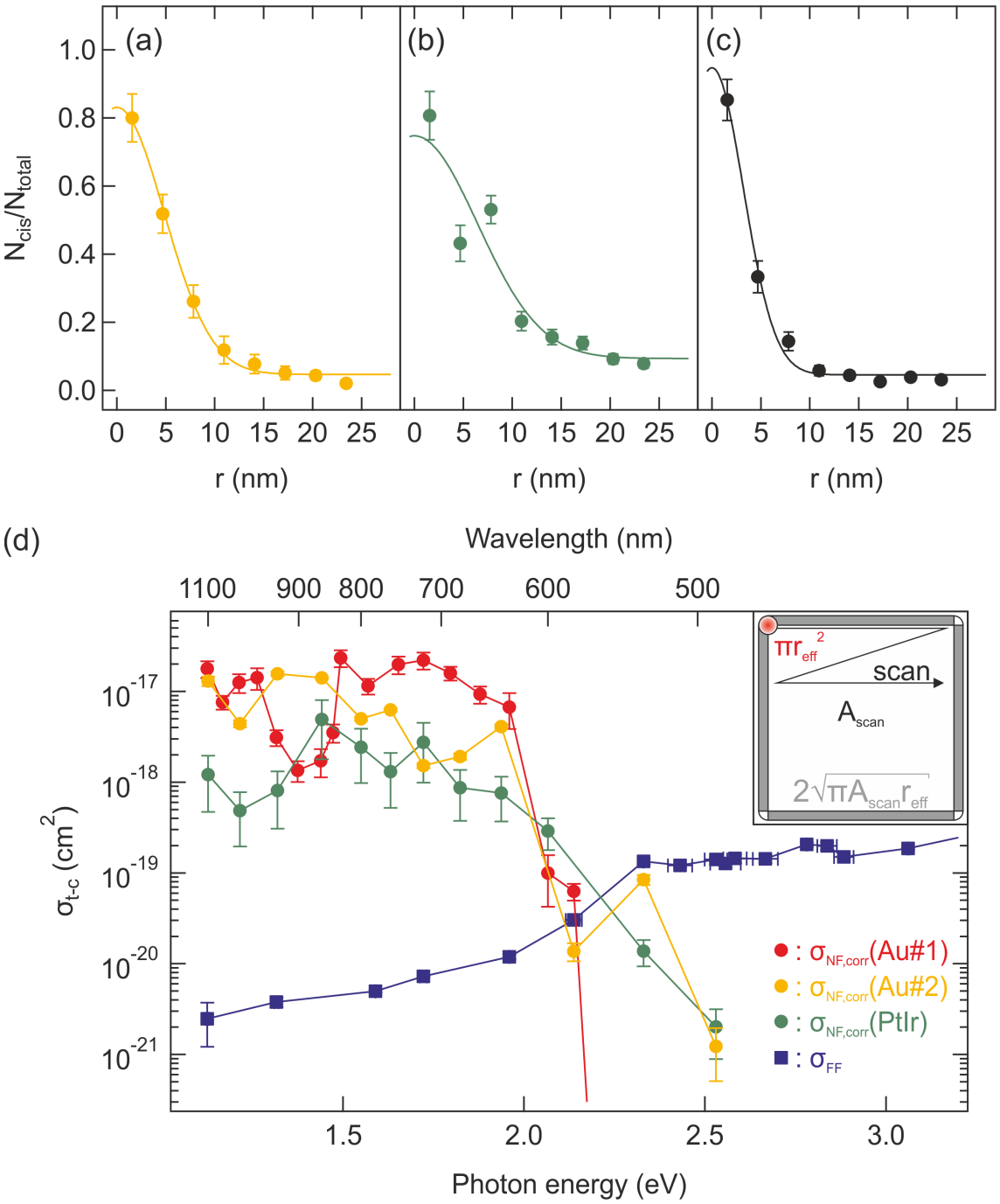

Figure 5.6: Radial distribution of the *trans* → *cis* conversion probability with Gaussian fits (solid curves) for STM tips (a) Au#2 at 860 nm (n_{ph} = 3.5(±0.2) × 10^{17} cm^{-2}) (b) PtIr at 860 nm (n_{ph} = 4.9(±0.3) × 10^{17} cm^{-2}) (b) W at 690 nm (n_{ph} = 2.5(±0.2) × 10^{18} cm^{-2}) (V_t = 50 mV, I_t=30 pA). (d) Photoexcitation energy (wavelength) dependent near-field cross section for tips Au#1 (red filled circles), Au#2 (orange filled circles), PtIr (green filled circles) and far-field cross section (blue filled squares). Near-field cross section corrected by Eq. 5.7.

area, while near-field photoexcitation below ∼2.2 eV largely exceeds far-field contribution. Nominator and denominator describe the area, scanned by the tip-enhanced spot during the experiment and the spot size itself, respectively (inset in Fig. 5.6(d)). Fig. 5.6(d) displays the spectral dependence of $\sigma_{NF,corr}$ together with σ_{FF} for all tip materials. W was excluded from the correction, as no apparent enhancement was observed. The spectrally varying photochemical enhancement factor ($\sigma_{NF,corr}/\sigma_{FF}$) reaches ∼$10^2$-$10^3$ in the STM junction. This finding provides the first direct measurement of a photochemical enhancement factor for individual molecules in a single nano-gap across a broad excitation range, which is inaccessible in ensemble averaged measurements.

5.2.3 Mechanism of Near-Field Mediated Porphycene Tautomerization

Photoexcited tautomerization of porpyhcene with in the far-field was elucidated to be driven by charge carriers which are generated in the substrate and subsequent attachment to the adsorbate. Spectral scans of the excitation energy dependent cross section, both with far- and near-field excitation, show no indication of a molecule dipole transition to obviously contribute to the photoreaction. We thereby denote the near-field enhanced reaction also to an indirect excitation mechanism, where both charge carriers in the substrate and in the tip may contribute via inelastic tunneling. However, the exact properties of the near-field, generated in the junction, should determine the intensity and relative strength of the individual processes. A fundamentally important parameter is the relative tip-sample distance, which is a dominant parameter to control plasmonic resonance energy as well as magnitude of the near-field. It was revealed in theoretical and experimental studies that near-field properties are affected, when the gap size enters the tunneling regime and classical electrodynamics fail to describe the physics, while this is the inherent working range of the STM [32, 174–180, 230, 231]. Near-field mediated chemistry in this transition regime can therefore be precisely probed in the STM junction, which has not been examined yet.

Fig. 5.7(a) shows the tip-surface gap dependent cross section at different excitation wavelengths with tip Au#1, where the gap size is controlled by the set current. At 720 nm excitation, the tip shows strong enhancement, while none was observed at 532 nm (see Fig. 5.5), which is reflected in the gap size dependence. We find that the near-field mediated cross section increases monotonously in the tunneling regime, while there is a negligible effect when the near-field may not be excited. The expected near-field decay in the quantum regime, where electron tunneling is dominant, is not reflected in the reaction cross section, which may be explained by overcompensation from optically excited tunneling (Fig. 5.7(b)). It should further be mentioned that the interaction between near-field and molecule scales differently from net field enhancement and could increase continuously in the tunneling regime, which was observed before for Raman excitation in a TERS setup [180, 191]. Photoexcited tunneling carriers can also induce the reaction non-locally, as it was found that porphycene tautomerization on Cu(111) can be driven by tunneling electrons, traveling along the surface state [161].

Fig. 5.7(c) depicts the gap dependent cross section, measured outside the tunneling regime at 860 nm excitation wavelength with tip Au#2, where this tip shows strong enhancement. The data was measured with the tip scanning the surface during illumination and disabled feedback loop, while the tip is vertically retracted from the set point (V_t = 50 mV, I_t=30

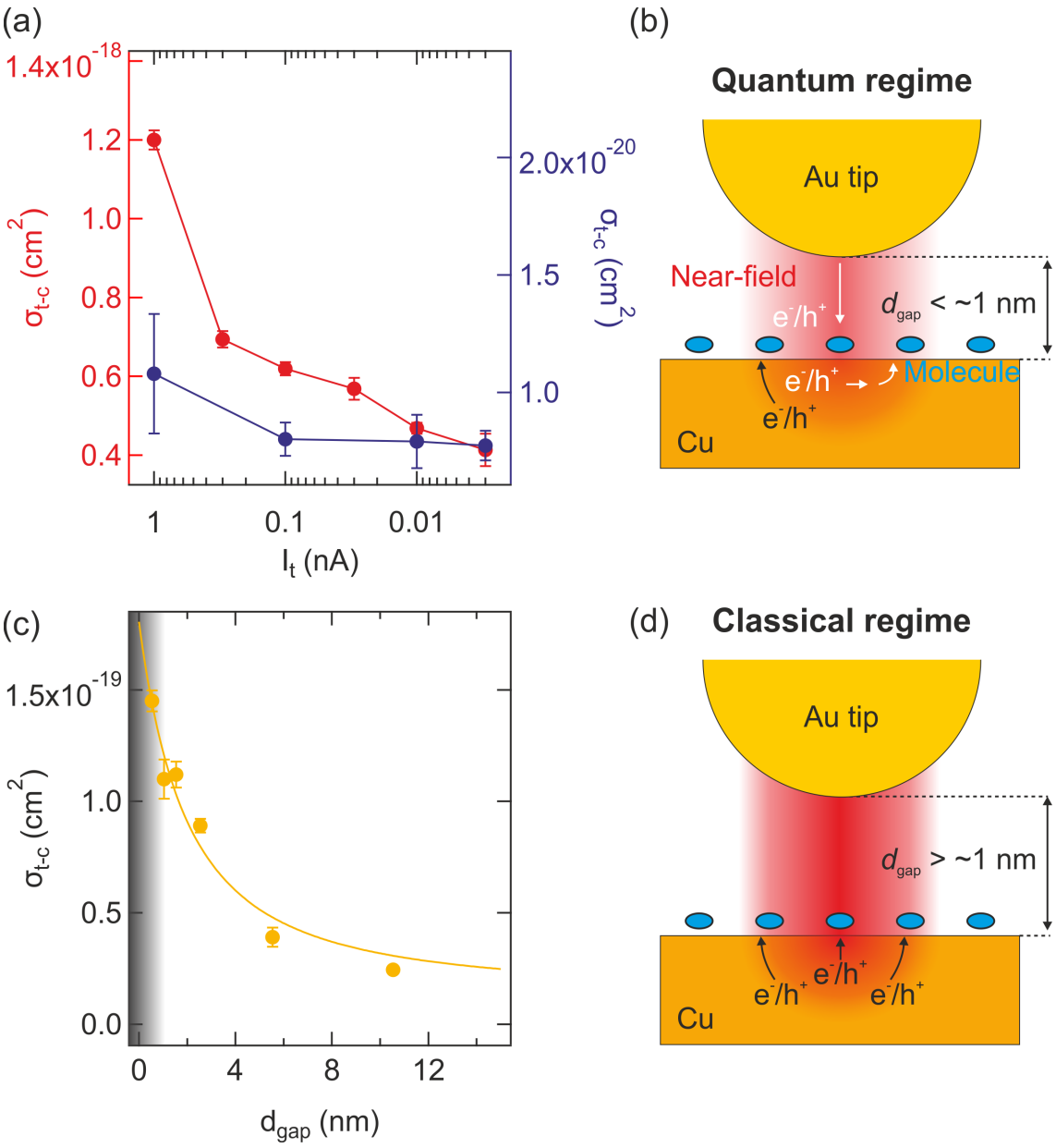

Figure 5.7: (a) Tip-surface distance-dependent cross section in the tunneling regime at 720 nm (red filled circles) and 532 (blue filled circles) excitation wavelength, measured with tip Au#1. I_t is the STM set current. (b) Schematic representation of the proposed excitation mechanism in the quantum regime. (c) Tip-surface distance(d_{gap})-dependent cross section outside the tunneling regime (black shaded area) at 860 nm excitation wavelength, measured with tip Au#2. The first left data point is taken at d_{gap}, corresponding to V_t = 50 mV, I_t=30 pA, from where the tip is vertically retracted and scanned across the surface under illumination with disabled feedback loop. (60×60 nm^2, ~670 molecules). Reacted molecules were identified from subsequent imaging. Low photon flux of 3.9(±0.3)-9.6(±0.6)×10^{15} cm^{-2}s^{-1} was used to minimize thermal expansion. The solid line represents a fit to Eq. 5.8. (d) Schematic representation of the proposed excitation mechanism in the classical regime, i.e. no electron tunneling.

pA). As optically excited tunneling electrons cannot mitigate the near-field but also not contribute to the reaction, the cross section should reflect the excitation rate of substrate charge carriers. In a simple classical coupled dipole approximation, the distance-dependent excitation rate can be described by mutual polarization of tip and sample, where the tip is represented by a sphere of radius R with polarizability α, as descriebd in Eq. 5.2. The measured near-field cross section is then proportional to the excitation rate [180]:

$$\sigma_{NF} \propto \sigma_{FF} + \left(1 - \frac{\kappa\alpha(\epsilon_{Cu} - 1)}{16\pi(\epsilon_{Cu} + 1)(R + d_{gap})^3}\right)^{-2} \tag{5.8}$$

where κ is a free parameter, which accounts for possible deviation of the tip apex from an ideal spherical shape, d_{gap} is the tip-sample gap distance and ϵ_{Cu}, ϵ_{Au} are the wavelength dependent dielectric constant of copper and gold, respectively, taken from ref. [30]. We find good agreement of σ_{NF} scaling with gap size, represented by the solid curve in Fig. 5.7(c), which is the best fit result, achieved for $\kappa = 2.6(\pm 0.1)$ and R=41($\pm$8) nm. The charge carrier excitation in the substrate is therefore concluded to follow the near-field intensity, which results from classical coupling of the tip apex dipole with its image dipole (Fig. 5.7(d)).
The results suggest that near-field mediated porphycene tautomerization is dominated by photoexcited charge carrier generation in the substrate which is locally enhanced via plasmon decay in the junction. Optically excited inelastic tunneling may contribute to the process at sub-nanometer distance, where tunneling is significant. Since the tip needs to be scanned across the surface in the here presented measurement scheme, it is not the ideal framework to discuss detailed variations of plasmonic enhancement in the tunneling junction which is presented in the following.

5.2.4 Conclusion

Near-field mediated *trans* $\rightarrow$ *cis* tautomerization of porphycene on Cu(111) was directly observed by low-temperature STM with wavelength tunable laser excitation. We found that the photoreaction is significantly enhanced in the red and near-IR range by employing gold as tip material, whereas the enhancement was found to be weak for tungsten, thus the enhancement is denoted to a coupled plasmonic excitation of the tip-sample junction. The reaction enhancement factor of near-field to far-field photoexcitation reaches $\sim 10^2$-10^3, which represents, to the best of our knowledge, the first measurement of an enhancement factor for single molecules in a nano-gap. Near-field induced tautomerization was examined in and out of the tunneling regime. It was found that the reaction is driven by photogenerated substrate charge carriers whose excitation rate is locally enhanced via plasmonic decay in the STM junction. Optically excited inelastic tunneling between tip and surface may contribute to the process in the tunneling regime. The presented work demonstrates a new possibility to study directly near-field enhanced chemistry at the single-molecule level in a nanoscopic gap with precise gap distance control. Our results should provide fundamental insight into photochemistry and -catalysis on metallic nanostructures, which is dominated by near-field enhanced reactions within nano-gaps [10, 12, 13, 232].
Chapter 4 outlined the possibility to use tautomerism for photoresponsive single-molecule switching in molecular scale electronics. The simultaneous implementation of plasmonic elements, which may confine optical signals beyond the diffraction limit and near-field re-

sponsive molecular functional components holds the potential for combination in an all optical operation scheme [94].

5.3 Tip-Enhanced Tautomerization on Cu(110)

The following section will focus on the plasmon mediated reversible tautomerization of a single porphycene molecule on the Cu(110) surface to locally probe the near-field properties within the STM junction. A brief overview summarizes previous work of tunneling electron and thermally induced porphycene tautomerization on the Cu(110) surface, followed by a description of the experimental procedure. The near-field response of STM tips with tailored geometry is further presented and the mechanism of photogenerated charge carrier tunneling to induce the reaction is elucidated.

5.3.1 Porphycene Tautomerization on Cu(110)

On the Cu(110) surface, porphycene adsorbs as isolated molecules in the *cis* state which is confirmed by comparing the molecular appearance in STM images (Fig. 5.8(a)) with the calculated structure on the surface (Fig. 5.8(b)) The molecule exhibits one axis symmetric protrusion and aligns on the substrate with the symmetry axis along the surface high symmetry [1$\bar{1}$0]-direction. The assignment to the *cis* tautomer is in agreement with calculated total energies of the tautomers in DFT calculations (Fig. 4.5). The molecule appears in two mirror symmetric *cis* states on the surface which are energetically degenerate (Fig. 5.8(c),(d)) while the *trans* state is not observed within the temporal resolution of STM measurements. Thermal and tunneling electron excitation drives the porphycene conversion between mirror symmetric *cis* states. As opposed to porphycene on Cu(111), the molecule and the Cu(110) surface show the same symmetry along the [1$\bar{1}$0]-direction. Therefore, the molecule position during *cis* $\leftrightarrow$ *cis* conversion is preserved and the reaction can be directly monitored in the tunneling current trace, due to the local abrupt change in conductance upon reaction (Fig. 5.8(e)). The STM tip position is kept stationary on the molecule (white star in Fig. 5.8(a),(c)) while the *cis* $\leftrightarrow$ *cis* reaction is induced and the reaction rate can be deduced directly from the inverse dwell time, measured in the current trace (Fig. 5.8(f)). Fig. 5.9(a) shows the bias dependent reaction yield of the reversible *cis* $\leftrightarrow$ *cis* conversion. The bias polarity independent reaction threshold is about $\pm$150 meV which indicates that the reaction is also driven via inelastic tunneling electron excitation of molecular skeletal vibrations, similar to the reaction mechanism on Cu(111). Fig. 5.9(b) shows an Arrhenius plot of the temperature dependent tautomerization rate. The *cis* $\leftrightarrow$ *cis* reaction activation energy is determined as E_a = 168($\pm$12) meV, similar to the tunneling electron induced reaction barrier of 150 meV. The tip was kept stationary above the molecule at an applied bias below the threshold for inelastic tunneling electron induced tautomerization. In Fig. 5.9(c), the STM observable conversion of porphycene tautomers by thermal and energetic tunneling electron excitation is summarized. Vibration mediated coupling to the reaction coordinate drives the conversion between the energetically degenerate metastable *cis* tautomers, while the *trans* state may not be observed, as the tautomer energetics are shifted due to substrate interactions. The mechanism of inelastic tunneling electron induced tautomerism was further investigated via isotope substitution

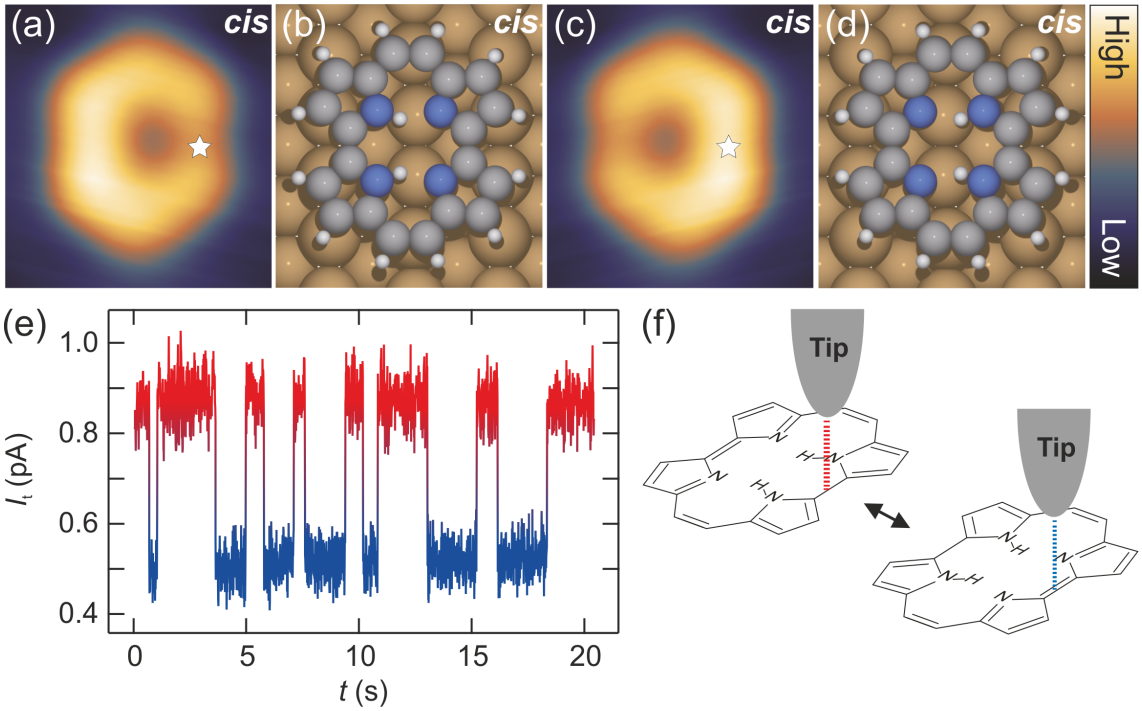

Figure 5.8: (a) STM image and (b) calculated adsorption geometry of a Porphycene molecule adsorbed on Cu(110) in the thermodynamically stable *cis* state. (c) STM image and (d) calculated geometry of the mirror symmetric *cis* state. The two states are energetically degenerate and are equally populated after adsorption. (e) Current trace of the tunneling electron induced *cis* ↔ *cis* conversion, recorded while the tip is fixed over the molecule (white star). The observed telegraph noise indicates two distinguishable conductance state. (V_t = 10 mV, I_t = 0.5 pA) (f) Measurement schematic which indicates the molecular configuration that belongs to the two conductance states. ((a)-(d) adapted by permission from Kumagai *et al.*, Physical Review Letters **2013**, 111, 246101 [104], copyright 2013)

of the cavity H by D atoms, which should strongly modify the tautomerization potential and give insight into H bond dynamics. While the threshold bias voltage is similar for both H-Pc and D-Pc, substantial difference in the behavior is observed above ∼ 250 mV. The fit (blue solid line in Fig. 5.10(a), fit procedure in [233]) of the voltage dependent D-Pc reaction yield between 250-320 mV reveals a second onset at 279(±5) mV which matches the measured N-D stretch mode (ν(N-D)). The stretch mode was determined experimentally to be 284 meV from nonlinear characteristics in the conductance spectrum (dI/dV) measured over a molecule (blue solid line in top left inset of Fig. 5.10(a)). The vibrational density of states of porphycene on Cu(110) was further theoretically accessed in DFT calculations and the stretch mode was located at 278 meV (blue solid line in Fig. 5.10(b)). Both experimental and theoretical results suggest that the onset in the yield stems from a vibrational excitation of the N-D stretch mode by inelastic tunneling electrons. From conductance spectroscopy and DFT calculations, the N-H stretch mode (ν(N-H)) is furthermore found at 380 meV (red solid line in top left inset of Fig. 5.10(a)) and 376 meV (red solid line in Fig. 5.10(b)), respectively, so that a similar onset in the reaction yield is expected for H-Pc at this energy. However, the yield only moderately increases in the observerd bias range

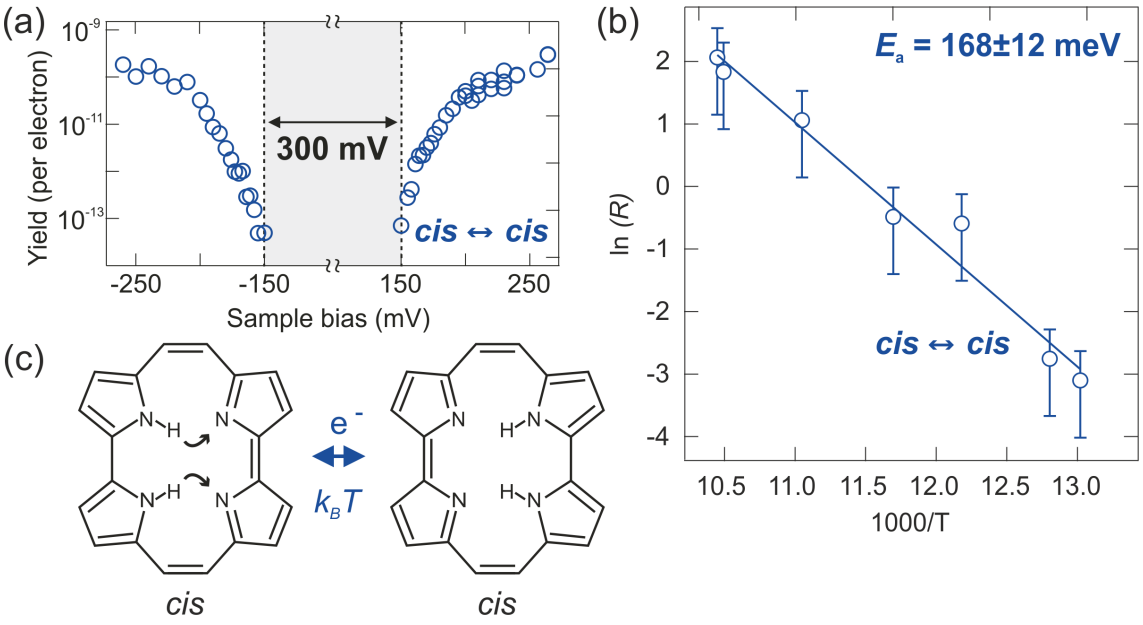

Figure 5.9: (a) STM bias dependence of the tautomerization yield for the *cis* ↔ *cis* conversion. The polarization independent threshold voltage is determined as about ±150 mV. (b) Arrhenius plot of the thermally induced tautomerization rate R, measured at V_t = 50 mV, I_t = 30 pA, far below the in (a) indicated threshold. The activation energy is determined as $E_a = 168 \pm 12meV$. (c) Schematic depiction of the interconversion between the porphycene tautomers on Cu(110). The reversible *cis* ↔ *cis* conversion is induced via both energetic tunneling electrons (e^-) and thermal excitation (k_BT). ((a),(b) adapted by permission from Kumagai *et al.*, Physical Review Letters **2013**, 111, 246101 [104], copyright 2013)

which can be attributed to a more pronounced anharmonicity of the mode potential as a consequence of strong H-bond formation, which is supported by an observed broadening of the N-H stretch mode in the conductance spectrum [147]. The observed common onset in the yield for H- and D-Pc at ∼150 meV cannot directly be pinpointed to a specific vibration mode, since it is located in the skeletal mode energy range and may relate to one or several of the skeletal vibrations which can couple indirectly to the tautomerization coordinate. DFT calculations reveal a high density of modes up to ∼200 meV (Fig. 5.10(b)) and the experimental conductance spectrum shows a common peak at 175 meV (top right inset of Fig. 5.10(a)), which may relate directly to the observed onset threshold. The excitation of skeletal vibration modes has already been shown to open up the reaction channel on Cu(111) and it is therefore reasonable to assume a similar mechanism on the (110) surface [159, 160].

5.3.2 Photoinduced Reversible Single-Molecule Tautomerization

Photoinduced tautomerization on the Cu(110) surface is observed within an isolated individual porphycene molecule which is found on the decorated surface at low coverage in

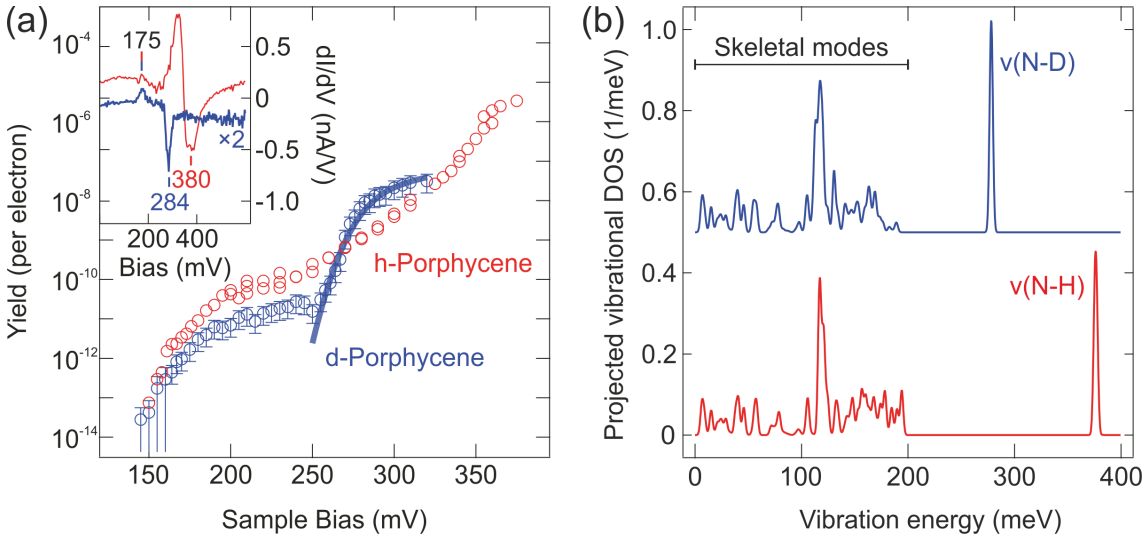

Figure 5.10: (a) STM bias dependence of the tautomerization yield for H-Pc (red circles) and D-Pc (blue circles). The inset shows the dI/dV conductance spectra for the two species (V_t = 100 mV, I_t = 20 nA for H-Pc and I_t = 30 nA for D-Pc) (c) Calculated projected density of states of H- (red) and D-Pc (blue) on a rigid Cu(110) surface. The energetic range of skeletal molecular vibrations are labeled and the inner cavity stretch modes ν(N-D) and ν(N-H) are calculated as 278 and 376 meV, respectively. ((a),(b) adapted by permission from Kumagai *et al.*, Physical Review Letters **2013**, 111, 246101 [104], copyright 2013)

its thermodynamically stable *cis* state. As the *trans* configuration is not observed within the instrument temporal resolution, photoexcited tautomerization occurs solely between the two mirror-symmetric *cis* states in a reversible manner, thus eliminating the need for statistical averaging over a large number of molecules, as it was done for *trans*→*cis* conversion on Cu(111). However, the reversibility imposes the need for constant probing of the tautomeric state during illumination. Therefore, a direct comparison with far-field induced conversion is not possible. Fig. 5.11(a) depicts a schematic of the experimental procedure, where the tip is placed in constant current mode above one lobe of the molecule. Upon illumination, the *cis*↔*cis* conversion is registered as an abrupt vertical tip displacement. Fig. 5.11(b) shows the resulting telegraph noise in the z-piezo feedback during illumination as function of time. Two plateaus indicate when the H atoms are located underneath the tip (Hi state, red) and on the opposite side (Lo state, blue). The assignment is confirmed by STM images (Fig. 5.11(c)). From the recorded time traces, the tautomerization rate is determined:

$$R_{Hi\rightarrow Lo/Lo\rightarrow Hi} = \frac{n}{\sum_i^n \Delta t_i} \tag{5.9}$$

$$\sigma_{sem} = \frac{s}{\sqrt{n}} \tag{5.10}$$

where $R_{Hi\rightarrow Lo}$ and $R_{Lo\rightarrow Hi}$ denote the Hi→Lo and Lo→Hi rate, respectively, n is the number of recorded time intervals Δt_i in the corresponding initial state. The statistical

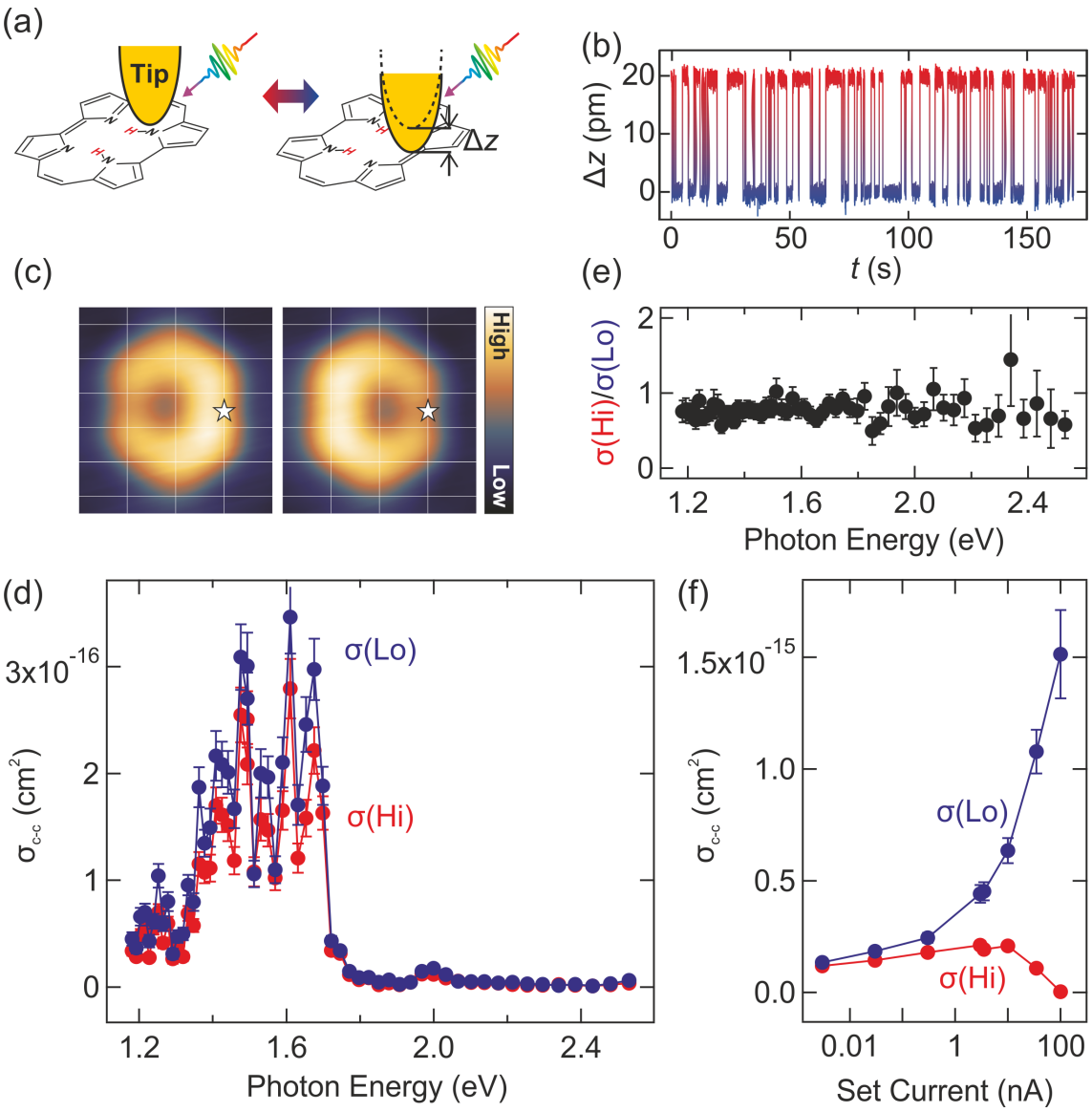

Figure 5.11: (a) Schematic measurement procedure. The tip is placed above the bright lobe of the molecule in constant current mode during illumination. Tautomerization is manifested in a sudden vertical tip displacement. (b) Recorded telegraph noise of the vertical displacement as function of illumination time. Two states are clearly distinguishable, corresponding to the H atom on the tip side (Hi state, red) and opposite to it (Lo state, blue). (c) STM images of a single porphycene molecule before and after a tautomerization event. The tip position is marked by a star. (V_t = 100 mV, I_t = 10 nA) (d) Initial state dependent tautomerization cross section measured as function of incident photon energy. (V_t = 50 mV, I_t = 10 pA) (e) Spectral dependence of cross section shows a constant ratio between both states. (f) STM set current dependent cross section, where the set current is used to control the tip-sample distance.

error is estimated as the standard error of the mean σ_{sem}, which assumes that the estimation of the actual rate from the limited sampling size becomes increasingly accurate with higher n and therefore reduces the sample standard deviation s. The tip presence may deform the potential landscape along the reaction coordinate asymmetrically, which makes the otherwise degenerate reactions distinguishable [158]. The corresponding reaction cross section is then readily derived:

$$\sigma_{Hi\rightarrow Lo/Lo\rightarrow Hi} = \frac{R_{Hi\rightarrow Lo/Lo\rightarrow Hi} t_{ill}}{n_{ph}} \tag{5.11}$$

where t_{ill} is the duration of light exposure and n_{ph} the photon fluence which is determined by the procedure, described in section 3.5.
Fig. 5.11(d) shows the determined cross section as function of incident photon energy, for the initial Lo and Hi state, indicated as $\sigma(Lo)$ and $\sigma(Hi)$, respectively. Across the entire measured range, the qualitative features of the spectrum are reproduced in both cross sections, while $\sigma(Hi)$ stays always below $\sigma(Lo)$ by a constant factor, as depicted in Fig. 5.11(e), where the ratio of both is plotted. For tunneling parameters V_t = 50 mV and I_t = 10 pA, the ratio was determined as $\sigma(Hi)/\sigma(Lo)$ = 0.78±0.02, independent of the incident photon energy. It was found that this ratio is independent of all varied parameters except for the tip height which may be controlled by the tunneling current feedback set point, analogous to tautomerization, induced by direct energetic charge carrier injection [158, 234]. Fig. 5.11(f) shows the measured cross section as a function of set current. The ratio between both rates is strongly influenced by the presence of the tip in the experimental tip height modulation range. As the applied bias is chosen below the threshold voltage (V_t = 150 mV) for the tunneling electron induced reaction, the tip-molecule interaction upon approach may be held accountable for the distortion of the reaction potential. All experiments were performed in constant current mode with the same tunneling parameters to keep the tip-molecule distance constant, which yields a constant $\sigma(Hi)/\sigma(Lo)$ ratio. A distinction is thus in the following omitted and the state independent cross section is determined to discuss observed spectral features.

5.3.3 Mechanism of Near-Field Mediated Photochemistry in a Tunnel Junction

It was revealed that far- and near-field excited *trans*→*cis* tautomerization on Cu(111) is a process, mediated by photoexcited charge carriers which are generated via metal absorption. We verify that this mechanism drives photoinduced chemistry also in the enhanced near-field of a stationary STM tip, positioned over the molecule. Fig. 5.12(a) shows the cross section spectral dependence, measured with an electrochemically etched Au tip for two different bistable molecular switches, adsorbed simultaneously on the surface. After deposition of porphycene, water is dosed into the STM chamber to adsorb on the Cu(110) surface, which is kept at 12 K. The water vapor is leaked into the chamber for 2 min at a pressure of $\sim 5 \times 10^{-8}$ mbar to achieve a water coverage far below one monolayer. By following the procedure, proposed in ref. [235], dimerized hydroxyl species $(OH)_2$ were obtained from repeated voltage pulses of individual H_2O molecules. Fig. 5.12(b) shows a schematic of $(OH)_2$, adsorbed on the surface, which may reversibly convert between two energetically equivalent configurations, separated by a 300 meV barrier, with an onset of

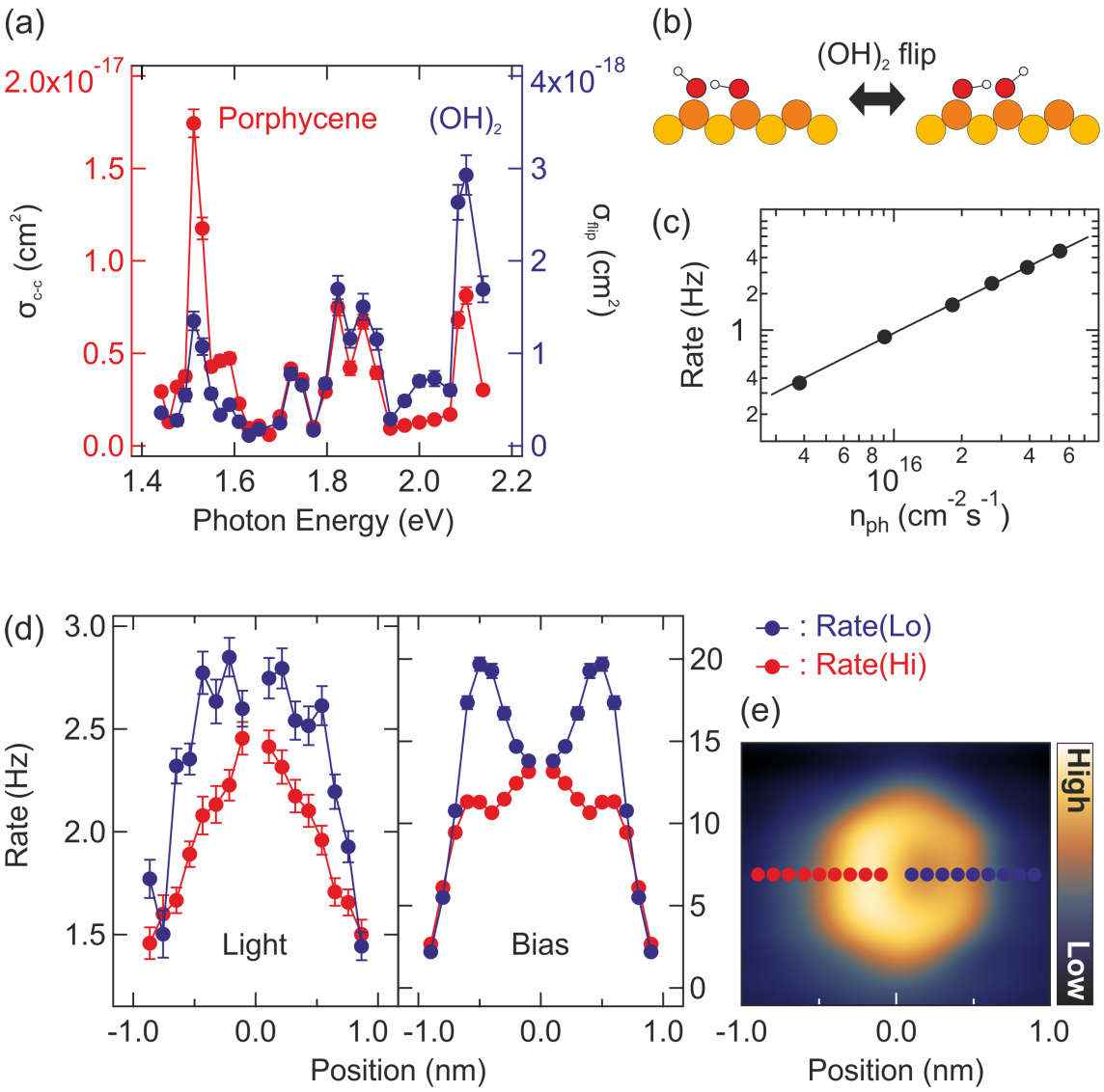

Figure 5.12: (a) Spectrally dependent photoreaction cross section of porphycene tautomerization (red) and $(OH)_2$ flip reaction (V_t = 50 mV and I_t = 10 pA). (b) Schematic representation of the $(OH)_2$ reversible conversion between two mirror symmetric states on the Cu(110) surface. (c) Photon flux dependent tautomerization rate at 690 nm excitation wavelength (tip micrograph in Fig. 5.14(d)). (d) Initial state resolved tautomerization rate as function of tip position on the molecule along the [001]-direction. Photoexcited tautomerization, measured at 690 nm excitation wavelength ($2.7(\pm\ 0.2)\times10^{16}$ $cm^{-2}s^{-1}$), V_t = 50 mV and I_t = 10 pA (Light) and tunneling electron induced tautomerization, measured at V_t = 350 mV and I_t = 10 pA (Bias). (e) Measurement positions, superimposed on a porphycene STM image.

the reaction at $\sim$ 150 meV, comparable to the energetics of porphycene tautomerization [104, 233, 235]. For both molecules, the reaction has been shown to be induced by tunneling electrons, while it was found in this work that it can also be photoexcited in the junction. The cross section spectrum for both molecular species reveals that the spectral response is

dominated by the characteristics of the tip with no observable differences for both molecular species. Both molecules are measured directly after each other and a change of the tip apex structure was not observed between measurements. As the electronic density of states for both molecules on the surface is clearly different, direct photon absorption as the driving mechanism for photochemistry can in this case be assumed to be negligible [233]. We therefore conclude that the reaction is induced by plasmon decay to e^-/h^+ pair excitations with subsequent attachment to the molecule. Fig. 5.12(c) shows the dependence of the porphycene tautomerization rate on the photon flux, taken at 690 nm excitation wavelength with the Au tip shown in Fig. 5.14(d) which reveals a linear relation, hence excluding non-linear effects of the excitation. For *trans*→*cis* tautomerization on Cu(111), it was found that charge carriers from the substrate, excited by the generated near-field, can drive the enhanced reaction, while the role of photoexcited charge carriers, tunneling from the tip could only be hypothesized to contribute in the tunneling regime. Since the experiment here is performed on a single molecule, the position dependent photoexcited tautomerization rate could be taken by scanning the tip across a porphycene molecule. Fig. 5.12(d) shows the initial state resolved rate as function of position, while the measurement points are indicated in Fig. 5.12(e). The photoreaction rate on the left is taken at an excitation wavelength of 690 nm with the Au tip shown in Fig. 5.14(d) at tunneling parameters V_t = 50 mV and I_t = 10 pA, far below the bias-induced reaction threshold of 150 meV. On the right, the same position dependence is taken without photoexcitation at V_t = 350 mV and I_t = 10 pA, which results in a high, tunneling electron induced tautomerization rate. We observe that the position dependent tunneling electron induced rate is qualitatively reproduced in the photoexcited rate, clearly indicating the dominant role of inelastic photogenerated charge carrier tunneling in the tunneling regime, as opposed to the substrate mediated excitation out of the tunneling regime. Both excitation channels are assumed to be relevant on metal surfaces and could be separately observed in the presented experiments.
It is concluded that near-field decay to e^-/h^+ pair excitations governs the porphycene tautomerization in a metallic tip-sample junctions. The charge carrier generation in the substrate dominates out of the tunneling regime, while in the tunneling regime, the photogenerated tunneling current significantly contributes.

5.3.4 SPP Interference Induced Near-Field Speckle Pattern

The ability to determine the photogenerated charge carrier induced cross section via STM facilitates the examination of the near-field properties within the tip-surface junction itself, as the charge carrier generation rate should directly relate to the local electric field intensity. Porphycene tautomerization therefore acts as a sensitivite local probe at the tip apex and may be used to discuss the plasmonic properties of the tip geometry. Fig. 5.13 shows exemplary spectra of the measured tautomerization cross section as function of incident photon energy for four different electrochemically etched Au tips. The beam polarization is perpendicular to the surface with an incident angle of about 65°. The spectral response is always observed as strongly modulated below ∼2.2 eV, where surface plasmons can be excited [30]. This modulation stands in contrast to the single broad LSPR resonance which is usually found to govern STM photo- and electroluminescence experiments [227, 236, 237]. Furthermore, each tip shows a distinctly different spectrum, which is thereby concluded to stem from the individual tip geometry. In order to systematically investigate

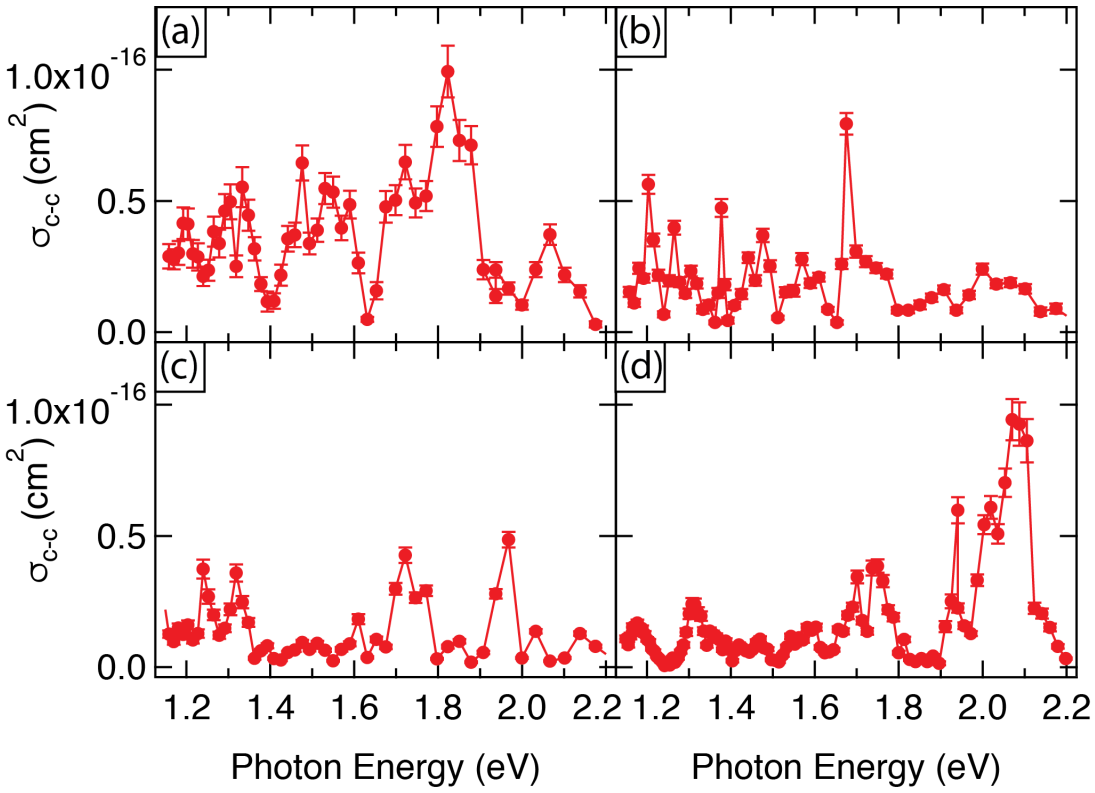

Figure 5.13: Spectrally dependent photoreaction cross section of porphycene tautomerization. Exemplary spectra are shown, taken with electrochemically etched Au tips (a) Tip 1 (b) Tip 2 (c) Tip 3 (d) Tip 4 (V_t = 50 mV and I_t = 10 pA).

the influence of the tip shape on the resulting tautomerization cross section, individual tips were polished with a focused ion beam (FIB). [26].

Fig. 5.14(a) shows a spectrum of the measured tautomerization cross section as function of incident photon energy for a sharp electrochemically etched tip, which was fabricated by following the procedure described in section 3.4. An SEM micrograph of the employed tip is shown in Fig. 5.14(d). The observed spectral modulation is assumed to be directly proportional to the charge carrier excitation rate within the junction, as charge carrier attachment was shown to drive the tautomerization reaction. Since the mean free path in noble metals in the available energy range is only tens on nanometers, we assume that the tautomerization reaction is primarily excited by charge carriers which result from the enhanced near-field close to the tip apex [26].

Polishing the tip creates a smooth surface which is milled out of an etched tip structure by following the procedure described in section 3.4.2. Two polished tips were examined with a polished length of about 19 μm (Fig. 5.14(e)) and 50 μm (Fig. 5.14(f)). The corresponding spectra are shown in Fig. 5.14(b) and Fig. 5.14(c). The spectrum can be divided in two regimes, which are described by the SPP propagation length L_{SPP}:

$$L_{SPP} = \frac{1}{2k''_{SPP}} \tag{5.12}$$

where k''_{SPP} is the imaginary part of the SPP wave vector (see section 2.3.2). L_{SPP} at the indicated threshold was determined as 11 μm and 28 μm for the two tips. The ratio of

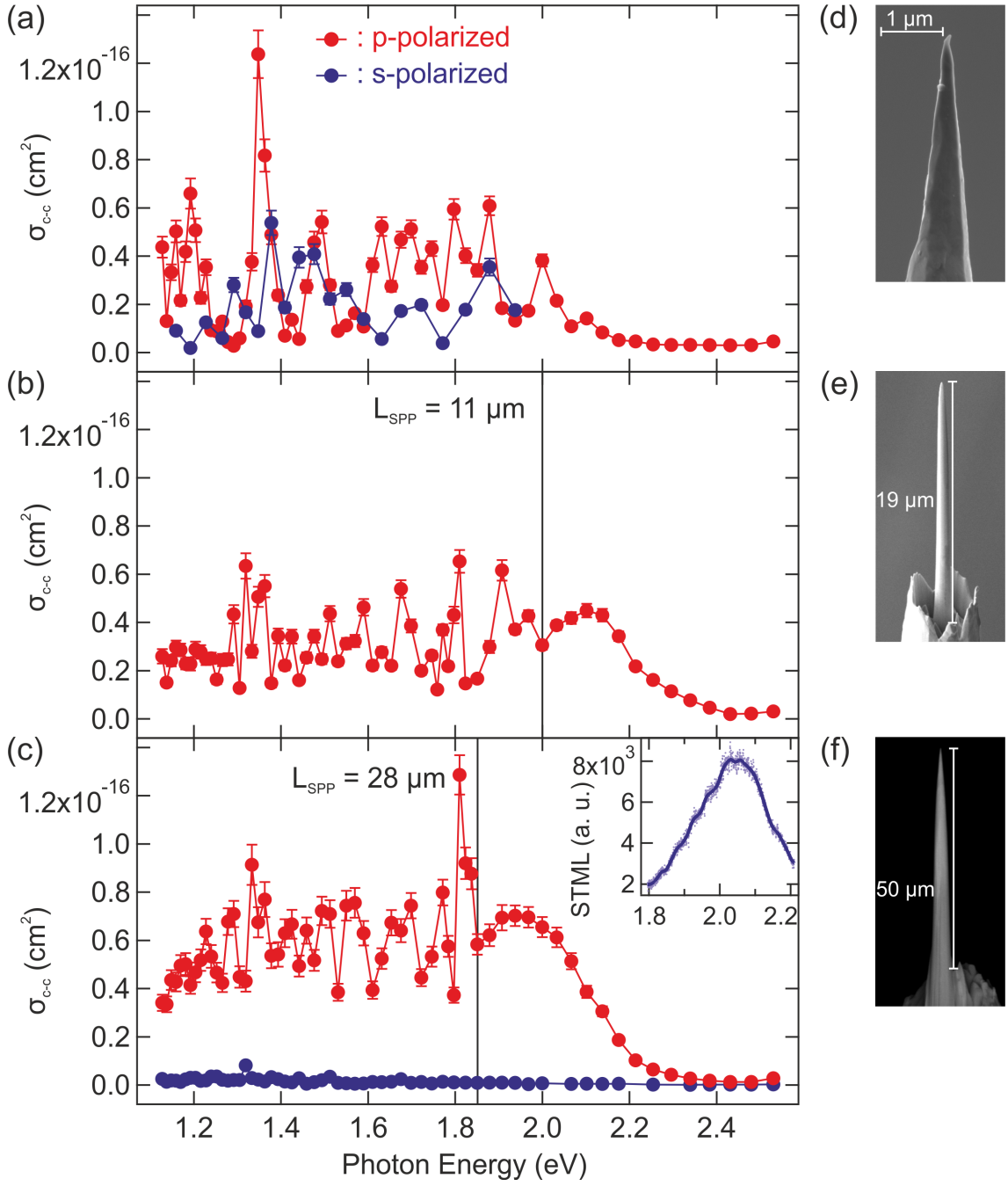

Figure 5.14: Tautomerization cross section as function of incident photon energy for different tip structures. (a) Electrochemically etched polycrystalline Au tip measured in p- (red) and s-polarization (blue). (b) Ion beam polished up to 19 μm tip length. (c) 50 μm polished tip. The inset shows an STML measurement of the same tip. Surface plasmon propagation length (L_SPP) are calculated by using Eq. 5.12. SEM micrographs of tip apex. SEM micrographs of employed tips are shown in (d)-(f).

L_{SPP} to the polished length stays within the experimental accuracy constant at 0.56 and 0.59 in Fig. 5.14(b) and Fig. 5.14(c), respectively, thus indicating the correlation of the separation with L_{SPP}. At incident photon energies larger than the indicated threshold, a single broad resonance is observed in agreement with STML measurements, as depicted in the inset of Fig. 5.14(c), which can be attributed to LSPR excitation at the tip apex. At smaller incident photon energies, the strong spectral modulation is maintained, which yields the conclusion that the modulation origins from tip surface roughness, remaining after the etching process. The correlation with L_{SPP} suggests that SPP excitation from the tip shaft results in the observed spectral behavior. Fig. 5.14(c) shows no observable enhancement with s-polarized excitation across the entire spectral range, thus indicating that the near-field is quenched. The apex of the unpolished tip in Fig. 5.14(a) is kinked which implies a stronger coupling of incident light perpendicular to the tip axis, whereas the straight apex of the polished tip may not efficiently couple to s-polarized light, due to depolarization of the apex dipole with its corresponding surface image dipole [29].
Roughness on metallic surfaces was shown to yield a complex SPP interference pattern, known as near-field speckle, which was experimentally observed by using SNOM and Photon Scanning Tunneling Microscopy (PSTM) [238–242]. The electrochemically etched rough surface of an STM tip couples light to SPPs, within the broad focus of the incident laser beam. An exemplary SEM micrograph of the electrochemically etched tip surface structure is depicted in Fig. 3.4, showing faceted structural corrugations. From the here presented observations, we conclude that the spectral response of the laser induced action spectrum origins from a speckle like modulation of the near-field at the apex due to SPP excitation from multiple structural corrugations on the tip surface. Focused ion beam polishing strongly reduces the surface roughness which yields a spectrum, dominated by the LSPR at the apex. As the near-field response is clearly related to the structural properties of the tip shaft, modifications might be used to engineer it in a desired way.

5.3.5 Manipulating the Near-Field Response with Structured Tips

The intentional engineering of SPP interference is investigated by introducing a single scatterer on the surface of a polished Au tip surface. We use FIB milling to manufacture a groove at 5 μm distance from the apex on the tip surface, which is polished on a total length of 75 μm. Fig. 5.15(a) shows an SEM micrograph of the manufactured tip. The groove depth was chosen to be 200 nm and the width was 735 nm. Fig. 5.15(b) shows the incident photon energy dependent tautomerization cross section and the near-field intensity at the tip apex, calculated by performing a finite element simulation of the employed geometry (COMSOL 5.2, RF Module). The experimental setup was approximated by a radially symmetric, spatially broad plane wave excitation of a Au tip, located at 0.6 nm distance from a Cu surface. Structural parameters are taken from the SEM micrograph, while groove to apex distance and incident illumination angle were varied to match experimental results. Good agreement was found with a taper angle of 3°, an apex radius of 35 nm, groove distance of 4.7 μm and incident illumination angle of 61.5°. The deviation of the groove distance can be rationalized by length changes due to tip forming while the deviation of the incident angle (nominal 65 °) can be caused by slight manual misalignment and tilting of the tip. The prominent peak at $\approx$ 2 eV in the measured cross section is underestimated in the simulation which may be caused by structural details of the apex, which are found in

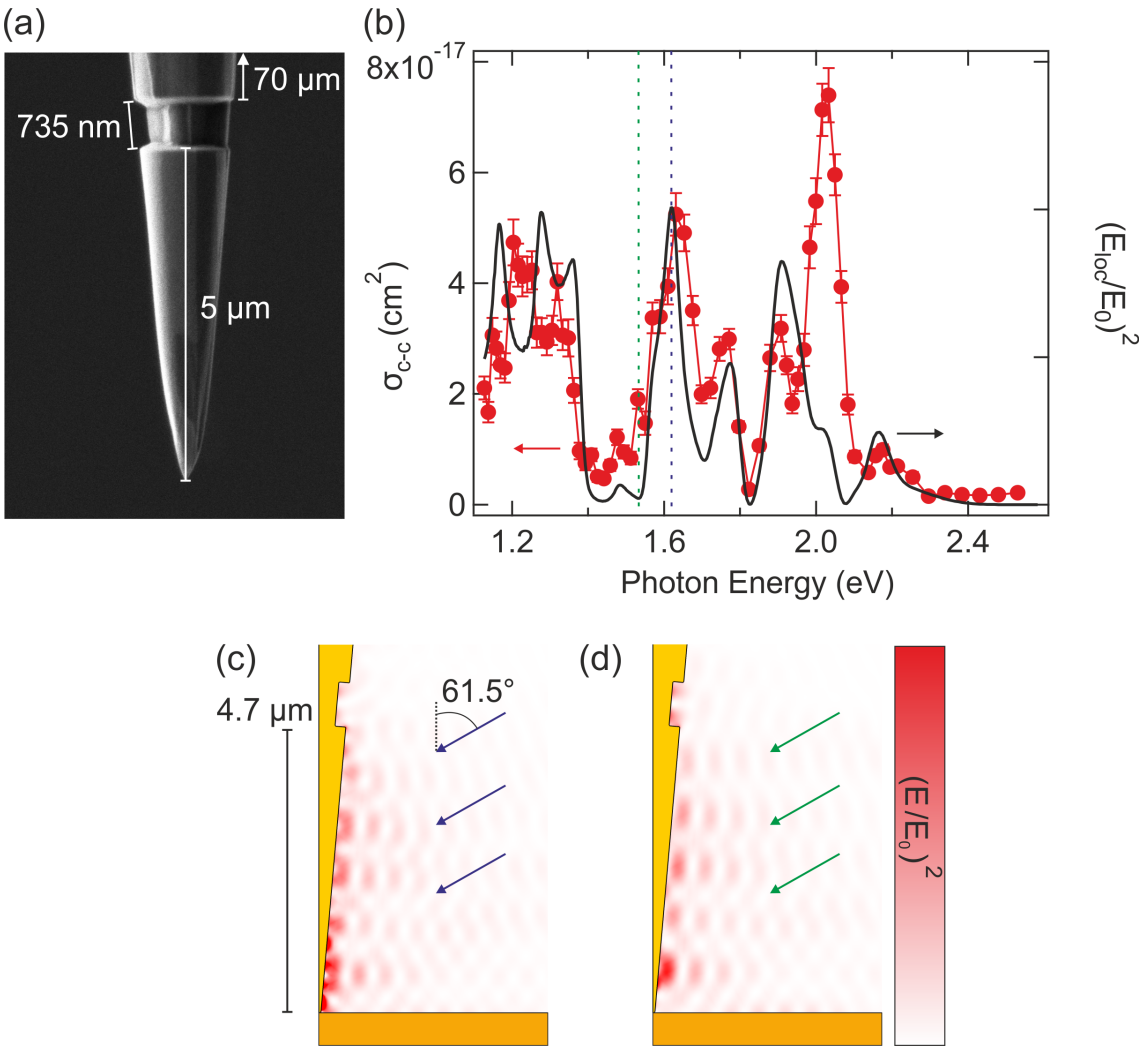

Figure 5.15: (a) SEM micrograph of a fabricated Au tip with 75 μm polished length. A 200 nm deep and 735 nm wide groove is milled onto the tip shaft at a distance of 5 μm from the apex. (b) Tautomerization cross section (red) and calculated near-field enhanced intensity at the tip apex (black) as function of incident photon energy. Exemplary plots of the calculated electric field intensity along the tip shaft for (c) 765 nm (blue dashed in (b)) and (d) 810 nm (green dashed in (b)) incident wavelength, showing both constructive and destructive interference at the apex, respectively.

simulations to sensitively influence the field intensity close to the surface plasmon energy. The results show that the near-field response at the tip apex is strongly influenced by the presence of the groove on the shaft. As the illuminated groove, like the apex, acts as an efficient center for SPP coupling, a standing wave resonance is formed within the cavity, where surface plasmons are launched and reflected at both cavity ends, thus yielding a complex interference pattern, measured at the apex location. Fig. 5.15(c) and (d) show the calculated electric field intensity in the assumed geometry at 765 nm (blue dashed in Fig. 5.15(b)) and 810 nm (green dashed in Fig. 5.15(b)) incident wavelength, respectively. Depending on the incident wavelength, i.e. the corresponding surface plasmon wavelength,

either constructive (Fig. 5.15(c)) or destructive (Fig. 5.15(d)) interference in the cavity yields stronger or weaker electric field intensities at the apex which ultimately modulates the charge carrier excitation rate and resulting tautomerization cross section. The observed speckle pattern from electrochemically etched tips can therefore be rationalized by the simultaneous excitation of multiple scattering centers by the spatially broad laser beam.

5.3.6 STML Modulation with Structured Tips

While simulations provide theoretical evidence for standing wave resonances, modulating the near-field intensity, experimental confirmation was found by performing STML with structured tips. The inelastic tunneling current in an STM represents a very localized source for surface plasmon excitation, in contrast to the spatially broad laser illumination, which was used to measure the tautomerization cross section. STML measurements were performed in a separate setup on multiple microstructured tips with varying groove to apex distance and can be directly compared to the tautomerization cross section, measured with the same tips. Fig. 5.16(a),(b),(c) show the STML spectra of tips, prepared in the same way as shown in Fig. 5.15(a) but with a groove to apex distance of 3, 6 and 10μm, respectively. A broad enhancement is observed, corresponding to the LSPR excitation at the tip apex (see inset Fig. 5.14(c)), which is further spectrally modulated with a groove to apex distance dependent enhancement and attenuation. The density of the modulation increases with the formed cavity size, which was theoretically predicted for apex illuminated microstructured SNOM tips [243]. Fig. 5.16(d),(e),(f) show Fast Fourier Transforms (FFT) of the corresponding STML spectra. The radiated photon energy is recalculated to the corresponding surface plasmon wave vector by using Eq. 2.15 and subsequently Fourier transformed to yield the SPP wavelength difference, which corresponds to the spectral modulation. Fig. 5.16(g) shows the location of the most prominent peak in the FFT spectra as function of groove to apex distance (L). A linear relation is found with a slope of 2.2±0.1, which is in good agreement with a simple Fabry-Pérot resonator model [243]:

$$\Delta\lambda_{SPP} = 2Lcos(\theta) \tag{5.13}$$

where θ is the opening angle of the tip, which was determined as 3-5° for all employed tips. However, we find an offset of $\Delta\lambda_{SPP}$) of 3.1±0.4 μm, which indicates that the linear relationship breaks down at small L, where the wavelengths in the measured spectrum approach the cavity size. The STML measurements clearly show that for localized SPP excitation at the apex, a simple resonator model describes the modulation in the radiated spectra, where the groove may be regarded as a lossy mirror.
Fig. 5.16(h),(i) show the measured tautomerization cross section for L=3 and 6 μm, respectively. It is found that the spectrum is more complex than in STML with a stronger modulation, showing that the influence of the groove on the near-field intensity at the apex is more pronounced for a spatially broad excitation source which also illuminates the groove itself. The difference in modulation amplitude may further be held responsible for the fact that speckle like near-field fluctuations on scanning probe tips are observed only for spatially broad excitation, while it was never observed in STML spectra or in photoluminescence measurements with tightly focused laser beams [227, 236, 237]. Calculations further show a spectrally dependent near-field intensity which depends on the angle of incident illumination, which is not exlpained by a Fabry-Pérot resonator model. Both groove and apex launch SPPs and may be regarded as a grating, where the resonated wavelengths

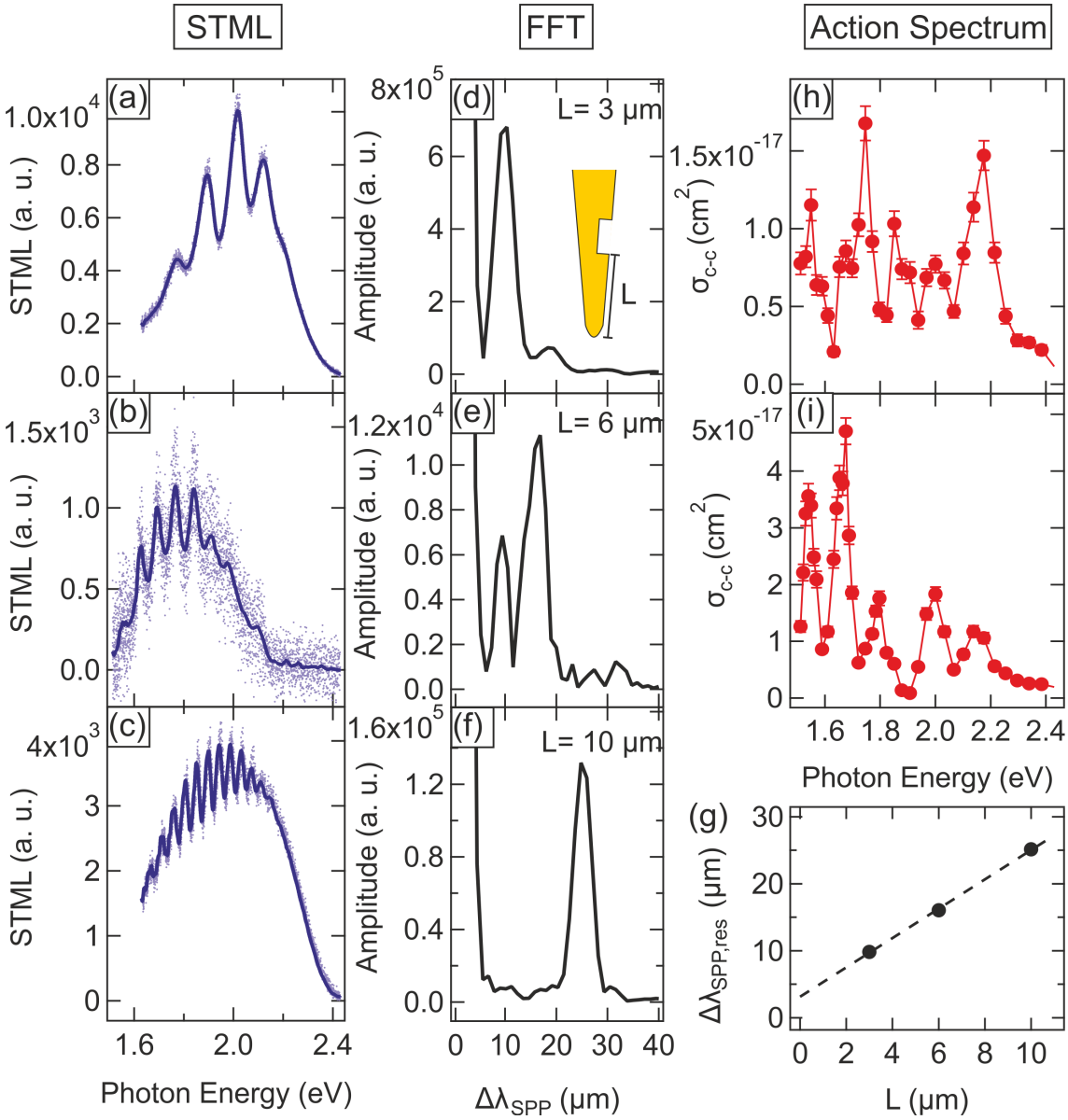

Figure 5.16: (a),(b),(c) STML (V_t = 2.5 V and I_t = 9 nA) as function of radiated photon energy for groove to apex distance L=3, 6 and 10 μm, respectively. The spectra were taken on a Ag substrate. (d),(e),(f) Corresponding FFT as function of SPP wavelength difference within modulation ($\Delta\lambda_{SPP}$) (inset indicates L). (g) Strongest resonated $\Delta\lambda_{SPP}$ as function of L, showing a linear relation with a slope of 2.2±0.1. (h),(i) Measured tautomerization cross section as function of incident photon energy for tips L=3 and 6 μm.

are known to strongly depend on the incident angle, which is experimentally observed for adiabatic focusing of surface plasmons, excited by a grating on the tip shaft [244]. By choosing the location of individual scatterers on the surface, the near-field response at the apex can therefore be manipulated with precise control and could be tuned to match desired spectral properties with high fidelity.

5.3.7 Conclusion

The photoexcited *cis* ↔ *cis* tautomerization of porphycene on Cu(110) was directly observed in the tip-sample junction of a low-temperature STM by using spectrally tunable laser excitation. It was found that non-radiative near-field decay to inelastically tunneling charge carriers from the tip induces the chemical reaction, additional to the previously shown substrate mediated excitation within the tip near-field. The near-field intensity at the apex is demonstrated to be spectrally modulated through interference of traveling surface plasmons which are simultaneously excited both at the apex and on the rough tip surface by the spatially broad illumination profile. Focused ion bombardment was used to engineer the tip surface to yield a controlled near-field response, achieved by the formation of cavity resonances between apex and surface scatterers. STML measurements confirm the formation of Fabry-Pérot resonances between apex and microstructure in a separate experiment.
The presented work demonstrates the ability to engineer the spectral properties of the near-field at a sharp metallic tip via surface structuring and presents the ability to probe its properties with a simple molecular switch. The results have implications for plasmon enhanced chemistry, where the direct observation of a chemical reaction on a fundamental level can be correlated to the plasmonic properties of an employed metal structure and therefore allows for studying the interplay between molecular properties and the near-field spectral response. Furthermore, structured scanning probes can be employed to engineer customized near-field properties in tip-enhanced techniques.

6 Plasmon Mediated Photochemistry of Formaldehyde on Cu(110)

Plasmon mediated photochemistry provides the possibility to actively control spectral absorption on metal nanostructures and can selectively promote desired adsorbate reaction channels via resonant excitation of specific electronic levels [10]. However, fundamental insight is hardly acquired from ensemble averging techniques, where active sites, adsorbate state and therefore involved reaction mechanisms are manifold and usually indistinguishable on the single-molecule level.
Here we report the plasmon mediated bistable flip reaction of formaldehyde and methoxy on a Cu(110) surface in an STM junction. The reactions are induced by plasmon mediated photoexcitation of charge carriers and subsequent transfer to the molecule. It was found that the reaction cross section is significantly increased at excitation energies exceeding the non-bonding $2b_2$ electronic resonance of physisorbed formaldehyde, while this effect was not observed for the chemisorbed methoxy, which does not exhibit an electronic resonance at this energy. The increase is assigned to a photoexcited hole transfer which induces efficiently the flip reaction as well as hopping and desorption, which may not be observed at lower excitation energies. Different electrochemically etched tips are employed both plasmonically resonant and non-resonant in the investigated excitation range, thus demonstrating the ability to potentially match the surface plasmon resonance to the adsobate electronic state. Comparison with the photoreaction cross section of porphycene tautomerization allows a separate identification of tip geometry and adsorbate resonance attributed reaction enhancement, thus providing information on the energy of generated charge carriers via near-field decay in the tunneling junction.

6.1 STM Probed Photocatalytic Reactions

The use of STM in photocatalytical research has focused exclusively on the ability to trace individual reactants and the corresponding products with atomic resolution prior and posterior to the photoexcitation. Several studies have addressed photoinduced surface processes with STM like diffusion, rotation, dissociation and bond formation by means of CW and pulsed UV and visible excitation.
The combination of a femtosecond (fs) pulsed UV light source with an STM was pioneered in 2004 by Bartels *et al.*, who successfully demonstrated non-equilibrium laser excited CO diffusion on a Cu(111) surface, notably different from thermal excitation [245]. It was revealed that individual CO molecules diffuse along and perpendicular to the close-packed $[1\bar{1}0]$ direction under fs laser excitation in a different ratio than expected for simple laser induced surface heating and thus the diffusion was concluded to be electronically driven. The identification of diffused molecules in STM was possible by choosing a low laser fluence so that the rare hopping event of a molecule may be identified relative to other molecules which have not moved during the illumination. The measurement scheme was adapted by the Morgenstern group, where chloronitrobenzene molecules were shown to diffuse and

rotate upon incident irradiation at 400 nm wavelength with pulse durations of 40 fs [246]. Furthermore, the concept was applied to water diffusion as well as hydrogen bond formation and cleavage [247]. Studies focusing again on CO diffusion on Cu(111) gain more detailed insight into the diffusion mechanism by revealing a second, high fluence diffusion mechanism, mediated by thermalized electrons as well as laser induced dimer formation [248, 249].
Visible CW radiation was presented to be able to brake the S-S in dimethyl disulfide on Ag(111) via direct excitation from the nonbonding HOMO-derived molecular orbital to the antibonding LUMO-derived molecular orbital, which is in gas phase only possible by UV radiation [250]. Further work has focused on more relevant systems for actual photocatalytic applications, like the splitting of water or methanol on TiO_2(110)-1×1, which is considered as a promising route in clean energy research ever since its discovery [59]. STM studies have provided direct evidence for Ti^{4+} as the active sites in the dissociation step of both water and methanol and it was possible to trace individual reaction products on the surface [251, 252].
In the above studies, the STM is involved passively in the photochemical process and merely used as a high resolution observation tool. However, in the emerging field of plasmon photocatalysis, active control of the catalytic hot spot, created in the nano-gap between STM tip and sample may provide fundamental insight into plasmon mediated chemistry at the single molecule level at an individual active site.

6.2 Formation and Reaction Pathways of Methanol Derivatives

Selective decomposition of methanol (CH_3OH) to formaldehyde (CH_2O) on Cu containing catalysts is an industrially relevant process and was extensively studied by employing low-index Cu surfaces [254–261]. It was found that methanol on Cu(110) is stable below ∼100 K, before it converts to methoxy (CH_3O) and subsequently formaldehyde at increasing temperature while heating above ∼300 K leads to formaldehyde desorption [254–256, 261]. Coadsorption of oxygen further promotes methanol decomposition via hydroxyl (OH) formation in the initial oxidation step [262]. High oxygen coverage leads to subsequent formate (CHO) and CO_2 formation while low coverages yield formaldehyde and atomic hydrogen at increasing temperature [263–265].
Theory and experiment show that methanol, deposited at croygenic temperatures on a Cu(110) surface, is only physisorbed at a calculated distance of more than 2Å away from the topmost Cu plane and with an almost upright C-O bond and a parallel O-H bond with respect to the surface plane [253, 266, 267]. At 6 K methanol forms stable clusters on the surface while monomers migrate across the surface as there exists only a small diffusion barrier, which has been directly observed by using STM [266, 268]. Apart from the mentioned thermal dehydrogenation, a voltage pulse of ∼1 V which is applied from the STM tip also leads to the formation of methoxy. Fig. 6.1(a) shows the schematic configuration of methanol on the surface. While methanol has a closed-shell structure, the open-shell methoxy radical strongly interacts with the surface and binds at the short bridge site with the CO bond tilted by 33° along the [001] direction from the (110) surface normal (Fig. 6.1(b)) [253, 256–259]. Fig. 6.1(e) depicts the DFT calculated local density of states of the methoxy oxygen atom at the short-bridge position of Cu(110). It was found

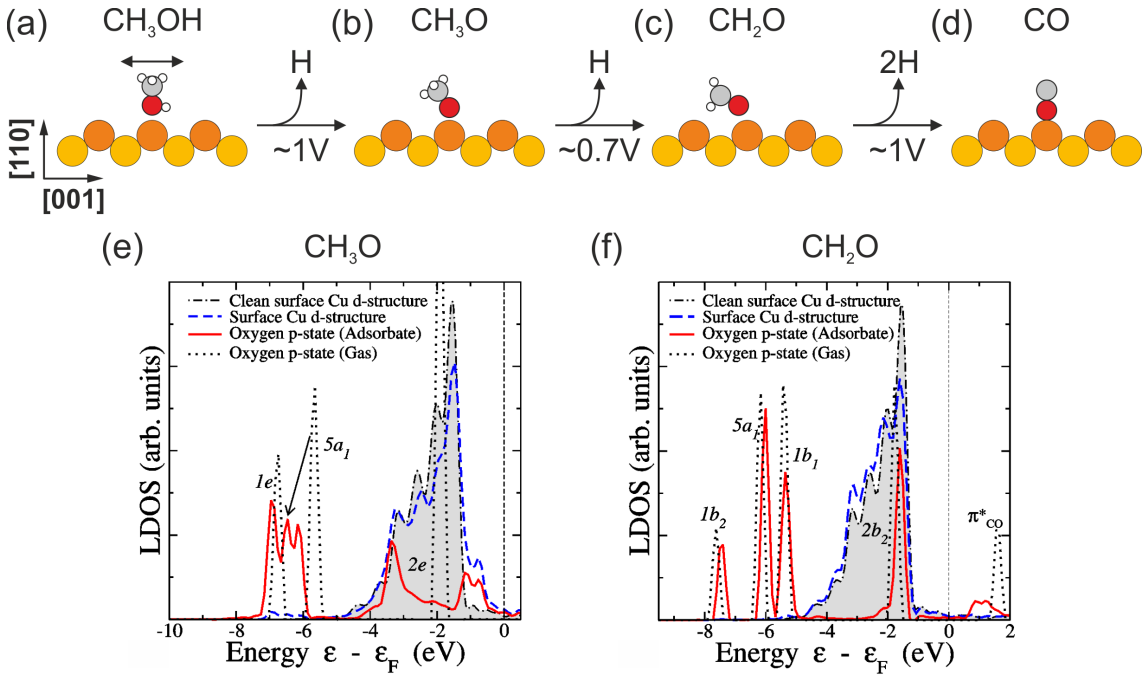

Figure 6.1: Schematic configuration and applied voltage in STM for dehydrogenation of (a) methanol (CH_3OH), mobile on the surface at 6K (b) methoxy (CH_3O), adsorbed on the short bridge site (c) formaldehyde (CH_2O), adsorbed on the top position and (d) carbon monoxide (CO), adsorbed on the top position. DFT calculated local density of states of the (e) methoxy oxygen atom and (f) η^1-formaldehyde oxygen atom on the Cu(110) surface. ((e),(f) reprinted by permission from Sakong *et al.*, Journal of Catalysis **2005**, 231, 420-429 [253], copyright 2005)

that the non-bonding 2e orbital substantially broadens upon adsorption compared to the gas phase while the p_z ($5a_1$) orbital shifts down in energy [269]. The adsorption energy was found to be -2.98 eV [267]. Another voltage pulse of ~0.7 V further converts methoxy to formaldehyde via dehydrogenation. This closed-shell species again weakly binds with the oxygen to the Cu atoms and is predicted theoretically at the short-bridge site while it was experimentally found at the top position [253, 266]. Different adsorption sites were found for formaldehyde and assigned to the weakly bound physisorbed species (η^1), which exists at a distance of about 3 Å from the surface with an adsorption energy of -0.06 eV and a chemisorbed, nearly flat lying species (η^2) with an adsorption energy of -0.46 eV, which is oriented along the troughs along the $[1\bar{1}0]$ direction [270]. Fig. 6.1(f) shows the calculated local density of states of the η^1-formaldehyde species. The gas phase electronic orbitals are nearly unperturbed upon adsorption with a slight shift of the non-bonding $2b_2$ orbital, while the antibonding π^*_{CO} orbital which is localized along the C-O bond experiences a stronger perturbation, due to the nearly parallel configuration on the surface [253, 255]. Finally, a voltage pulse of ~1 V dehydrogenates the formaldehyde to CO, while an intermediate CHO was not observed and assumed to be unstable due to its predicted exothermal dissociation on the Cu(110) surface [266, 271].
It was found in low temperature STM studies that both methoxy and η^1-formaldehyde may perform bistable switching between two mirror symmetric configurations, induced by inelastic tunneling electrons [266]. Fig. 6.2(a) shows the two methoxy configurations which

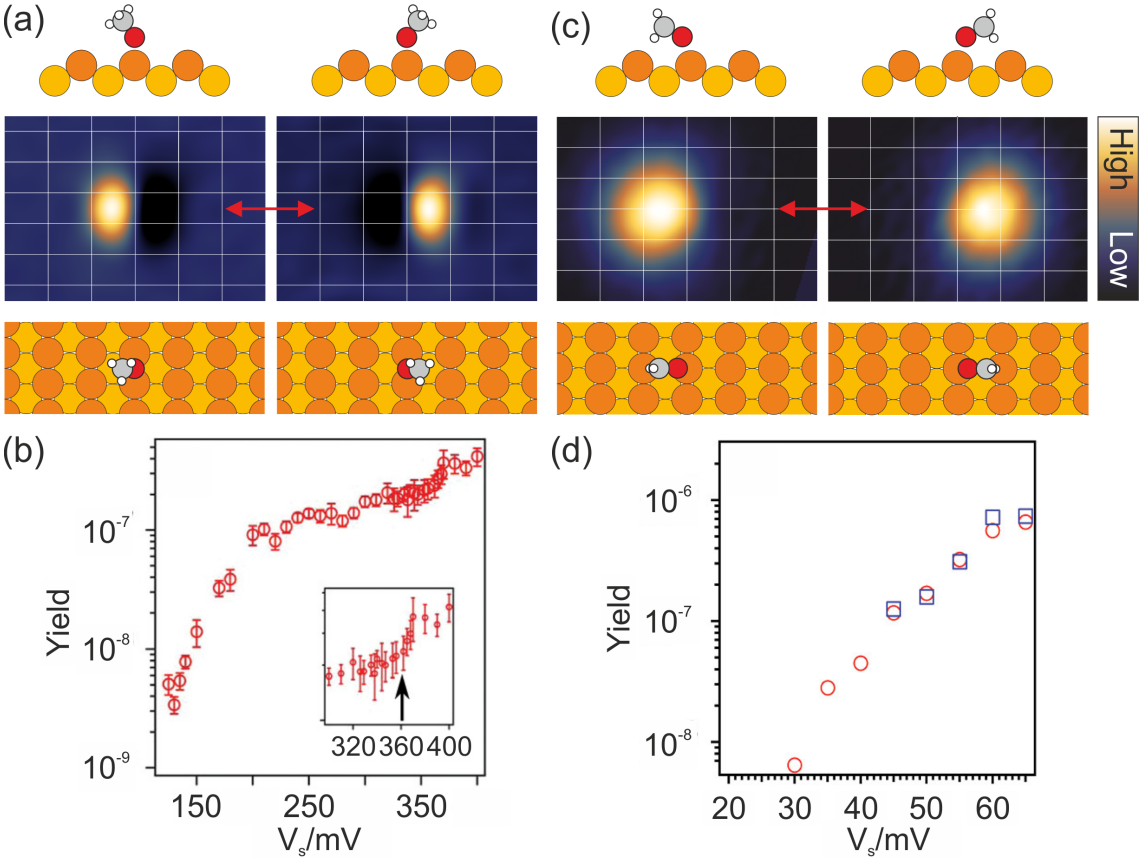

Figure 6.2: (a) Bistable flip reaction of methoxy, centered at the short bridge site in a schematic side view (top), in STM images, taken before and after the flip (center) and a schematic top view (bottom). (b) Reaction yield per tunneling electron of the flip reaction as function of applied sample bias. (c) Bistable flip reaction of η^1-formaldehyde, centered at the top site. (d) Corresponding reaction yield. ((b),(d) reprinted by permission from Kitaguchi *et al.*, Journal of Chemical Physics **2011**, 134, 174703 [266], copyright 2011)

are symmetric along the [001] plane and centered at the short bridge site. STM images before and after the performed flip reaction reveal the symmetry of the species. Fig. 6.2(b) shows the corresponding flip reaction yield per tunneling electron as function of applied sample voltage. A monotonic increase up to ∼200 meV was found, followed by a plateau and another more suddle increase at ∼360 meV, which was assigned to an excitation of the sp^3 C-H stretch mode which may couple to the reaction coordinate [272]. The reaction yield onset was tentatively assigned to an excitation of the CH_3 rock at 143 meV and possibly the CH_3 bend mode at 181 meV [256].
Fig. 6.2(c) depicts the bistable configurations of η^1-formaldehyde which may flip along the same mirror plane as methoxy but is centered at the top position. In the performed STM study, a second formaldehyde species was identified which was assigned to the η^2 configuration and showed no bistable switching at low temperatures, as it is assumed to be strongly hybridized with the substrate. Fig. 6.2(d) shows the reaction yield, which increases monotonically in the investigated voltage range with an onset at ∼30 meV, which was however not assigned to a specific vibration mode.

6.3 Photoexcited Bistable Flip Motion of Methoxy and Formaldehyde

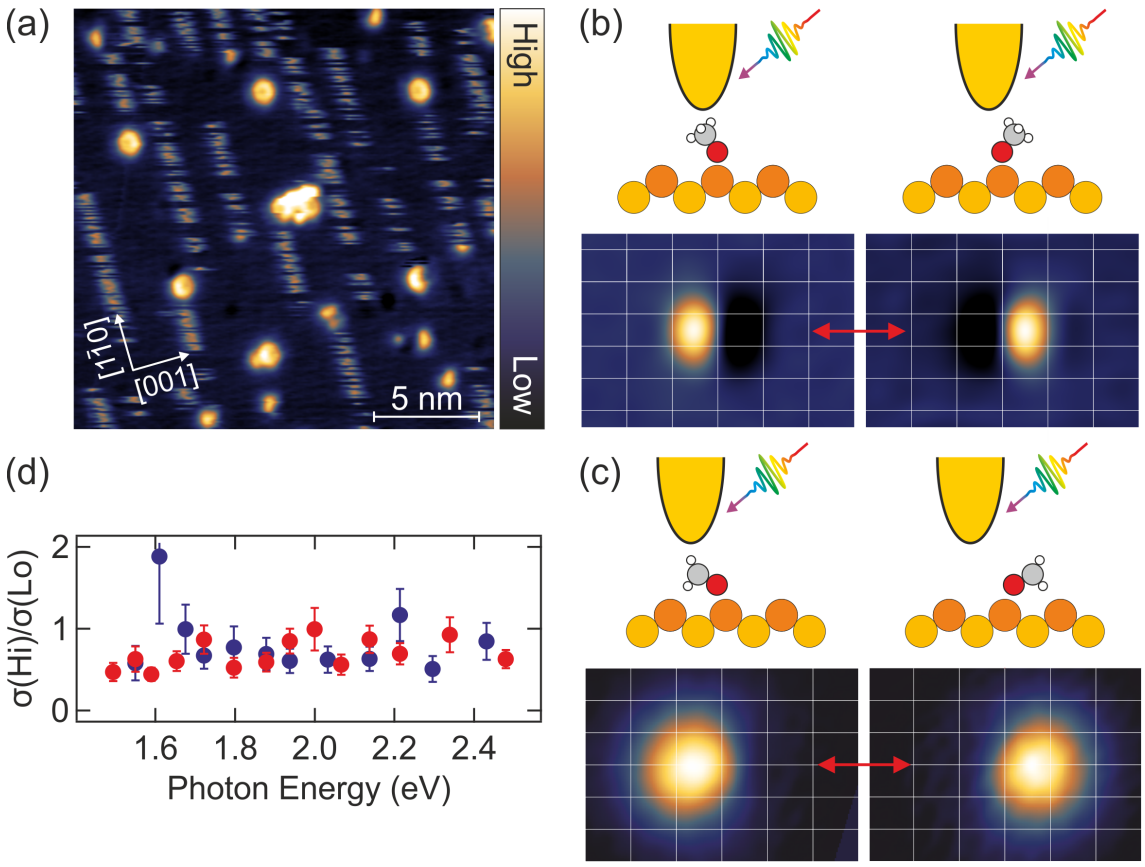

Figure 6.3: (a) Large-scale STM image after molecular deposition of porphycene and methanol (size: 20×20 nm^2, V_s = 50 mV, I_t = 30 pA). (b) Schematic of bistable CH_3O flip reaction, induced via photoexcitation. (b) Schematic of bistable CH_2O flip reaction, induced via photoexcitation. (d) Resulting initial state resolved reaction cross section as function of incident photon energy. For two employed tips, the ratio $\sigma(Hi)/\sigma(Lo)$ was found constant at 0.69±0.05 and 0.81±0.12, thus independent of the photon energy.

Methoxy and formaldehyde molecules were prepared by following the procedure, described in ref. [266]. The Cu(110) surface was cleaned and covered with a low coverage of porphycene molecules by following the procedure, described in the previous sections. Subsequently, the surface was exposed to methanol gas at a sample temperature of ∼12 K at a partial pressure of ∼5×10^{-8} mbar for 2 min. Fig. 6.3(a) shows a representative STM image of the freshly prepared surface. Porphycene molecules are readily identified by their characteristic appearance while methanol monomers appear fractional in the image as they migrate along the [1$\bar{1}$0] direction of the Cu(110) surface. The migration was identified to be intrinsic with a negligible activation barrier [268]. Stationary species on the surface are assigned methanol clusters which may be dissociated by repeated voltage pulses. Methoxy molecules were obtained from 1V voltage pulses of methanol monomers and identified by

their appearance and characteristic action spectrum for bias induced bistable switching with an onset at ∼130 mV (Fig. 6.2(b)). The same reaction could be induced by photoexcitation within the entire available energy range of the laser from 1.1-2.5 eV. Fig. 6.3(b) shows the experimental procedure. A Au scanning tip was used at V_s = 10 mV and I_t = 10 pA in constant current mode, well below the threshold for the bias induced reaction. The molecule could be further reduced to formaldehyde by applying again 1V voltage pulses. The molecule is again identified by the characteristic onset for bistable switching at ∼30 mV (Fig. 6.2(d)). The photoexcited reaction may also be induced in the entire available energy range by using the same tunneling parameters. The reaction rate and resulting cross section of the process is determined analogous to the procedure applied to tautomerization of porphycene, described in section 5.3.2, while the Hi state is here assigned to the situation where the molecule's CH_3/CH_2 group resides underneath the tip apex, while the Lo state corresponds to the opposite configuration. It was found for two different Au scanning tips that the ratio between the corresponding cross sections is independent of the incident photon energy with $\sigma(Hi)/\sigma(Lo) = 0.69\pm0.05$ and $\sigma(Hi)/\sigma(Lo) = 0.81\pm0.12$, which is why the distinction is omitted from here on.

6.4 Photoexcited Tunneling to Molecule Electronic Resonance

Following the in section 5.3 outlined methods for the determination of photoexcited reaction cross sections, two different electrochemically etched Au tips were employed to measure the flip reaction cross section for methoxy and formaldehyde as well as the tautomerization cross section for porphycene. As the here presented work was performed prior to the presented findings of near-field manipulation via tip surface structuring, solely etched tips without further treatment are employed. The molecules are prepared spatially adjacent on the surface and measured subsequently under constant illumination, to ensure both stable tip conditions and photon flux between measurements. Fig. 6.4(a) shows an STM image of the prepared molecular species on the surface before illumination. Fig. 6.4(b) shows the spectrally dependent reaction cross section for all three molecules. The tip geometry governs the spectral response of photoexcited charge carrier generation at the apex, due to surface plasmon interference, which yields the observed spectrally sharp modulations of the measured cross section (see section 5.3.4). However, as the susceptibility for charge carrier attachment and the residence time further influence the molecule interaction with the photoexcited tunneling current, the resulting reaction yield should depend significantly on the electronic density of states of the molecule on the surface [77]. Since porphycene is chemisorbed on the surface with the free N atoms binding strongly to the surface Cu atoms, it exhibits a hybridized electronic density of states across a broad energy range which has been concluded from both the lack of a molecular signature in STS measurements and calculations, predicting a strong interaction [104, 158]. On the other hand, the investigated η^1-formaldehyde species is physisorbed on Cu(110) with a calculated pronounced occupied electronic resonance at ∼1.6 eV below the Fermi energy and a more hybridized unoccupied resonance at ∼1.0 eV above within the experimentally probed energy range (see Fig. 6.1(f)). Methoxy is again predicted to be more strongly bound to the surface with hybridized weaker electronic states at ∼1.0 eV below the Fermi energy (see Fig. 6.1(e)). A pronounced interaction of charge carriers with sufficient energy to attach to the localized electronic state of

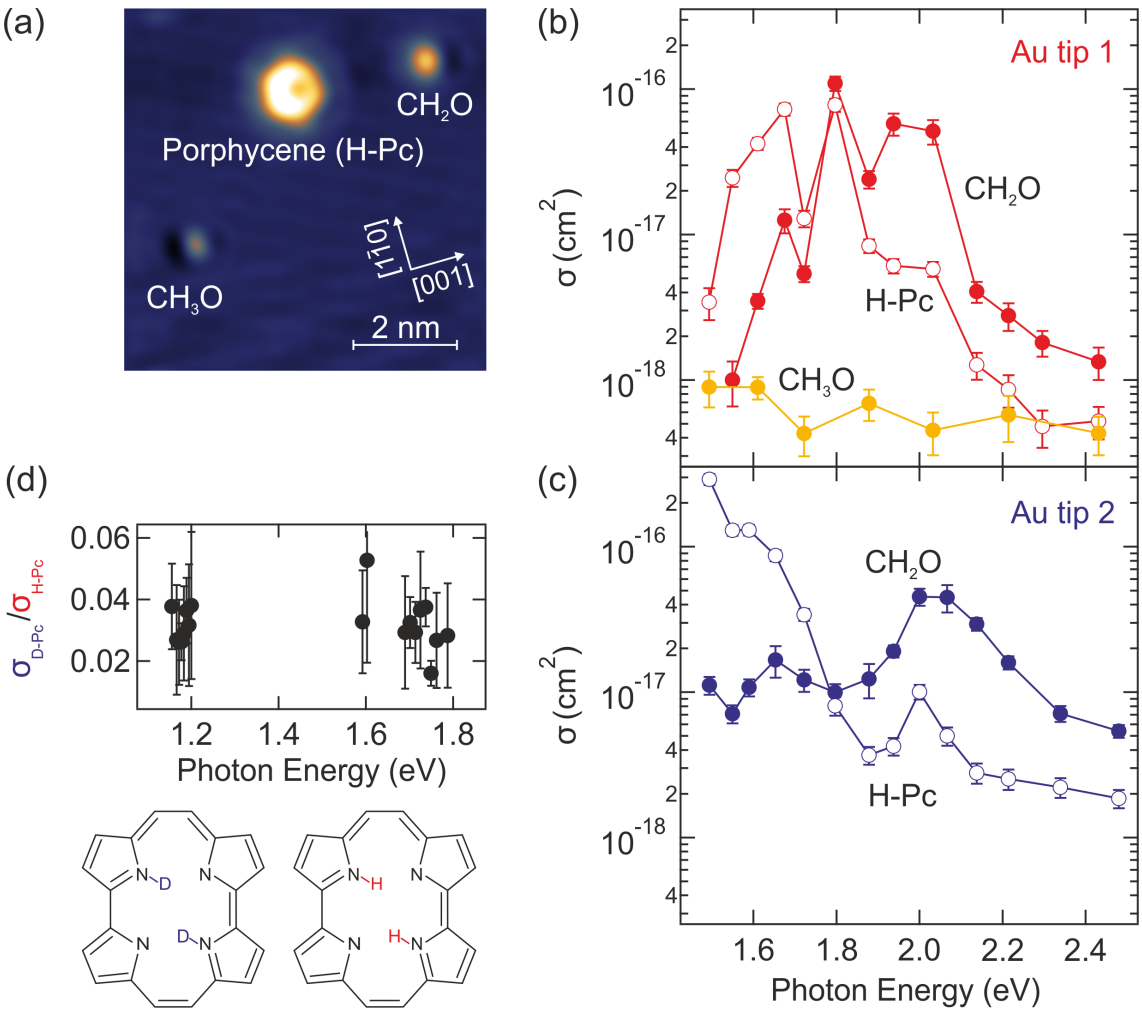

Figure 6.4: (a) STM image of prepared molecules on the surface, where CH_3O and CH_2O were obtained from sequential dehydrogenation of CH_3OH monomers (V_s = 50 mV, I_t = 30 pA). (b) Photoexcited cross section as function of the incident photon energy for CH_3O (orange filled), CH_2O (red filled) and H-Pc (red open), measured with an unmodified electrochemically etched Au tip. (c) Photoexcited cross section for CH_2O (blue filled) and H-Pc (blue open) with a different Au tip, prepared in the same way. (d) Cross section ratio between porphycene (H-Pc, structure bottom right) and cavity deuterated porphycene (D-Pc, structure bottom left). The ratio is concluded to be constant with incident photon energy.

formaldehyde may therefore be expected. While the measured cross section of formaldehyde is consistently lower than for porphycene at low incident photon energies, we observe a threshold just below 1.8 eV, while formaldehyde shows a consistently higher cross section at photon energies exceeding this threshold, hence indicating that photoexcited charge carriers interact more efficiently with the molecule. Both spectra in Fig. 6.4(b) and (c) exhibit the same threshold which is found in good agreement with the $2b_2$ resonance of formaldehyde at ∼1.6 eV below the Fermi energy and is therefore assigned to resonant attachment of photoexcited holes. This conclusion is supported by the observation that

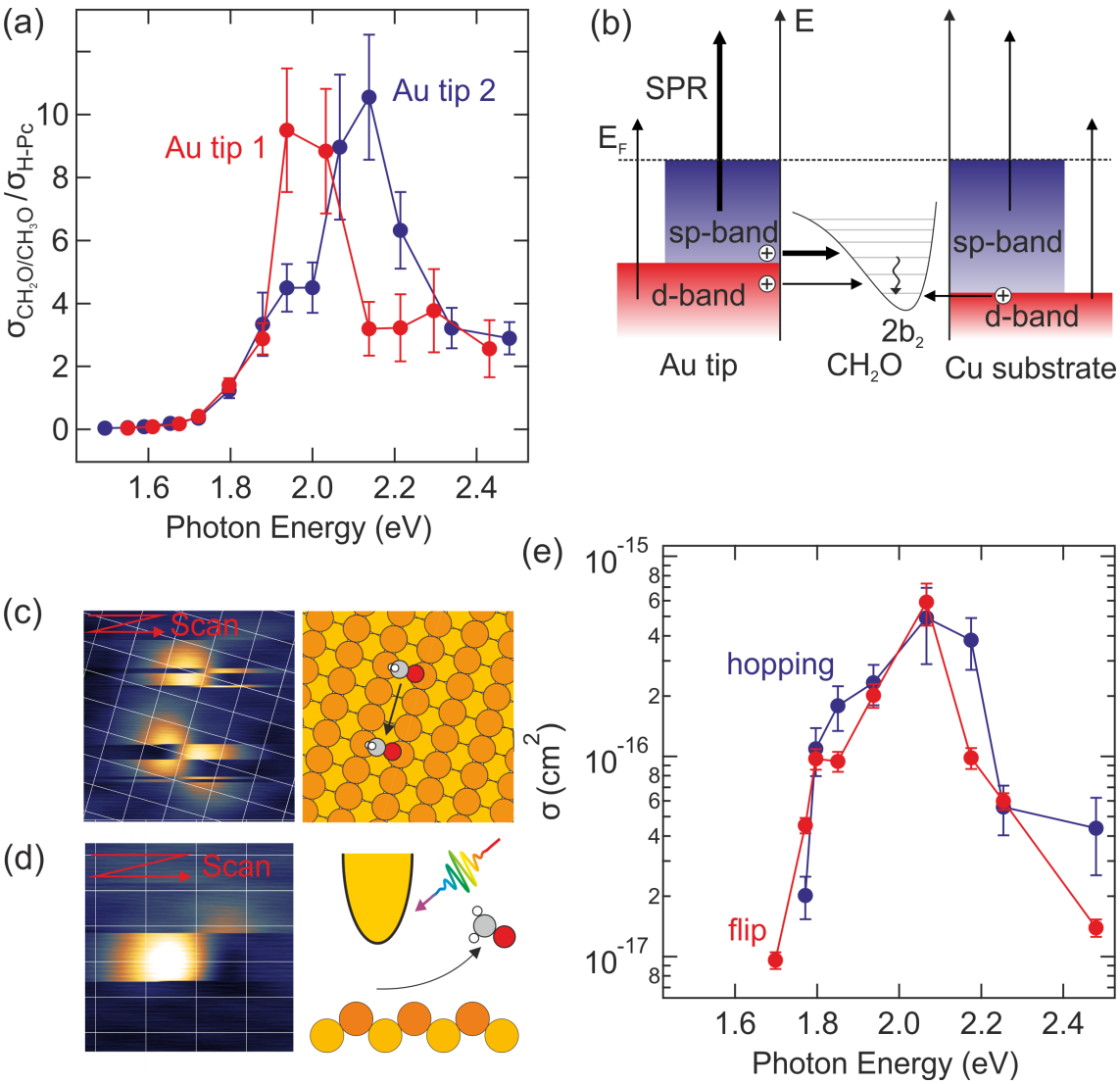

Figure 6.5: (a) Cross section ratio for both Au tips between the CH_2O (red, Au tip 1 and blue, Au tip 2) flip reaction and porphycene tautomerization as function of incident photon energy, reflecting the attachment of photoexcited holes to the CH_2O $2b_2$ orbital. (b) Schematic of the proposed model of the excitation process for surface plasmon resonance (SPR) mediated sp-band charge carrier excitation and direct absorption from the metal d-band. (c) CH_2O hopping and (d) desorption during scanning under illumination at 1.82 eV (680 nm) excitation energy, induced via hole attachment to the $2b_2$ orbital (V_s = 20 mV and I_t = 50 pA). (e) Photoexcited cross section as function of incident photon energy for the CH_2O flip (red) and hopping (blue) reaction, measured with an etched Au scanning tip.

the methoxy cross section does not exhibit a resonant enhancement which is rationalized by the lack of a pronounced electronic state in the investigated energy range. The molecule reactivity is not only dependent on the susceptibility to charge carrier attachment but also the vibronic coupling which governs the energy dissipation along the reaction coordinate. STM action spectroscopy is a viable tool to probe the energy dependence of this coupling

and to determine the involved vibrational modes at a single-molecule level [273]. Since the here considered process of photoexcited electron attachment to the molecule is similar to direct charge carrier tunneling, we may refer to the previously measured action spectra of the involved molecules, which are shown in Fig.5.10(a) for porphycene, in Fig.6.2(b) for methoxy and in Fig.6.2(d) for formaldehyde. The vibronic coupling is expected to be little influenced by the incident photon energy which largely exceeds the vibrational energy of modes in the molecule. This may be inferred from the position dependent tautomerization rate, measured on porphycene, which was shown in Fig.5.12(d). Photoexcited tautomerization resembles the bias induced position dependence, measured at V_s=350 mV, where the molecule N-H stretch is excited. It is observed that the Lo rate exceeds the Hi rate at all positions. However, the bias induced position dependence, measured in ref.[158] at V_s=300 mV, below the N-H stretch energy shows an inverted ratio between Hi and Lo rate. While the origin of this inversion is unknown, it is a robust effect and may serve as a strong indication that the photoexcited tautomerization is governed by charge carriers which exceed the N-H stretch energy.
Fig. 6.4(d) shows the cross section ratio taken for porphycene (H-Pc) and cavity deuterated porphycene (D-Pc). The cavity deuterium strongly modifies the vibronic coupling along the reaction coordinate, while there is no noticeable change in the cross section ratio as function of photon energy, which suggests that the excited molecular vibration modes remain unchanged. The STM action spectra show that the yield for methoxy reaches only up $\sim 5\times10^{-7}$ while it exceeds $\times10^{-6}$ for porphycene and methoxy. The plateau that should be reached in the yield when the highest lying vibration is excited cannot be observed, due to the limited time resolution of the STM which limits the observable reaction rate. It may therefore only be speculated that the formaldehyde and porphycene yield are comparable but this may not be experimentally verified which creates some uncertainty about the location of the observed energy threshold, assigned to the $2b_2$ resonance of formaldehyde. However, the conclusion remains valid, as it is considered unaffected by the vibronic coupling.
As plasmonic resonances are considered to affect the measured reaction cross section for both porphycene and formaldehyde, spectral enhancement from plasmonic decay should be similarly reflected. Both employed tips show a different spectral response, which is dominated by their individual geometry and which may overlap with the electronic resonance of formaldehyde. As the plasmonic response is not controlled in this experiment, spectral overlap is, however, coincidental. Fig. 6.5(a) shows the ratio between the measured cross sections of formaldehyde/porphycene which is considered unaffected by plasmonic enhancement. The formaldehyde/porphycene ratio reaches up to 10 for both tips, while the maximum is located at slightly shifted positions, which may be attributed to geometric effects in plasmonic decay within both tips [26, 38, 232]. The ratio spectral shape is readily rationalized by the overlap between the formaldehyde $2b_2$ resonance and the energy distribution of charge carriers from plasmonic decay, which is shown in Fig.2.9 for both Au and Cu. At the location of the metal d-bands, most of the photon energy is deposited into holes, while excitations from the sp-band result in an equal energy distribution. The maximum location reflects the onset of the d-bands as most photoexcited holes have an energy that is equal or exceeds the molecule electronic resonance and may therefore both efficiently attach and induce the flip reaction in formaldehyde, while the resonant attachment is absent for methoxy. Fig. 6.5(b) schematically depicts the proposed model. Photoexcited holes, primarily from the metal d-bands attach to the $2b_2$ resonance of formaldehyde which yields efficient energy transfer to the reaction coordinate via anharmonic coupling. The

surface plasmon resonance is, however, strongest below the metal d-band position which is imposed by the metal dielectric constant in the LSPR resonance condition, given in Eq.5.5. Most favorable in future experiments would be to match the spectral maximum location with the plasmonic response of a fabricated tip to overlap plasmonic and electronic resonance for efficient funneling of the light energy into a specific molecular orbital. However, as the deposited energy into holes upon plasmon decay is largest for d-band excitation, the achievable enhancement in photoreactivity may be limited. These considerations need to be taken into account for efficient matching of plasmon harvested charge carriers with molecular orbital resonances, as specificity in polarity and energy of the charge carriers is hard to control.
Additional to the bistable flip reaction, other reaction channels are observed to open up, only when charge carriers may reach the $2b_2$ resonance. Fig. 6.5(c) shows a formaldehyde molecule which hops to a different adsorption site during scanning under illumination at 1.82 eV (680 nm) excitation energy. Fig. 6.5(d) shows the molecule, desorbing from the surface during scanning at the same conditions. As the molecule is physisorbed on the surface with a calculated adsorption energy of only -0.06 eV, the reaction barrier is low and the reaction efficiency is comparable with the flip reaction, which shows an onset in the STM action spectrum of 0.03 eV [253, 266]. The hopping rate was determined by scanning the surface area, adjacent to a molecule to record the position of surrounding species. The the tip location is kept constant above the molecule under illumination until a non-reversible tip height change is observed. By scanning the area again, the change in molecule location is recognized. Fig. 6.5(e) shows the cross section, which is derived from the hopping rate together with the simultaneously measured flip reaction cross section as function of incident photon energy. A different Au tip was used for the measurement than the previously shown. The hopping shows a similar energy dependence as the flip reaction which means that the reactions are non-selectively excited by charge carrier tunneling into the $2b_2$ resonance. A similar behavior was observed for molecular desorption, however with lower probability so that a systematic evaluation was not possible.

The lateral tip position dependent flip reaction rate was determined for both photoexcitation and excitation via energetic tunneling electrons. Fig. 6.6 shows the initial state resolved reaction rate as function of lateral tip position above the molecule along the surface [001] direction, indicated in the STM image. For both excitation stimuli, the rate peaks above the location of the O atom at the top site position, while asymmetries in positive to negative direction are attributed to the tip apex geometry. However, the light induced lateral dependence appears broadened in the Hi rate while there is no obvious effect on the Lo rate. The effect is tentatively attributed to the shape of the $2b_2$ orbital, whose onset may be reached by photoexcited charge carriers at the employed excitation energy. The orbital charge density is located at the O atom and the H atoms within the molecule, so that an excitation at these positions should yield a high reaction rate and may explain the higher measured reaction rate at $\pm \sim 0.3$ nm [274]. However, the absence of a clear effect on the Lo rate remains unknown. The difference in lateral flip rate dependence was not observed for the porphycene molecule (Fig. 5.12), where molecular orbitals are strongly hybridized and little change from at different charge carrier energies may be expected.

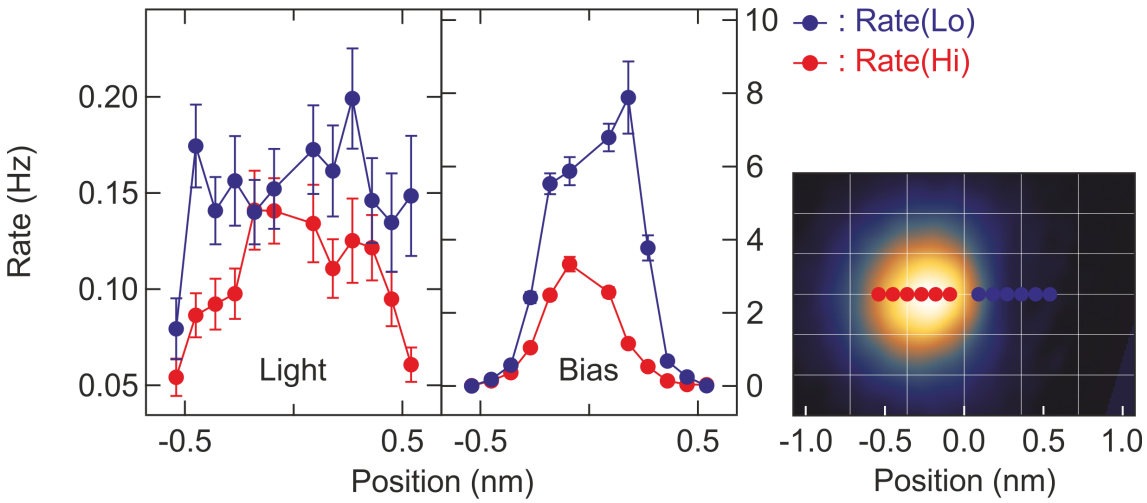

Figure 6.6: Initial state resolved flip reaction rate as function of lateral tip position above the CH_2O molecule both under illumination (Light) at 1.55 eV (800 nm) excitation, V_s = 10 mV and I_t = 10 pA and without illumination (Bias) at V_s = 33 mV and I_t = 33 pA, which is above the threshold for the bias induced reaction. The tip height is kept constant between both measurements. The bias and light induced rate peak above the O atom location at the Cu(110) top site position.

6.5 Conclusion

The photoexcited bistable flip reaction of methoxy and formaldehyde was demonstrated in the junction of a Au scanning tip and a Cu(110) surface, mediated by charge carrier attachment from near-field decay. It was found that plasmon excitation may increase the photoreaction cross section mostly by enhancing the metal intraband absorption. Resonant hole tunneling to the formaldehyde $2b_2$ lone-pair orbital is further demonstrated to enhance the cross section at photon energies exceeding the electronic resonance while the enhancement peaks when interband absorption in the metal deposits most of the absorbed photon energy into the photoexcited holes. The effect is confirmed by the lack of resonant enhancement for chemisorbed methoxy which lacks pronounced electronic structure in the investigated energy range. Further reaction channels are found to open up upon attachment to the $2b_2$ orbital, as we observe diffusion and desorption of formaldehyde molecules with a clear cutoff below the orbital energy.
The presented study reveals the possibility of employing STM as a tool to study plasmon mediated photoreactions on a single-molecule level. Action spectra of different reactions may be obtained directly from monitoring confirmational changes underneath the tip apex. In combination with the previously demonstrated ability of tip plasmon engineering, design guidelines for plasmonic photocatalysts can be derived directly in a highly controlled environement. However, specificity in polarity and energy of the resulting charge carriers is still an open challenge in future experiments.

7 Conclusion and Outlook

In this thesis, single-molecule photoinduced reactions are probed both in the optical far- and near-field. The photoinduced tautomerization of single porphycene molecules on copper surfaces was investigated in both optical regimes and employed as a model system to investigate local molecular processes. As the molecule remains adsorbed on the surface with unchanged chemical composition upon tautomerization, the combination of wavelength tunable laser excitation with STM provides a unique tool to study the photoinduced tautomerization reaction, which is demonstrated in this work.
For far-field excitation, the variation of the photoreaction cross section with photon energy in the UV to near IR range follows qualitatively the substrate absorption. We have therefore concluded that porphycene tautomerization is mediated by photoexcited substrate charge carriers.
The near-field regime was explored by exploiting the field enhancement within the nanogap, formed between substrate and a Au tip. It was found that the reaction cross section is enhanced by 10^2-10^3 in the red to near-IR spectral range, whereas, for a W tip, the enhancement is found negligible across the entire spectral range, which is consistent with surface plasmon excitation. Furthermore, the experimentally found lateral decay of the local cross section on the surface within a spatial range of $\sim$10 nm is in agreement with the expected localized field enhancement in a plasmonic junction.
In the tunneling regime, the photogenerated tunneling current due to non-radiative surface plasmon decay to charge carrier excitations is demonstrated to govern the cross section. Beyond the tunneling regime, the enhancement decays across several nanometers of tip-sample distance, following a simple coupled dipole model, which is rationalized by substrate mediated charge carrier excitation in the tip-induced near-field. The elucidation of indirect adsorbate excitation channels in a plasmonic tunneling junction gives an unprecedented detailed view on the excitation mechanism in photocatalysis, where most reactions are believed to occur in nanoscale gaps between metallic particles [57, 232]. Here we could demonstrate that tunneling of photoexcited charge carriers opens up as an additional excitation channel in near-field chemistry when those gaps enter the tunneling regime and provide direct access to the usually unknown near-field induced enhancement factor. Other experimental and theoretical studies have demonstrated the quenching of the near-field in the tunneling regime [176, 180]. Nevertheless, we find that the reaction cross section increases continuously in the tunneling regime which is rationalized by the molecular excitation due to photoexcited charge carrier tunneling.
The ability to use a single porphycene molecule as a sensitive optical switch, triggered via photoinduced carrier attachment, has been exploited to locally characterize the field enhancement and plasmonic properties of different Au tips. The shape of the tip and its surface structure is found to be of vital importance for the spectral dependence of the near-field response due to the formation of surface plasmon polariton cavity resonances between multiple surface features. While the rough surface of electrochemically etched tips results in a speckle pattern, tailoring the surface geometry with a focused ion beam can be used to manipulate the tip plasmonic properties by smoothing the surface and placing individual features (e.g. grooves) on the tip shaft. In this way, a cavity resonator is formed between tip apex and groove, which yields a tunable spectral modulation of the near-field, according to the groove position. The direct observation of the local photoreaction yield in

dependence of the nanostructure plasmonic properties has not been demonstrated before and facilitates the design of tailored plasmonic structures for near-field enhanced chemistry. Additionally, the combination of scanning probe techniques with optical spectroscopy requires reproducible and controllable near-field properties of each employed metal tip to achieve meaningful experiments which has remained a challenging topic with limited physical understanding [226]. We present a novel route to reliably fabricate scanning probe tips with controlled plasmonic properties, which may have broad implications concerning the characteristics and manipulation of the near-field in scanning probe setups. While the near-field response is usually determined by the localized surface plasmon at the tip apex, the procedure developed here allows to create spectrally sharp resonances, which may be adjusted to specific purposes (e.g. electronic or vibrational resonances).
Even though the charge carrier excitation rate due to near-field decay can be controlled in the presented way, the energy of attached charge carriers remains unknown and uncontrollable. Hence, the energy distribution is investigated by monitoring the reaction cross section of different molecular species with distinct electronic structure, which are simultanously adsorbed on the surface. The photoexcited charge carrier excitation rate is kept constant, so that relative differences in the photon energy dependent cross section between the species can be attributed to the charge carrier energy dependent reaction yield. It is demonstrated that excited charge carriers in the tunneling junction are not thermalized upon molecule attachment, as photoexcited hole tunneling to electronic states far away from the Fermi energy was found to promote the reactivity of a formaldehyde molecule. Our findings constitute direct evidence that low intensity light sources may drive reactions with large activation barriers at the surface of a photocatalyst as photoexcited tunneling provides charge carriers with energies as high as the incident photon energy. This is a necessary prerequisite to employ photocatalysis for many technologically relevant catalytic reaction. However, it remains difficult to achieve control over charge carrier polarity and energy from near-field decay as well as reaction pathway selectivity, which remain challenges to address in photocatalysis research.

References

(1) Dai, H. L.; Ho, W., *Laser Spectroscopy and Photochemistry on Metal Surfaces*; Advanced Series in Physical Chemistry pt. 1; World Scientific: 1995.

(2) Zhou, X.-L.; Zhu, X.-Y.; White, J. M. *Surface Science Reports* **1991**, *13*, 73–220.

(3) Watanabe, K.; Menzel, D.; Nilius, N.; Freund, H.-J. *Chemical Reviews* **2006**, *106*, 4301–4320.

(4) Freund, H.-J. *Surface Science* **2002**, *500*, 271–299.

(5) Kreibig, U.; Vollmer, M. In *Optical Properties of Metal Clusters*; Springer Berlin Heidelberg: 1995.

(6) Gieseking, R. L.; Ratner, M. A.; Schatz, G. C. In *Frontiers of Plasmon Enhanced Spectroscopy Volume 1*; Chapter 1, pp 1–22.

(7) Linic, S.; Christopher, P.; Ingram, D. B. *Nature Materials* **2011**, *10*, 911–921.

(8) Brongersma, M. L.; Halas, N. J.; Nordlander, P. *Nature Nanotechnology* **2015**, *10*, 25–34.

(9) Thrall, E. S.; Preska Steinberg, A.; Wu, X.; Brus, L. E. *Journal of Physical Chemistry C* **2013**, *117*, 26238–26247.

(10) Linic, S.; Aslam, U.; Boerigter, C.; Morabito, M. *Nature Materials* **2015**, *14*, 567–576.

(11) Besteiro, L. V.; Govorov, A. O. *The Journal of Physical Chemistry C* **2016**, *120*, 19329–19339.

(12) Christopher, P.; Xin, H.; Linic, S. *Nature Chemistry* **2011**, *3*, 467–472.

(13) Christopher, P.; Xin, H.; Marimuthu, A.; Linic, S. *Nature Materials* **2012**, *11*, 1044–1050.

(14) Schreier, W. J.; Schrader, T. E.; Koller, F. O.; Gilch, P.; Crespo-Hernández, C. E.; Swaminathan, V. N.; Carell, T.; Zinth, W.; Kohler, B. *Science* **2007**, *315*, 625–629.

(15) Anderson, N. A.; Shiang, J. J.; Sension, R. J. *Journal of Physical Chemistry A* **1999**, *103*, 10730–10736.

(16) Brimioulle, R.; Bach, T. *Science* **2013**, *342*, 840–843.

(17) Johnson, P. J. M.; Halpin, A.; Morizumi, T.; Prokhorenko, V. I.; Ernst, O. P.; Miller, R. J. D. *Nature Chemistry* **2015**, *7*, 980–986.

(18) Hell, S. W. *Science* **2007**, *316*, 1153–1158.

(19) Büchi, G.; Inman, C. G.; Lipinsky, E. S. *Journal of the American Chemical Society* **1954**, *76*, 4327–4331.

(20) Weller, A. *Zeitschrift für Elektrochemie, Berichte der Bunsengesellschaft für physikalische Chemie* **1956**, *60*, 1144–1147.

(21) Lochbrunner, S.; Wurzer, A. J.; Riedle, E. *The Journal of Chemical Physics* **2000**, *112*, 10699–10702.

(22) Lochbrunner, S.; Wurzer, A. J.; Riedle, E. *Journal of Physical Chemistry A* **2003**, *107*, 10580–10590.

(23) Chudoba, C.; Lutgen, S.; Jentzsch, T.; Riedle, E.; Woerner, M.; Elsässer, T. *Chemical Physics Letters* **1995**, *240*, 35–41.

(24) Lärmer, F.; Elsässer, T.; Kaiser, W. *Chemical Physics Letters* **1988**, *148*, 119–124.

(25) Antonov, L., *Tautomerism: Methods and Theories*; Wiley: 2013; Chapter Femtosecond Pump-Probe Spectroscopy of Photoinduced Tautomerism; 80 pp.

(26) Brown, A. M.; Sundararaman, R.; Narang, P.; Goddard, W. A.; Atwater, H. A. *ACS Nano* **2016**, *10*, 957–966.

(27) Menzel, D.; Gomer, R. *The Journal of Chemical Physics* **1964**, *41*, 3311–3328.

(28) Redhead, P. A. *Canadian Journal of Physics* **1964**, *42*, 886–905.

(29) Novotny, L.; Hecht, B., *Principles of Nano-Optics*; Cambridge University Press: 2006.

(30) McPeak, K. M.; Jayanti, S. V.; Kress, S. J. P.; Meyer, S.; Iotti, S.; Rossinelli, A.; Norris, D. J. *ACS Photonics* **2015**, *2*, 326–333.

(31) Prineha, N.; Ravishankar, S.; A., A. H. **2016**, *5*, 96–111.

(32) Marinica, D.; Kazansky, A.; Nordlander, P.; Aizpurua, J.; Borisov, A. G. *Nano Letters* **2012**, *12*, 1333–1339.

(33) Fedutik, Y.; Temnov, V. V.; Schöps, O.; Woggon, U.; Artemyev, M. V. *Physical Review Letters* **2007**, *99*, 136802.

(34) Fang, Z.; Liu, Z.; Wang, Y.; Ajayan, P. M.; Nordlander, P.; Halas, N. J. *Nano Letters* **2012**, *12*, 3808–3813.

(35) Atwater, H. A.; Polman, A. *Nature Materials* **2010**, *9*, 205–213.

(36) Räther, H., *Surface plasmons on smooth and rough surfaces and on gratings*; Springer tracts in modern physics; Springer: 1988.

(37) Giannini, V.; Fernández-Domínguez, A. I.; Heck, S. C.; Maier, S. A. *Chemical Reviews* **2011**, *111*, 3888–3912.

(38) Sundararaman, R.; Narang, P.; Jermyn, A. S.; Goddard III, W. A.; Atwater, H. A. *Nature Communications* **2014**, *5*, 5788.

(39) Kühn, S.; Hakanson, U.; Rogobete, L.; Sandoghdar, V. *Physical Review Letters* **2006**, *97*, 017402.

(40) Mukherjee, S.; Libisch, F.; Large, N.; Neumann, O.; Brown, L. V.; Cheng, J.; Lassiter, J. B.; Carter, E. A.; Nordlander, P.; Halas, N. J. *Nano Letters* **2013**, *13*, 240–247.

(41) Takahashi, Y.; Tatsuma, T. *Applied Physics Letters* **2011**, *99*, 182110.

(42) Mubeen, S.; Lee, J.; Singh, N.; Krämer, S.; Stucky, G. D.; Moskovits, M. *Nature Nanotechnology* **2013**, *8*, 247–251.

(43) Manjavacas, A.; Liu, J. G.; Kulkarni, V.; Nordlander, P. *ACS Nano* **2014**, *8*, 7630–7638.

(44) Bernardi, M.; Mustafa, J.; Neaton, J. B.; Louie, S. G. *Nature Communications* **2015**, *6*, 7044.

(45) Hirsch, L. R.; Stafford, R. J.; Bankson, J. A.; Sershen, S. R.; Rivera, B.; Price, R. E.; Hazle, J. D.; Halas, N. J.; West, J. L. *Proceedings of the National Academy of Sciences* **2003**, *100*, 13549–13554.

(46) El-Sayed, I. H.; Huang, X.; El-Sayed, M. A. *Cancer Letters* **2006**, *239*, 129–135.

(47) Carpin, L. B.; Bickford, L. R.; Agollah, G.; Yu, T.-K.; Schiff, R.; Li, Y.; Drezek, R. A. *Breast Cancer Research and Treatment* **2011**, *125*, 27–34.

(48) Ni, W.; Ambjörnsson, T.; Apell, S. P.; Chen, H.; Wang, J. *Nano Letters* **2010**, *10*, 77–84.

(49) Schneider, G.; Decher, G.; Nerambourg, N.; Praho, R.; Werts, M. H. V.; Blanchard-Desce, M. *Nano Letters* **2006**, *6*, 530–536.

(50) Liu, G. L.; Long, Y.-T.; Choi, Y.; Kang, T.; Lee, L. P. *Nature Methods* **2007**, *4*, 1015–1017.

(51) Tam, F.; Goodrich, G. P.; Johnson, B. R.; Halas, N. J. *Nano Letters* **2007**, *7*, 496–501.

(52) Fleischmann, M.; Hendra, P. J.; McQuillan, A. J. *Chemical Physics Letters* **1974**, *26*, 163–166.

(53) Jeanmaire, D. L.; Van Duyne, R. P. *Journal of Electroanalytical Chemistry and Interfacial Electrochemistry* **1977**, *84*, 1–20.

(54) Albrecht, M. G.; Creighton, J. A. *Journal of the American Chemical Society* **1977**, *99*, 5215–5217.

(55) Moskovits, M. *Review of Modern Physics* **1985**, *57*, 783–826.

(56) Kneipp, K.; Moskovits, M.; Kneipp, H., *Surface-Enhanced Raman Scattering: Physics and Applications*; Springer Berlin Heidelberg: 2006.

(57) Lombardi, J. R.; Birke, R. L. *Journal of Physical Chemistry C* **2008**, *112*, 5605–5617.

(58) Lombardi, J. R.; Birke, R. L.; Lu, T.; Xu, J. *The Journal of Chemical Physics* **1986**, *84*, 4174–4180.

(59) Fujishima, A.; Honda, K. *Nature* **1972**, *238*, 37–38.

(60) Kudo, A.; Miseki, Y. *Chemical Society Reviews* **2009**, *38*, 253–278.

(61) Kamat, P. V. *Journal of Physical Chemistry B* **2002**, *106*, 7729–7744.

(62) Gomes Silva, C.; Juárez, R.; Marino, T.; Molinari, R.; García, H. *Journal of the American Chemical Society* **2011**, *133*, 595–602.

(63) Awazu, K.; Fujimaki, M.; Rockstuhl, C.; Tominaga, J.; Murakami, H.; Ohki, Y.; Yoshida, N.; Watanabe, T. *Journal of the American Chemical Society* **2008**, *130*, 1676–1680.

(64) Gavnholt, J.; Rubio, A.; Olsen, T.; Thygesen, K. S.; Schiotz, J. *Physical Review B* **2009**, *79*, 195405.

(65) Ertel, K.; Kohl, U.; Lehmann, J.; Merschdorf, M.; Pfeiffer, W.; Thon, A.; Voll, S.; Gerber, G. *Applied Physics B* **1999**, *68*, 439–445.

(66) Mukherjee, S.; Zhou, L.; Goodman, A. M.; Large, N.; Ayala-Orozco, C.; Zhang, Y.; Nordlander, P.; Halas, N. J. *Journal of the American Chemical Society* **2014**, *136*, 64–67.

(67) Jin, R.; Charles Cao, Y.; Hao, E.; Métraux, G. S.; Schatz, G. C.; Mirkin, C. A. *Nature* **2003**, *425*, 487–490.

(68) Binnig, G.; Rohrer, H.; Gerber, C.; Weibel, E. *Physical Review Letters* **1983**, *50*, 120–123.

(69) Feenstra, R. M. *Surface Science* **1994**, *299-300*, 965–979.

(70) Hamers, R. J.; Tromp, R. M.; Demuth, J. E. *Physical Review Letters* **1986**, *56*, 1972–1975.

(71) Muralt, P.; Pohl, D. W. *Applied Physics Letters* **1986**, *48*, 514–516.

(72) Eigler, D. M.; Schweizer, E. K. *Nature* **1990**, *344*, 524.

(73) Shiotari, A., *Reactivity of Nitric Oxide on Copper Surfaces: Elucidated by Direct Observation of Valence Orbitals*; Springer Singapore: 2017.

(74) Tersoff, J.; Hamann, D. R. *Physical Review Letters* **1983**, *50*, 1998–2001.

(75) Bardeen, J. *Physical Review Letters* **1961**, *6*, 57–59.

(76) Tersoff, J.; Hamann, D. R. *Physical Review B* **1985**, *31*, 805–813.

(77) Lang, N. D. *Physical Review B* **1986**, *34*, 5947–5950.

(78) GmbH, S. O. Omicron Low-Temperature SPM. Online; accessed 2-January-2018, `http://www.scientaomicron.com/en/products/low-temperature-spm/instrument-concept`.

(79) GmbH, S. Z. Nanonis Control Systems. Online; accessed 2-January-2018, `http://www.specs-zurich.com/en/SPM-Control-System.html`.

(80) GmbH, M. Metal single crystals. Online; accessed 2-January-2018, `http://www.mateck.de/index.php?lang=en&Itemid=7`.

(81) GmbH, K. Kentax UHV Evaporator TCE-BSC. Online; accessed 2-January-2018, `http://www.kentax.de/uhv-evaporator-tce-three-cell.html`.

(82) Müller-Rösch, M. Femtosecond low-energy electron imaging and diffraction using nanotip photoemitters., Ph.D. Thesis, Free University Berlin, 2017.

(83) Pettinger, B.; Picardi, G.; Schuster, R.; Ertl, G. *Single Molecules* **2002**, *3*, 285–294.

(84) Ren, B.; Picardi, G.; Pettinger, B. *Review of Scientific Instruments* **2004**, *75*, 837–841.

(85) Plottke, H. Präparation und Charakterisierung von Wolfram-Nanospitzen als Feldemissions-Elektronenquelle., MA thesis, Freie Universität Berlin, 2012.

(86) Xu, G.; Liu, Z.; Xu, K.; Zhang, Y.; Zhong, H.; Fan, Y.; Huang, Z. *Review of Scientific Instruments* **2012**, *83*, 103708.

(87) Scientific, T. F. Helios Nanolab G3 UC. Online; accessed 3-March-2018, `https://www.fei.com/products/dualbeam/helios-g4-uc-for-materials-science/`.

(88) Photonics, N. Supercontinuum white light laser source. Online; accessed 4-January-2018, `http://www.nktphotonics.com/lasers-fibers/en/product/superk-extreme-supercontinuum-lasers/`.

(89) McIlwain, J., *An Introduction to the Biology of Vision*; Cambridge University Press: 1996.

(90) Yoshikawa, S.; Shimada, A.; Shinzawa-Itoh, K. In *Sustaining Life on Planet Earth: Metalloenzymes Mastering Dioxygen and Other Chewy Gases*; Springer International Publishing: 2015, pp 89–130.

(91) Feringa, B. L.; Jager, W. F.; de Lange, B. *Tetrahedron* **1993**, *49*, 8267–8310.

(92) Feringa, B. L. *Angewandte Chemie International Edition* **2017**, *56*, 11060–11078.

(93) Lukas, A. S.; Wasielewski, M. R. In *Molecular Switches*; Wiley-VCH Verlag GmbH: 2001, pp 1–35.

(94) Wang, T.; Nijhuis, C. A. *Applied Materials Today* **2016**, *3*, 73–86.

(95) Comstock, M. J.; Levy, N.; Kirakosian, A.; Cho, J.; Lauterwasser, F.; Harvey, J. H.; Strubbe, D. A.; Fréchet, J. M. J.; Trauner, D.; Louie, S. G.; Crommie, M. F. *Physical Review Letters* **2007**, *99*, 038301.

(96) Comstock, M. J.; Levy, N.; Cho, J.; Berbil-Bautista, L.; Crommie, M. F.; Poulsen, D. A.; Fréchet, J. M. J. *Applied Physics Letters* **2008**, *92*, 123107.

(97) Levy, N.; Comstock, M. J.; Cho, J.; Berbil-Bautista, L.; Kirakosian, A.; Lauterwasser, F.; Poulsen, D. A.; Fréchet, J. M. J.; Crommie, M. F. *Nano Letters* **2009**, *9*, 935–939.

(98) Comstock, M. J.; Strubbe, D. A.; Berbil-Bautista, L.; Levy, N.; Cho, J.; Poulsen, D.; Fréchet, J. M. J.; Louie, S. G.; Crommie, M. F. *Physical Review Letters* **2010**, *104*, 178301.

(99) Bazarnik, M.; Henzl, J.; Czajka, R.; Morgenstern, K. *Chemical Communications* **2011**, *47*, 7764–7766.

(100) Henzl, J.; Puschnig, P.; Ambrosch-Draxl, C.; Schaate, A.; Ufer, B.; Behrens, P.; Morgenstern, K. *Physical Review B* **2012**, *85*, 035410.

(101) Bronner, C.; Schulze, G.; Franke, K. J; Pascual, J. I.; Tegeder, P. *Journal of Physics: Condensed Matter* **2011**, *23*, 484005.

(102) Liljeroth, P.; Repp, J.; Meyer, G. *Science* **2007**, *317*, 1203–1206.

(103) Auwärter, W.; Seufert, K.; Bischoff, F.; Ecija, D.; Vijayaraghavan, S.; Joshi, S.; Klappenberger, F.; Samudrala, N.; Barth, J. V. *Nature Nanotechnology* **2011**, *7*, 41–46.

(104) Kumagai, T.; Hanke, F.; Gawinkowski, S.; Sharp, J.; Kotsis, K.; Waluk, J.; Persson, M.; Grill, L. *Physical Review Letters* **2013**, *111*, 246101.

(105) Simpson, G. J.; Hogan, S. W. L.; Caffio, M.; Adams, C. J.; Früchtl, H.; van Mourik, T.; Schaub, R. *Nano Letters* **2014**, *14*, 634–639.

(106) Qiu, X. H.; Nazin, G. V.; Ho, W. *Physical Review Letters* **2004**, *93*, 196806.

(107) Choi, B.-Y.; Kahng, S.-J.; Kim, S.; Kim, H.; Kim, H. W.; Song, Y. J.; Ihm, J.; Kuk, Y. *Physical Review Letters* **2006**, *96*, 156106.

(108) Pavlicek, N.; Fleury, B.; Neu, M.; Niedenführ, J.; Herranz-Lancho, C.; Ruben, M.; Repp, J. *Physical Review Letters* **2012**, *108*, 086101.

(109) Zhang, J. L.; Xu, J. L.; Niu, T. C.; Lu, Y. H.; Liu, L.; Chen, W. *Journal of Physical Chemistry C* **2014**, *118*, 1712–1718.

(110) Li Huang, Y.; Lu, Y.; Niu, T. C.; Huang, H.; Kera, S.; Ueno, N.; Wee, A. T. S.; Chen, W. *Small* **2012**, *8*, 1423–1428.

(111) Miyamachi, T.; Gruber, M.; Davesne, V.; Bowen, M.; Boukari, S.; Joly, L.; Scheurer, F.; Rogez, G.; Yamada, T. K.; Ohresser, P.; Beaurepaire, E.; Wulfhekel, W. *Nature Communications* **2012**, *3*, 938.

(112) Gopakumar, T. G.; Matino, F.; Naggert, H.; Bannwarth, A.; Tuczek, F.; Berndt, R. *Angewandte Chemie International Edition* **2012**, *51*, 6262–6266.

(113) Leoni, T.; Guillermet, O.; Walch, H.; Langlais, V.; Scheuermann, A.; Bonvoisin, J.; Gauthier, S. *Physical Review Letters* **2011**, *106*, 216103.

(114) Fu, Y.-S.; Zhang, T.; Ji, S.-H.; Chen, X.; Ma, X.-C.; Jia, J.-F.; Xue, Q.-K. *Physical Review Letters* **2009**, *103*, 257202.

(115) Swart, I.; Sonnleitner, T.; Repp, J. *Nano Letters* **2011**, *11*, 1580–1584.

(116) Mohn, F.; Repp, J.; Gross, L.; Meyer, G.; Dyer, M. S.; Persson, M. *Physical Review Letters* **2010**, *105*, 266102.

(117) Alemani, M.; Peters, M. V.; Hecht, S.; Rieder, K.-H.; Moresco, F.; Grill, L. *Journal of the American Chemical Society* **2006**, *128*, 14446–14447.

(118) Weigelt, S.; Busse, C.; Petersen, L.; Rauls, E.; Hammer, B.; Gothelf, K. V.; Besenbacher, F.; Linderoth, T. R. *Nature Materials* **2006**, *5*, 112–117.

(119) Henzl, J.; Bredow, T.; Morgenstern, K. *Chemical Physics Letters* **2007**, *435*, 278–282.

(120) Henzl, J.; Mehlhorn, M.; Gawronski, H.; Rieder, K.-H.; Morgenstern, K. *Angewandte Chemie International Edition* **2006**, *45*, 603–606.

(121) Henningsen, N.; Franke, K. J.; Torrente, I. F.; Schulze, G.; Priewisch, B.; Rück-Braun, K.; Doki, J.; Klamroth, T.; Saalfrank, P.; Pascual, J. I. *The Journal of Physical Chemistry C* **2007**, *111*, 14843–14848.

(122) Wang, Y.; Kröger, J.; Berndt, R.; Hofer, W. A. *Journal of the American Chemical Society* **2009**, *131*, 3639–3643.

(123) Chen, L.; Li, H.; Wee, A. T. S. *ACS Nano* **2009**, *3*, 3684–3690.

(124) Huang, T.; Zhao, J.; Feng, M.; Popov, A. A.; Yang, S.; Dunsch, L.; Petek, H. *Nano Letters* **2011**, *11*, 5327–5332.

(125) Liu, L.; Yang, K.; Jiang, Y.; Song, B.; Xiao, W.; Li, L.; Zhou, H.; Wang, Y.; Du, S.; Ouyang, M.; Hofer, W. A; Castro Neto, A. H; Gao, H.-J. *Scientific Reports* **2013**, *3*, 1210.

(126) Strózecka, A.; Soriano, M.; Pascual, J. I.; Palacios, J. J. *Physical Review Letters* **2012**, *109*, 147202.

(127) Hartley, G. S. *Nature* **1937**, *140*, 281.

(128) Dürr, H.; Bouas-Laurent, H., *Photochromism: Molecules and Systems*; Elsevier Science: 2003.

(129) Hugel, T.; Holland, N. B.; Cattani, A.; Moroder, L.; Seitz, M.; Gaub, H. E. *Science* **2002**, *296*, 1103–1106.

(130) Wolf, M.; Tegeder, P. *Surface Science* **2009**, *603*, 1506–1517.

(131) Schulze, G.; Franke, K. J.; Pascual, J. I. *Physical Review Letters* **2012**, *109*, 026102.

(132) Cohen, M. D.; Schmidt, G. M. J. *The Journal of Physical Chemistry* **1962**, *66*, 2442–2446.

(133) Katsumi, T.; Tatsuo, A.; Masaya, M. *Molecular Crystals and Liquid Crystals Science and Technology. Section A. Molecular Crystals and Liquid Crystals* **1994**, *246*, 147–149.

(134) Tapia, O.; Andres, J.; Safont, V. S. *The Journal of Physical Chemistry* **1994**, *98*, 4821–4830.

(135) Wang, W.; Hellinga, H. W.; Beese, L. S. *Proceedings of the National Academy of Sciences* **2011**, *108*, 17644–17648.

(136) Watson, J. D.; Crick, F. H. C. *Nature* **1953**, *171*, 964.

(137) Topal, M. D.; Fresco, J. R. *Nature* **1976**, *263*, 285–289.

(138) Morgan, A. *Trends in Biochemical Sciences* **1993**, *18*, 160–163.

(139) Robert, F.; Jacquemin, P.-L.; Tinant, B.; Garcia, Y. *Crystal Engineering Communications* **2012**, *14*, 4396–4406.

(140) Kawata, S.; Kawata, Y. *Chemical Reviews* **2000**, *100*, 1777–1788.

(141) Joachim, C.; Gimzewski, J. K.; Aviram, A. *Nature* **2000**, *408*, 541–548.

(142) Aviram, A.; Ratner, M. A. *Chemical Physics Letters* **1974**, *29*, 277–283.

(143) Heath, J. R.; Ratner, M. A. *Physics Today* **2003**, *56*, 43–49.

(144) Sperl, A.; Kröger, J.; Berndt, R. *Angewandte Chemie International Edition* **2011**, *50*, 5294–5297.

(145) Simão, C.; Mas-Torrent, M.; Casado-Montenegro, J.; Otón, F.; Veciana, J.; Rovira, C. *Journal of the American Chemical Society* **2011**, *133*, 13256–13259.

(146) Vogel, E.; Köcher, M.; Schmickler, H.; Lex, J. *Angewandte Chemie International Edition in English* **1986**, *25*, 257–259.

(147) Gawinkowski, S.; Walewski, L.; Vdovin, A.; Slenczka, A.; Rols, S.; Johnson, M. R.; Lesyng, B.; Waluk, J. *Physical Chemistry Chemical Physics* **2012**, *14*, 5489–5503.

(148) Langer, U.; Hoelger, C.; Wehrle, B.; Latanowicz, L.; Vogel, E.; Limbach, H.-H. *Journal of Physical Organic Chemistry* **2000**, *13*, 23–34.

(149) Webb, L. E.; Fleischer, E. B. *The Journal of Chemical Physics* **1965**, *43*, 3100–3111.

(150) Braun, J.; Köcher, M.; Schlabach, M.; Wehrle, B.; Limbach, H.-H.; Vogel, E. *Journal of the American Chemical Society* **1994**, *116*, 6593–6604.

(151) Fita, P.; Urbaska, N.; Radzewicz, C.; Waluk, J. *Chemistry - A European Journal* **2009**, *15*, 4851–4856.

(152) Waluk, J.; Vogel, E. *The Journal of Physical Chemistry* **1994**, *98*, 4530–4535.

(153) Gil, M.; Waluk, J. *Journal of the American Chemical Society* **2007**, *129*, 1335–1341.

(154) Fita, P.; Radzewicz, C.; Waluk, J. *The Journal of Physical Chemistry A* **2008**, *112*, 10753–10757.

(155) Mengesha, E. T.; Sepio, J.; Borowicz, P.; Waluk, J. *The Journal of Chemical Physics* **2013**, *138*, 174201.

(156) Taylor, C. A.; El-Bayoumi, M. A.; Kasha, M. *Proceedings of the National Academy of Sciences* **1969**, *63*, 253–260.

(157) Wu, Y.-D.; Chan, K. W. K.; Yip, C.-P.; Vogel, E.; Plattner, D. A.; Houk, K. N. *Journal of Organic Chemistry* **1997**, *62*, 9240–9250.

(158) Kumagai, T.; Hanke, F.; Gawinkowski, S.; Sharp, J.; Kotsis, K.; Waluk, J.; Persson, M.; Grill, L. *Nature Chemistry* **2013**, *6*, 41–46.

(159) Novko, D.; Tremblay, J. C.; Blanco-Rey, M. *The Journal of Chemical Physics* **2016**, *145*, 244701.

(160) Novko, D.; Tremblay, J. C.; Blanco-Rey, M. *The Journal of Chemical Physics* **2017**, *147*, 169901.

(161) Ladenthin, J. N.; Grill, L.; Gawinkowski, S.; Liu, S.; Waluk, J.; Kumagai, T. *ACS Nano* **2015**, *9*, 7287–7295.

(162) Davey, W. P. *Physical Review* **1925**, *25*, 753–761.

(163) Waluk, J.; Müller, M.; Swiderek, P.; Kocher, M.; Vogel, E.; Hohlneicher, G.; Michl, J. *Journal of the American Chemical Society* **1991**, *113*, 5511–5527.

(164) Novko, D.; Blanco-Rey, M.; Tremblay, J. C. *The Journal of Physical Chemistry Letters* **2017**, *8*, 1053–1059.

(165) Ying, Z. C.; Ho, W. *The Journal of Chemical Physics* **1990**, *93*, 9089–9095.

(166) Ying, Z. C.; Ho, W. *Physical Review Letters* **1990**, *65*, 741–744.

(167) Tsymbal, E.; Pettifor, D. In *Solid State Physics*, Ehrenreich, H., Spaepen, F., Eds.; Solid State Physics, Vol. 56; Academic Press: 2001, pp 113 –237.

(168) Rakic, A. D.; Djurisic, A. B.; Elazar, J. M.; Majewski, M. L. *Applied Optics* **1998**, *37*, 5271–5283.

(169) García Rey, N.; Arnolds, H. *The Journal of Chemical Physics* **2011**, *135*, 224708.

(170) Mulugeta, D.; Kim, K. H.; Watanabe, K.; Menzel, D.; Freund, H.-J. *Physical Review Letters* **2008**, *101*, 146103.

(171) Hamann, H. F.; Gallagher, A.; Nesbitt, D. J. *Applied Physics Letters* **1998**, *73*, 1469–1471.

(172) Berweger, S.; Atkin, J. M.; Olmon, R. L.; Raschke, M. B. *The Journal of Physical Chemistry Letters* **2012**, *3*, 945–952.

(173) Sanders, A.; Bowman, R. W.; Zhang, L.; Turek, V.; Sigle, D. O.; Lombardi, A.; Weller, L.; Baumberg, J. J. *Applied Physics Letters* **2016**, *109*, 153110.

(174) Savage, K. J.; Hawkeye, M. M.; Esteban, R.; Borisov, A. G.; Aizpurua, J.; Baumberg, J. J. *Nature* **2012**, *491*, 574–577.

(175) Esteban, R.; Borisov, A. G.; Nordlander, P.; Aizpurua, J. *Nature Communications* **2012**, *3*, 825.

(176) Scholl, J. A.; Garcia-Etxarri, A.; Koh, A. L.; Dionne, J. A. *Nano Letters* **2013**, *13*, 564–569.

(177) Zhu, W.; Crozier, K. B. *Nature Communications* **2014**, *5*, 5228.

(178) Hajisalem, G.; Nezami, M. S.; Gordon, R. *Nano Letters* **2014**, *14*, 6651–6654.

(179) Zhu, W.; Esteban, R.; Borisov, A. G.; Baumberg, J. J.; Nordlander, P.; Lezec, H. J.; Aizpurua, J.; Crozier, K. B. *Nature Communications* **2016**, *7*, 11495.

(180) Kravtsov, V.; Berweger, S.; Atkin, J. M.; Raschke, M. B. *Nano Letters* **2014**, *14*, 5270–5275.

(181) Pohl, D. W.; Denk, W.; Lanz, M. *Applied Physics Letters* **1984**, *44*, 651–653.

(182) Lewis, A.; Isaacson, M.; Harootunian, A.; Muray, A. *Ultramicroscopy* **1984**, *13*, 227–231.

(183) Bao, W. et al. *Science* **2012**, *338*, 1317–1321.

(184) Dürig, U.; Pohl, D. W.; Rohner, F. *Journal of Applied Physics* **1986**, *59*, 3318–3327.

(185) Oshikane, Y.; Kataoka, T.; Okuda, M.; Hara, S.; Inoue, H.; Nakano, M. *Science and Technology of Advanced Materials* **2007**, *8*, 181–185.

(186) Wessel, J. *Journal of the Optical Society of America B: Optical Physics* **1985**, *2*, 1538–1541.

(187) Hayazawa, N.; Inouye, Y.; Sekkat, Z.; Kawata, S. *Optics Communications* **2000**, *183*, 333–336.

(188) Stöckle, R. M.; Suh, Y. D.; Deckert, V.; Zenobi, R. *Chemical Physics Letters* **2000**, *318*, 131–136.

(189) Anderson, M. S. *Applied Physics Letters* **2000**, *76*, 3130–3132.

(190) Steidtner, J.; Pettinger, B. *Physical Review Letters* **2008**, *100*, 236101.

(191) Zhang, R.; Zhang, Y.; Dong, Z. C.; Jiang, S.; Zhang, C.; Chen, L. G.; Zhang, L.; Liao, Y.; Aizpurua, J.; Luo, Y.; Yang, J. L.; Hou, J. G. *Nature* **2013**, *498*, 82–86.

(192) Klingsporn, J. M.; Jiang, N.; Pozzi, E. A.; Sonntag, M. D.; Chulhai, D.; Seideman, T.; Jensen, L.; Hersam, M. C.; Duyne, R. P. V. *Journal of the American Chemical Society* **2014**, *136*, 3881–3887.

(193) Lambe, J.; McCarthy, S. L. *Physical Review Letters* **1976**, *37*, 923–925.

(194) Hansma, P. K.; Broida, H. P. *Applied Physics Letters* **1978**, *32*, 545–547.

(195) Gimzewski, J. K.; Reihl, B.; Coombs, J. H.; Schlittler, R. R. *Zeitschrift für Physik B Condensed Matter* **1988**, *72*, 497–501.

(196) Gimzewski, J. K.; Sass, J. K.; Schlitter, R. R.; Schott, J. *Europhysics Letters* **1989**, *8*, 435.

(197) Johansson, P.; Monreal, R.; Apell, P. *Physical Review B* **1990**, *42*, 9210–9213.

(198) Berndt, R.; Gimzewski, J. K.; Johansson, P. *Physical Review Letters* **1991**, *67*, 3796–3799.

(199) Downes, A.; Welland, M. E. *Applied Physics Letters* **1998**, *72*, 2671–2673.

(200) Ushioda, S. *Solid State Communications* **1992**, *84*, 173–176.

(201) Alvarado, S. F.; Renaud, P.; Abraham, D. L.; Schönenberger, C.; Arent, D. J.; Meier, H. P. *Journal of Vacuum Science & Technology B: Microelectronics and Nanometer Structures Processing, Measurement, and Phenomena* **1991**, *9*, 409–413.

(202) Hakanson, U.; Johansson, M. K.-J.; Persson, J.; Johansson, J.; Pistol, M.-E.; Montelius, L.; Samuelson, L. *Appl. Phys. Lett.* **2002**, *80*, 494–496.

(203) Berndt, R.; Gaisch, R.; Gimzewski, J. K.; Reihl, B.; Schlittler, R. R.; Schneider, W. D.; Tschudy, M. *Science* **1993**, *262*, 1425–1427.

(204) Qiu, X. H.; Nazin, G. V.; Ho, W. *Science* **2003**, *299*, 542–546.

(205) Shigekawa, H.; Takeuchi, O.; Aoyama, M. *Science and Technology of Advanced Materials* **2005**, *6*, 582.

(206) Cocker, T. L.; Jelic, V.; Gupta, M.; Molesky, S. J.; Burgess, J. A. J.; Reyes, G. D. L.; T., L. V.; Tsui, Y. Y.; Freeman, M. R.; Hegmann, F. A. *Nature Photonics* **2013**, *7*, 620–625.

(207) Van Schrojenstein Lantman, E. M.; Deckert-Gaudig, T.; Mank, A. J. G.; Deckert, V.; Weckhuysen, B. M. *Nature Nanotechnology* **2012**, *7*, 583–586.

(208) Sun, M.; Zhang, Z.; Zheng, H.; Xu, H. *Scientific Reports* **2012**, *2*, 647.

(209) Merlen, A.; Chaigneau, M.; Coussan, S. *Physical Chemistry Chemical Physics* **2015**, *17*, 19134–19138.

(210) Debus, C.; Lieb, M. A.; Drechsler, A.; Meixner, A. J. *Journal of Microscopy* **2003**, *210*, 203–208.

(211) Zhang, Z.; Sun, M.; Ruan, P.; Zheng, H.; Xu, H. *Nanoscale* **2013**, *5*, 4151–4155.

(212) Kumar, N.; Stephanidis, B.; Zenobi, R.; Wain, A. J.; Roy, D. *Nanoscale* **2015**, *7*, 7133–7137.

(213) Tallarida, N.; Rios, L.; Apkarian, V. A.; Lee, J. *Nano Letters* **2015**, *15*, 6386–6394.

(214) Kazuma, E.; Jung, J.; Ueba, H.; Trenary, M.; Kim, Y. *Science* **2018**, *360*, 521–526.

(215) Wu, S. W.; Ogawa, N.; Ho, W. *Science* **2006**, *312*, 1362–1365.

(216) Apell, S. P.; Penn, D. R. *Physical Review B* **1992**, *45*, 6757–6768.

(217) Thon, A.; Merschdorf, M.; Pfeiffer, W.; Klamroth, T.; Saalfrank, P.; Diesing, D. *Applied Physics A* **2004**, *78*, 189–199.

(218) Li, S.; Chen, S.; Li, J.; Wu, R.; Ho, W. *Physical Review Letters* **2017**, *119*, 176002.

(219) Chen, C., *Introduction to scanning tunneling microscopy*; Monographs on the physics and chemistry of materials; Oxford University Press: 2008.

(220) Aizpurua, J.; Hoffmann, G.; Apell, S. P.; Berndt, R. *Physical Review Letters* **2002**, *89*, 156803.

(221) Pettinger, B.; Ren, B.; Picardi, G.; Schuster, R.; Ertl, G. *Journal of Raman Spectroscopy* **2005**, *36*, 541–550.

(222) Meng, L.; Yang, Z.; Chen, J.; Sun, M. *Scientific Reports* **2015**, *5*, 9240.

(223) Willets, K. A.; Wilson, A. J.; Sundaresan, V.; Joshi, P. B. *Chemical Reviews* **2017**, *117*, 7538–7582.

(224) Benz, F.; Schmidt, M. K.; Dreismann, A.; Chikkaraddy, R.; Zhang, Y.; Demetriadou, A.; Carnegie, C.; Ohadi, H.; de Nijs, B.; Esteban, R.; Aizpurua, J.; Baumberg, J. J. *Science* **2016**, *354*, 726–729.

(225) Trautmann, S.; Aizpurua, J.; Gotz, I.; Undisz, A.; Dellith, J.; Schneidewind, H.; Rettenmayr, M.; Deckert, V. *Nanoscale* **2017**, *9*, 391–401.

(226) Behr, N.; Raschke, M. B. *Journal of Physical Chemistry C* **2008**, *112*, 3766–3773.

(227) Zhang, C.; Chen, B.-Q.; Li, Z.-Y. *Journal of Physical Chemistry C* **2015**, *119*, 11858–11871.

(228) Neacsu, C. C.; Steudle, G. A.; Raschke, M. B. *Applied Physics B* **2005**, *80*, 295–300.

(229) Dong, Z. C.; Zhang, X. L.; Gao, H. Y.; Luo, Y.; Zhang, C.; Chen, L. G.; Zhang, R.; Tao, X.; Zhang, Y.; Yang, J. L.; Hou, J. G. *Nature Photonics* **2009**, *4*, 50–54.

(230) Zuloaga, J.; Prodan, E.; Nordlander, P. *Nano Letters* **2009**, *9*, 887–891.

(231) Pérez-González, O.; Zabala, N.; Borisov, A. G.; Halas, N. J.; Nordlander, P.; Aizpurua, J. *Nano Letters* **2010**, *10*, 3090–3095.

(232) De Nijs, B.; Benz, F.; Barrow, S. J.; Sigle, D. O.; Chikkaraddy, R.; Palma, A.; Carnegie, C.; Kamp, M.; Sundararaman, R.; Narang, P.; Scherman, O. A.; Baumberg, J. J. *Nature Communications* **2017**, *8*, 994.

(233) Frederiksen, T.; Paulsson, M.; Ueba, H. *Physical Review B* **2014**, *89*, 035427.

(234) Koch, M.; Pagan, M.; Persson, M.; Gawinkowski, S.; Waluk, J.; Kumagai, T. *Journal of the American Chemical Society* **2017**, *139*, 12681–12687.

(235) Kumagai, T.; Kaizu, M.; Okuyama, H.; Hatta, S.; Aruga, T.; Hamada, I.; Morikawa, Y. *Physical Review B* **2009**, *79*, 035423.

(236) Roth, R. M.; Panoiu, N. C.; Adams, M. M.; Osgood, R. M.; Neacsu, C. C.; Raschke, M. B. *Optics Express* **2006**, *14*, 2921–2931.

(237) Demming, A. L.; Festy, F.; Richards, D. *The Journal of Chemical Physics* **2005**, *122*, 184716.

(238) Van Hulst, N. F.; Segerink, F. B.; Achten, F.; Bölger, B. *Ultramicroscopy* **1992**, *42-44*, 416–421.

(239) Ferrell, T. L.; Sharp, S. L.; Warmack, R. J. *Ultramicroscopy* **1992**, *42-44*, 408–415.

(240) Zhang, P.; Haslett, T. L.; Douketis, C.; Moskovits, M. *Physical Review B* **1998**, *57*, 15513–15518.

(241) Seal, K.; Sarychev, A. K.; Noh, H.; Genov, D. A.; Yamilov, A.; Shalaev, V. M.; Ying, Z. C.; Cao, H. *Physical Review Letters* **2005**, *94*, 226101.

(242) Bozhevolnyi, S. I.; Vohnsen, B.; Smolyaninov, I. I.; Zayats, A. V. *Optics Communications* **1995**, *117*, 417–423.

(243) Mihaljevic, J.; Hafner, C.; Meixner, A. J. *Opt. Express* **2015**, *23*, 18401–18414.

(244) Ropers, C.; Neacsu, C. C.; Elsässer, T.; Albrecht, M.; Raschke, M. B.; Lienau, C. *Nano Letters* **2007**, *7*, 2784–2788.

(245) Bartels, L.; Wang, F.; Moeller, D.; Knoesel, E.; Heinz, T. F. *Science* **2004**, *305*, 648–651.

(246) Mehlhorn, M.; Gawronski, H.; Nedelmann, L.; Grujic, A.; Morgenstern, K. *Review of Scientific Instruments* **2007**, *78*, 033905.

(247) Mehlhorn, M.; Carrasco, J.; Michaelides, A.; Morgenstern, K. *Physical Review Letters* **2009**, *103*, 026101–.

(248) Mehlhorn, M.; Gawronski, H.; Morgenstern, K. *Physical Review Letters* **2010**, *104*, 076101.

(249) Zaum, C.; Meyer-auf-der Heide, K. M.; Mehlhorn, M.; McDonough, S.; Schneider, W. F.; Morgenstern, K. *Physical Review Letters* **2015**, *114*, 146104.

(250) Kazuma, E.; Jung, J.; Ueba, H.; Trenary, M.; Kim, Y. *Journal of the American Chemical Society* **2017**, *139*, 3115–3121.

(251) Tan, S.; Feng, H.; Ji, Y.; Wang, Y.; Zhao, J.; Zhao, A.; Wang, B.; Luo, Y.; Yang, J.; Hou, J. G. *Journal of the American Chemical Society* **2012**, *134*, 9978–9985.

(252) Zhou, C. et al. *Chemical Science* **2010**, *1*, 575–580.

(253) Sakong, S.; Gross, A. *Journal of Catalysis* **2005**, *231*, 420–429.

(254) Wachs, I. E.; Madix, R. J. *Journal of Catalysis* **1978**, *53*, 208–227.

(255) Bowker, M.; Madix, R. *Surface Science* **1980**, *95*, 190–206.

(256) Sexton, B.; Hughes, A.; Avery, N. *Surface Science* **1985**, *155*, 366–386.

(257) Bader, M.; Puschmann, A.; Haase, J. *Physical Review B* **1986**, *33*, 7336–7338.

(258) Holub-Krappe, E.; Prince, K.; Horn, K.; Woodruff, D. *Surface Science* **1986**, *173*, 176–193.

(259) Hofmann, P.; Menzel, D. *Surface Science* **1987**, *191*, 353–366.

(260) Peremans, A.; Maseri, F.; Darville, J.; Gilles, J.-M. *Journal of Vacuum Science & Technology A: Vacuum, Surfaces, and Films* **1990**, *8*, 3224–3228.

(261) Ammon, C.; Bayer, A.; Held, G.; Richter, B.; Schmidt, T.; Steinrück, H.-P. *Surface Science* **2002**, *507-510*, 845–850.

(262) Karolewski, M.; Cavell, R. *Applied Surface Science* **2001**, *173*, 151–163.

(263) Carley, A.; Davies, P.; Mariotti, G.; Read, S. *Surface Science* **1996**, *364*, 525–529.

(264) Davies, P. R.; Mariotti, G. G. *Catalysis Letters* **1997**, *43*, 261–266.

(265) Wachs, I. E.; Madix, R. J. *Surface Science* **1979**, *84*, 375–386.

(266) Kitaguchi, Y.; Shiotari, A.; Okuyama, H.; Hatta, S.; Aruga, T. *The Journal of Chemical Physics* **2011**, *134*, 174703.

(267) Sakong, Sendner, C.; Gross, A. *Journal of Molecular Structure: THEOCHEM* **2006**, *771*, 117–122.

(268) Singnurkar, P.; Bako, I.; Koch, H. P.; Demirci, E.; Winkler, A.; Schennach, R. *Journal of Physical Chemistry C* **2008**, *112*, 14034–14040.

(269) Jackels, C. F. *The Journal of Chemical Physics* **1985**, *82*, 311–322.

(270) Sakong, S.; Gross, A. *Journal of Physical Chemistry A* **2007**, *111*, 8814–8822.

(271) Mei, D.; Xu, L.; Henkelman, G. *Journal of Physical Chemistry C* **2009**, *113*, 4522–4537.

(272) Stipe, B. C.; Rezaei, M. A.; Ho, W. *Physical Review Letters* **1998**, *81*, 1263–1266.

(273) Ho, W. *The Journal of Chemical Physics* **2002**, *117*, 11033–11061.

(274) Bowker, M.; Madix, R. *Surface Science* **1981**, *102*, 542 –565.

List of Publications

Publications within this Thesis

H. Böckmann, C. Lin, J. Waluk, M. Wolf and T. Kumagai.
Single-Molecule Photochemistry by Resonant Hole Attachment from Plasmonic Decay.
In Preparation

H. Böckmann, M. Müller, A. Hammud, M.-G. Willinger, M. Pszona, J. Waluk, M. Wolf and T. Kumagai.
Near-Field Spectral Response of Optically Excited Scanning Tunneling Microscope Junctions Probed by Single-Molecule Action Spectroscopy.
Journal of Physical Chemistry Letters, **10**(9): 2068-2074 (2019)

H. Böckmann, S. Liu, M. Müller, A. Hammud, M. Wolf and T. Kumagai.
Near-Field Manipulation in a Scanning Tunneling Microscope Junction with Plasmonic Fabry-Pérot Tips.
Nano Letters, **19**(6): 3597-3602 (2019)

H. Böckmann, S. Gawinkowski, J. Waluk, M. B. Raschke, M. Wolf and T. Kumagai.
Near-Field Enhanced Photochemistry of Single Molecules in a Scanning Tunneling Microscope Junction.
Nano Letters, **18**(1): 152-157 (2018)

H. Böckmann, S. Liu, J. Mielke, S. Gawinkowski, J. Waluk, L. Grill, M. Wolf and T. Kumagai.
Direct observation of photoinduced tautomerization in single molecules at a metal surface.
Nano Letters, **16**(2): 1034-1041 (2016)

Publications concering other Topics

P. Li, T. Wang, H. Boöckmann and T. Taubner.
Graphene-enhanced infrared near-field microscopy.
Nano Letters, **14**(8): 4400–4405 (2014)

Selbstständigkeitserklärung

Ich erkläre, dass ich die vorliegende Arbeit selbstständig und nur unter Verwendung der angegebenen Literatur und Hilfsmittel angefertigt habe.

Berlin, den 07.08.2018 Hannes Böckmann